Second Harmonic Generation: Probing Photochromic Interfaces and Ultrafast Charge Transfer Processes

Im Fachbereich Physik
der Freien Universität Berlin
eingereichte Dissertation

Michael Schulze

Oktober 2014

Die vorliegende Arbeit wurde zwischen April 2011 und Mai 2013 am Fachbereich Physik der Freien Universität Berlin und von Juni 2013 bis Oktober 2014 am Physikalisch-Chemischen Institut der Ruprecht-Karls-Universität Heidelberg angefertigt.

Erstgutachterin:	Prof. Dr. Petra Tegeder
Zweitgutachter:	Prof. Dr. Martin Weinelt
Datum der Disputation:	19.02.2015

Abstract

The inherent interface sensitivity of the second harmonic generation (SHG) setup developed and realized in the framework of this thesis is successfully utilized to investigate functionalized surfaces and functional thin layers, *viz.* photochromic azobenzene and fulgimide self-assembled monolayers (SAMs) and the electron donor/acceptor (D/A) heterojunction C_{60}/P3HT. Applying light as an external stimulus and observing the induced changes in the interfacial non-linear optical (NLO) response, the switching state of the photochromic interfaces is read out *via* the isomerization-correlated static charge reallocation. Moreover, the ultrafast charge transfer (CT) across the D/A interface is monitored with time-resolved SHG on a femtosecond timescale.

En route towards innovative photonic and optoelectronic data processing and transmitting microelectronic components and data storage devices, photochromic interfaces exhibiting reversibly controllable NLO properties inhere intriguing potential. The strategy of anchoring fulgimide and azobenzene chromophores *via* SAMs to metallic and semiconducting substrates, respectively, results in substantial NLO contrasts. Polarization-resolved SHG measurements enable to identify a correlation of these NLO responses to conjugation and orientation of the π-electron system and hence reveal information on the chromophore alignment. In case of the fulgimide system, density functional theory as well as correlated wavefunction method calculations confirm these results. In addition, the NLO contrast depends on a precise balance of chromophore-functionalized and unmodified spacer chains. A progressing inability to photoisomerize sets in at intermediate azobenzene packing densities. The successful chromophore–substrate decoupling is furthermore reflected in large isomerization cross-sections and results in thermal stability at ambient conditions.

The C_{60}/P3HT heterojunction is investigated regarding the dynamics and energetics of the ultrafast charge transfer across the D/A interface. Reducing the complexity of this prototypal system to a single, well-defined D/A interface enables a maximized exploitation of the interface sensitivity of the SHG probe and hence an unambiguous understanding of the fundamental CT mechanisms. The formation and subsequent thermalization of 'hot excitons' in the donor occurs on an ultrafast timescale. However, in the presence of the acceptor the charge transfer is identified as the dominating relaxation mechanism. Most remarkably, the yield of the CT process is revealed to correlate with the excitation wavelength. It increases with the amount of excess energy.

Zusammenfassung

Im Rahmen dieser Arbeit wurde ein experimenteller Aufbau entwickelt und realisiert, welcher die intrinsische Grenzflächensensitivität des nichtlinear optischen (NLO) Effekts der Frequenzverdopplung (engl. second harmonic generation, SHG) ausnutzt, um funktionalisierte Oberflächen und funktionale Dünnschichten zu untersuchen. Im Speziellen wurde der Schaltzustand selbstorganisierter Monolagen (engl. self-assembled monolayers, SAMs) photochromer Azobenzole und Fulgimide erfolgreich ausgelesen und der Ladungstransfer (engl. charge transfer, CT) in der Elektronen-Donor/Akzeptor Heterostruktur (D/A) C_{60}/P3HT konnte auf der Femtosekundenzeitskala beobachtet werden.

Hinsichtlich innovativer photonischer und optoelektronischer datenverarbeitender und -übermittelnder Mikroelektronik und Datenspeichermodule, bieten photochrome Oberflächen mit reversibel einstellbaren NLO Eigenschaften großes Potential. Die Anbindung photochromer Fulgimide und Azobenzole über SAMs an metallische beziehungsweise halbleitende Substrate, führt zu einer effizienten, lichtinduzierten Schaltbarkeit zwischen Zuständen mit substanziellen NLO Kontrasten. Polarisationtsaufgelöste SHG-Messungen ermöglichen die Identifikation eines Zusammenhangs zwischen den NLO Eigenschaften und dem Grad der Konjugation und der Orientierung des π-Elektronensystems und liefern damit Informationen über die Ausrichtung der Chromophore. Für die Fulgimide werden diese Ergebnisse von Dichtefunktional- und Strörungstheorie bestätigt. Des Weiteren hängt der NLO Kontrast von einem präzisen Verhältnis zwischen Chromophorfunktionalisierten und als Abstandhalter fungierenden Molekülen ab. Beginnend bei mittleren Packungsdichten wird eine zunehmende Unfähigkeit der Azobenzole zu isomerisieren beobachtet.

Die C_{60}/P3HT-Heterostruktur wird hinsichtlich Dynamik und Energetik des ultraschnellen Ladungstransfers an der D/A-Grenzfläche untersucht. Die Reduzierung der Komplexität dieses prototypischen Systems zu einer einzelnen, wohldefinierten D/A-Grenzfläche maximiert zum Einen den Nutzen der intrinsischen SHG-Grenzflächensensitivität. Zum Anderen wird ein eindeutiges Verständnis der zugrundeliegenden CT-Mechanismen ermöglicht. Im Donor wird die ultraschnelle Entstehung und anschließende Thermalisierung 'heißer Exzitonen' beobachtet. In Gegenwart des Akzeptors wird zusätzlich ein CT-Zustand identifiziert, welcher für das D/A-System den dominierenden Relaxationsmechanismus darstellt. Bemerkenswert ist dabei die Korrelation zwischen steigender CT-Ausbeute und der überschüssigen Anregungsenergie.

Contents

List of Figures

List of Tables

Chapter 1

Introduction

Second Harmonic Generation

The first reported observation of second harmonic generation (SHG) effect in non-linear optical materials was in 1961 [1]. It was enabled by the realization of pulsed ruby lasers [2] which provided the necessary monochromaticity and electric field strengths. Actual implementations as an experimental technique capable of detecting less than a monolayer of surface adsorbed molecules [3] date back to the mid-eighties of the last century [4]. Since then, the method has proven to be a versatile probe for surface and interface studies [5]. SHG probes the non-linear optical properties of a medium described by the susceptibility tensor of second order $\chi^{(2)}$ [6]. The intrinsic interface sensitivity of this experimental method derives from the quadratic dependency of the SHG signal on the strong electric field of the probing (femtosecond) laser pulse: for homogeneous samples only the symmetry breaking interfaces contribute to the SHG signal [7]. This circumstance can be exploited experimentally for the investigation of functionalized surfaces and functional thin films by triggering the respective functionality *via* applying an external stimulus and monitoring the induced changes. As the $\chi^{(2)}$ tensor correlates to the electronic structure of the system, these 'induced changes' in principle span any alteration of the interfacial electron density, both static [8–11] and dynamic [12–15] as for the photochromic interfaces and charge transfer processes investigated in the framework of this thesis, respectively.

Other established spectroscopic surface sensitive probes as two-photon photoelectron spectroscopy (2PPE) [16], Auger electron spectroscopy (AES) [17], high-resolution electron energy loss spectroscopy (HREELS) [18], normal incidence x-ray standing wave (NIXSW) [19], scanning tunneling microscopy and spectroscopy (STM/STS) [20, 21], only to name a few, offer different advantages for the investigation of surfaces. However, the common disadvantage in comparison to SHG relates to the detection of electrons which (a) demands for conducting substrates to avoid charging the sample (b) generally renders buried interfaces like donor/acceptor heterojunctions inaccessible if the top layer thickness exceeds a few monolayers due to the limited electron

escape depth and (c) requires to work under (ultra high) vacuum conditions, although the latter is in the case STM/STS only true if substantial cooling is desired. Light-detecting experimental probes like attenuated total reflection (ATR) [22], photoluminescence and transient absorption spectroscopy (PL, TA) [23], *etc.* are usually either not time-resolved or not explicitly interface sensitive, respectively. Spectroscopic probes using non-linear optical effects of second order, *viz.* SHG and sum-frequency generation (SFG), can be utilized for the time-resolved investigation of samples under standard pressure conditions and excluding interfering bulk contributions to the signal on the one hand but with access to buried interfaces [24] on the other hand.

The versatility of the SHG probe reflects in the diversity of conducted investigations and examined systems. The surface sensitivity in general and the sub-monolayer resolution in particular have for instance been demonstrated in experiments as different as the thermally induced surface reconstructions of silicon [25], the determination of the orientation of organic molecules at the air/water interface [26] or the oxidation and reduction of a silver surface [27]. The applicability to buried interfaces has also been exploited to gain structural information on metal–semiconductor [28, 29] and magnetic multilayer interfaces [30–32]. The structural sensitivity of polarization- [33, 34] or rarely angle-resolved [35] SHG experiments has been demonstrated to even extend to the determination of the smoothness of surfaces and interfaces. The derivation of structural information is often facilitated in conjunction with spectroscopic SHG by tuning into resonances of either the fundamental or the second harmonic wavelength as for instance demonstrated for organic dye adlayers [36] as well as differently modified silicon substrates [37, 38]. Spectroscopic SHG has also been applied to probe excitonic transitions in molecules relevant to organic photovoltaics as C_{60} [39, 40]. Moreover, the conjunction with time-resolved SHG (TR-SHG) allows to monitor the dynamics of explicitly addressed excited states [12, 41]. TR-SHG proves particularly useful also for the investigation of organic [14, 15] and inorganic [13] charge transfer heterojunctions. The reason is the significant electric field enhancement of the TR-SHG signal amplitude arising from the charge transfer across a well defined donor/acceptor interface known as electric field enhanced second harmonic generation (EFISH) [42, 43]. This effect of field amplification has also been reported to occur when probing the junction between sample and a biased gold tip [44] which might lead to the intriguing concept of an SHG setup with nanometer spatial resolution. Finally, several groups report on large SHG amplitude contrasts between the different photostationary states of interfaces functionalized with photochromic molecules as azobenzenes immobilized in polymers and Langmuir films [9–11].

In the framework of this thesis an experimental SHG setup based on near-infrared and wavelength-tunable visible lasers has been developed and realized. The inherent interface sensitivity as well as the temporal, spatial and energetic

resolution of time- and polarization-resolved and spectroscopic SHG, respectively, enabled the successful investigation of functionalized surfaces and functional thin layers, *viz.* photochromic fulgimide and azobenzene self-assembled monolayers (SAMs) and the electron donor/acceptor (D/A) heterojunction C_{60}/P3HT.

Photochromic Interfaces

The importance of the interface sensitivity of the experimental probe becomes obvious when considering emerging innovative approaches in ubiquitous high-tech research fields, in which the underlying device functionality no longer derives from bulk material properties but from functionalized interfaces. The motivation for exploring novel design principles for data processing and transmitting microelectronic components and data storage devices, for instance, is the limitation of the device performance optimization *via* top-down miniaturization of smallest functional units. These arise from quantum mechanical phenomena governing the already approached nanoscale [45]. For example a further development of usually silicon-processed, transistor-based electronic components is practically limited by the feasibility of progressing the miniaturization of the transistor itself. This is due to the leakage currents at small gate lengths which leads to considerable excess heat development and power consumption already for the present transistor architecture [46]. While basically the same argument holds for the increase of the storage density of semiconductor-based data storage devices, the size reduction of single memory blocks in current magnetic and optical devices is limited by their thermal stability [47] and readout ability [48], respectively.

Among the most intriguing alternatives to the top-down approach is the targeted exploitation of quantum mechanical phenomena for which the consideration of topological insulators for spintronic devices [49–51] is an example. Likewise, the bottom-up device fabrication out of surfaces-immobilized single functional molecules is a promising concept. For instance the combination of molecular switches providing (light-induced) reversibly controllable electrical conductance over several orders of magnitude [52] with (semi-) conducting, surface-synthesized nanostructures [53–56] and molecular 'wires' [57] might lead to electronics based on molecular transistors. Furthermore, various molecular switches have been used for the construction of three-dimensional optical data storage devices, written and read out by means of (non-linear) optical methods [48, 58, 59] or as all-optical logic signal processing units [60, 61]. Equally intriguing are molecular switches with reversibly controllable non-linear optical (NLO) properties [62–67]. These might lead to the development of novel photonic and optoelectronic devices [68–70] for which the applicability of NLO switches as cation sensors is one example [71, 72].

However, exploiting the photochromic properties of molecular switches requires a successful immobilization strategy first of all regarding the preservation of the switching ability and second concerning a fine-tuning of the characteristics of the photochromic interface. Various general approaches exist. These range from physisorption [73, 74] to the incorporation of the chromophores into polymers [75, 76], Langmuir monolayers [10, 11] or Langmuir-Blodgett-films [77, 78] as well as to the chemical attachment to self-assembled monolayers [79, 80], all of which offer different advantages and disadvantages.

Polymers containing stereoisomeric chromophores like azobenzene undergo mechanic deformations upon isomerization and exhibit relatively low isomerization speed [81] which renders these materials inappropriate for applications in for instance optical data storage devices. However, the inducible macroscopic changes enable surface pattern writing which is for example utilized to photofabricate surface relief gratings [82]. Also, a photoswitching of the wettability [83] or of the magnetization [84] of azobenzene-functionalized Langmuir-Blodgett-films was demonstrated, albeit in both cases accompanied by a certain fatigue in the reversibility.

A lesson learned in following the physisorption strategy is that the photoisomerization ability of an immobilized molecular switch cannot only be preserved but also get 'restored'. The preservation in this context relates to an isomerization driven by an intramolecular transition following a direct photon-excitation which has only rarely been reported to be operational [85,86], albeit never bi-directional and wavelength-selective. Besides a possible steric hindrance of the isomerization-correlated nuclei motion due to the presence of the surface, the main reason for a quenched photoisomerization ability is a strong electronic adsorbate–substrate interaction and the according de-excitation of the photochromic unit prior to completion of the isomerization [87]. Nevertheless, this interaction is also exploitable as the example of the prototypal molecular switch azobenzene adsorbed on Au(111) illustrates. For the unsubstituted molecule, the photoswitching is inactive but it gets restored by adding bulky spacer groups. Interestingly, not *via* the expected geometric decoupling, as the molecule bends [88] and the photochromically active backbone [89, 90] is not lifted in comparison to azobenzene [91]. Rather the alteration of the energetic alignment of substrate- and adsorbate-derived electronic states [92] restores the photoisomerization ability. The switching of the corresponding derivative TBA (3,3',5,5'-tetra-*tert*-butyl-azobenzene) is driven by a positive ion resonance, i.e., a substrate-mediated excitation mechanism [93,94]. This example, like the correlated negative ion resonance observed for another azobenzene on bismuth [56], emphasizes the importance of precisely fine-tuning the adsorbate–substrate interaction [87].

The molecular switches investigated within the framework of this thesis, namely a fulgimide and azobenzene, were immobilized *via* attachment to self-

assembled monolayers on the technologically relevant metallic and semiconducting surfaces gold and silicon, respectively. Following this strategy, well-defined and well-ordered interfaces are obtained which are accordingly ideally suited to be investigated in an SHG experiment. In both cases, the decoupling between substrate and adsorbate is successful and the reversible control over the respective switching states is demonstrated. The large observed NLO contrast between the respective photostationary states (PSSs) is a result of the difference in the degrees in conjugation and orientation of the π-electron system read out *via* the second order susceptibility reflecting the interfacial electron density in both cases. For the fulgimide SAM the degree in electronic conjugation of the π-system is significantly reduced in the ring-opening reaction and *vice versa*, while for the azobenzene SAM the π-system is geometrically rearranged in the *trans* $\leftrightarrow$ *cis* isomerization. These characteristics render the here investigated photochromic interfaces relevant for possible future applications especially in novel photonic and optoelectronic devices [58–63, 68–72]. The combination of the reversibly controllable interfacial non-linear optical response and the photochromic functionalization of a gold and a silicon substrate, both being of major relevance for today's microelectronics, might constitute a link from present to future photonic and optoelectronic devices.

The fulgimide-functionalized SAM on the silicon surface is switched between two PSSs which differ by the respective isomer composition. While illumination with UV light establishes a 'closed-PSS' enriched with closed fulgimides (C), visible light triggers the ring-opening reaction and the corresponding 'open-PSS' solely consists of a mixture of the open *trans*- (E) and *cis*-forms (Z) [80]. As the degree in electronic conjugation is significantly higher for the extended four-ring π-system of the closed fulgimide, a substantial NLO contrast is expected. A fully reversible SHG signal amplitude change of 17 ± 6 % is indeed observed, when alternately illuminating the fulgimide-functionalized surface with visible and UV light, and attributed to switching between the two at room temperature thermally stable PSSs. Cross-sections on the order of 10^{-18} cm^{-2} are determined for both reaction paths. These are four orders of magnitude larger in comparison to the surface-mediated isomerization of TBA/Au(111) on the one hand [94] and of comparable magnitude as found for other azobenzene SAMs with larger linker systems on the other hand [95, 96] which indicates a successful decoupling strategy and hence an intramolecular photoexcitation mechanism. Finally, the components of the interfacial second order susceptibility tensor $\chi^{(2)}$ are accessed in polarization-resolved SHG measurements and compared to the molecular first order hyperpolarizabilities (i.e., the molecular equivalent of the second order non-linear susceptibility [26, 97]) of the fulgimide isomers. These were obtained with density functional theory as well as correlated wavefunction method calculations. The expected orientation of the closed fulgimide almost perpendicular to the surface [80] is in

agreement with both, an observed dominating NLO response and a large calculated hyperpolarizability in that direction. Furthermore, the calculated overall hyperpolarizabilities of both open forms are significantly smaller in comparison to the closed fulgimide due to the lower degree in electronic conjugation. This fits well to the observed pronounced SHG signal amplitude decrease in the ring-opening reaction and *vice versa*.

For the azobenzene containing SAMs on gold, a large interfacial second order non-linear susceptibility is expected if the thermally stable [98] *trans*-azobenzenes are well-aligned with their two phenyl-rings forming a π-electron system perpendicular to the surface. A significant NLO contrast is accordingly expected if a PSS predominantly containing bent *cis*-isomers can be established which appears to be a matter of the spacing between the chromophores [99–104]. A pronounced change in the SHG signal amplitude of 19 ± 3 % is indeed observed, when the azobenzene SAM constituting a mixture of 75 % chromophore-functionalized alkyl chains and 25 % unmodified linkers is alternately illuminated with visible and UV light. The reversibly addressable NLO response levels are assigned to the *trans*- and *cis*-PSSs. Interestingly, a thermal stability of the *cis*-PSS is solely observed if certain requirements are fulfilled and appears to depend on the environmental conditions, *viz.* the presence of ambient water. Switching cross-sections on the order of 10^{-18} cm^{-2} for both isomerization paths indicate a successful decoupling strategy and hence an intramolecular photoexcitation mechanism as concluded for the fulgimide SAM. The expected chromophore alignment parallel to the surface normal is confirmed in polarization-resolved SHG measurements. The SHG signal amplitude sensitive to the non-linear susceptibility perpendicular to the surface is three order of magnitude larger than the ones measured for other polarization settings. Accordingly, the *trans* $\rightarrow$ *cis* isomerization reduces the NLO response perpendicular to the interface while the parallel non-linear susceptibility for the bent *cis*-isomer increases. By varying the ratio of chromophore-modified alkyl chains to empty linkers between 10 ± 5 and 95 ± 5, the influence of the packing density on the photoisomerization ability is investigated. The NLO contrast at low chromophore concentration is reduced due to the lower number of contributing chromophores possibly assisted by a disordering effect. The difference in the SHG responses at highest packing density is significantly lowered due to steric hindrance [104] or excitonic coupling [102, 103, 105]. However, a broad high-contrast plateau at 30-75 % chromophore density is observed.

Ultrafast Charge Transfer Processes

The above mentioned importance of the interface sensitivity of an experimental probe does not only relate to functionalized surfaces, but also to the interfaces of adjacent functional thin layers for instance in organic photovoltaic devices

(OPVs). Their basic functionality is provided by interfacing thin layers of (electron) donor and acceptor materials to form the heterojunction across which charge transfer and eventually charge separation occur [106–108]. The desired advantages from the usually solution processed or evaporation deposited functional thin layers in comparison to bulk-derived construction principles are low-cost production, mechanical flexibility and weight-reduction [109, 110].

For the investigation of these systems, also the temporal resolution of the SHG setup on the order of 50 fs is essential. For instance singlet fission (SF), a process in which the Shockley-Queisser-limit [111] is exceeded by splitting a single above-bandgap excitation into two or more electron–hole pairs prior to thermalization [112–116] constitutes an illustrative example for ultrafast dynamics in organic molecules. In pentacene, a multiple exciton state originating from SF has been found not only to get populated on a sup-picosecond timescale, but also to get depopulated into a spin-triplet state already within this short timeframe [14]. Another example is the currently controversially discussed topic of the involvement of so-called 'hot excitons', i.e., the necessity of excess energy from above-bandgap excitation for an efficient charge transfer (CT) and charge separation (CS) process at D/A interfaces. Some groups report on a crucial role of hot excitons: (1) for the population of charge transfer states [117], (2) to overcome the poorly screened Coulomb barrier in organic semiconductors and to avoid trapping in relaxed CT ground states localized at the interface [15] and (3) to enhance the probability of charge dissociation out of delocalized CT states [118]. It has also been demonstrated *via* wavefunction-based *ab initio* calculations that the delocalization accompanying the high energetic excitation [117] is accountable for the stabilization of the CT state at the D/A interface [119]. Contrary, no excess energy was found to be needed for the ultrafast charge separation into band-like acceptor states beyond the necessary energy to avoid trapping in the Coulomb potential in blends of fullerenes with small molecules and polymers, respectively [120]. Furthermore, no correlation between the excitation energy and the external quantum efficiency (EQE) of a variety of OPV model systems has been found in recent extensive studies [121, 122]. These contradicting results emphasize the necessity for a better understanding of the light-to-current conversion processes in organic photovoltaics.

By investigating prototypal materials for organic solar cells, namely the organic semiconductor poly(3-hexylthiophene-2,5-diyl) (P3HT) and the electron acceptor C_{60}, this work aims to contribute to the fundamental understanding of the ultrafast charge transfer across the donor/acceptor interface. SHG is especially well suited for this purpose since it combines the necessary temporal resolution with the intrinsic sensitivity to the interface across which the charge transfer occurs. The choice for the P3HT/C_{60} layered D/A structure instead of the commonly used P3HT:PCBM bulk-heterojunction, i.e., a

blend of P3HT and phenyl-C_{61}-butyric acid methyl ester [107, 110, 123–125], reduces the complexity of the system to a single, well-defined interface. The expected absence of diffusion of the not-soluble C_{60} into the donor layer is verified *via* polarization-resolved SHG measurements sensitive to the structure of the interface. The photoinduced dynamics at the D/A interface of this model system can be expected to be very similar to those in P3HT:PCBM blends in which phase-separation results in the formation of donor and acceptor domains [126, 127]. Regarding the charge transfer dynamics, the interface of the model heterojunction investigated in the framework of this thesis thus corresponds to the domain boundaries in the blended materials.

The first step in developing an understanding of the dynamics at the investigated D/A interface is to study the pristine P3HT and C_{60} samples. For the donor, a pronounced pump-induced change in the TR-SHG signal amplitude is observed which returns to the initial level within a few picoseconds. Concerning the initial excitation in P3HT, apparently a consensus exists, that it can be attributed to singlet excitons [128–133]. Regarding the subsequent dynamics, time-constants as short as these are rarely associated with (geminate) exciton recombination [128, 133] or the formation of interchain polarons [132], whereas the excitation and subsequent thermalization of hot excitons is the more reasonable explanation for the observed NLO response. This assignment is in agreement with the theoretically expected and experimentally observed significant delocalization of not-thermalized excitons [117, 119, 130, 134, 135] and the assumed influence on the non-linear susceptibility of the surrounding system [136, 137]. Interestingly, the de-excitation exhibits a bi-exponential behavior. By varying the pump beam wavelength, the involvement of two polymer-derived bands S_1 and the energetically higher S_2 is deduced. In contrast, the pump-induced TR-SHG signal amplitude change observed for pristine C_{60} remains constant within the 20 ps time window of the measurement. As triplet excitons are energetically inaccessible at the applied wavelength and singlet excitations are optically dipole-forbidden in C_{60} [39], the assignment to the excitation of charged polarons [138–140] is most reasonable for the acceptor layer dynamics.

The TR-SHG data of the D/A sample resembles the dynamics observed for pristine P3HT for short delays up to 350 fs which indicates the initial population and the beginning localization of hot excitons in the donor layer. Thereafter, the signal amplitude decreases again instead of proceeding to return to the initial level. These dynamics indicate the delayed population of an interface derived state out of the initial hot exciton population. In accordance, the pronounced TR-SHG contrast at large delays is attributed to a field enhancement induced by charge transfer. Interestingly, solely the thermalization channel associated with the S_1 band is still observed for the D/A sample, while the ultrafast forming CT state appears to be directly populated out of the energet-

ically higher S_2 band prior to de-excitation. Additional spectroscopic TR-SHG measurements conducted by varying the excitation wavelength reveal that a charge transfer out of the S_1 band is also operative. However, the process gets significantly enhanced if sufficient excess excitation energy is available, to additionally involve the S_2 band. Most remarkably, the CT yield correlates with the excitation wavelength and increases with the amount of excess energy. It has to be kept in mind, however, that an increased charge transfer yield does not necessarily result in an increased charge generation yield, as recent studies revealed no correlation between the excitation energy and the quantum yield for charge separation in a variety of OPV model systems [121, 122]. However, this central result suggests that an increased performance of OPVs might be achievable by realizing both, a high CT yield out of a hot exciton population as demonstrated here and an efficient charge separation.

Structure of this Thesis

This thesis is structured as follows. In chapter two the SHG experiment is introduced. The chosen level of detail is provided to impart the knowledge necessary to operate the SHG setup developed and realized within the framework of this thesis. The chapter starts with a theoretical overview on non-linear optics in section 2.1. The experimental setup is described in section 2.2, regarding (a) the laser setup, i.e., in- and out-coupling and modification of the laser pulses, (b) the home-built experimental chamber, (c) light detection and signal processing and (d) data processing routines. The experimental procedures are described in section 2.3.

The topic of chapter three is the NLO response of photochromic interfaces. It starts with an overview on the isomerization and ring-opening/ring-closure reactions of photochromic azobenzenes and fulgimides, respectively, and on surface immobilization strategies as well as the sample preparation of the SAMs investigated in the framework of this thesis in section 3.1. The reversible photoswitching of a fulgimide-functionalized SAM is the topic of section 3.2, with focus on (a) the NLO contrast and the interfacial molecular alignment as well as reversibility, thermal stability and efficiency of the ring-opening/ring-closure processes and (b) the additional theoretical modeling of the NLO contrast by means of density functional theory and correlated wavefunction method calculations. The results regarding the reversible photoisomerization of azobenzene-functionalized SAMs are outlined in section 3.3, regarding (a) the NLO contrast, (b) reversibility, thermal stability and efficiency of the isomerization processes, (c) the interfacial molecular alignment and (d) a correlation of the chromophore packing density and the isomerization ability.

The topic of chapter four is the ultrafast charge transfer across the C_{60}/ P3HT interface. This part of the thesis starts with an introduction on charge

carrier dynamics in organic photovoltaics and an overview on sample preparation in section 4.1 and 4.2, respectively. The TR-SHG results obtained for the pristine P3HT and C_{60} samples are illustrated in section 4.3. The CT dynamics at the C_{60}/P3HT D/A interface are the subject of section 4.4. Finally, the results concerning the CT yield investigated by means of excitation energy resolved SHG measurements are presented in section 4.5.

Chapter 2

The SHG Experiment

SHG probes the second order non-linear optical properties of a medium described by the susceptibility tensor $\chi^{(2)}$. The quadratic dependency of the SHG signal on the strong electric field of a probing femtosecond laser pulse results in an intrinsic interface and surface sensitivity of this experimental method: for homogeneous samples only the symmetry breaking interfaces contribute to the SHG signal [3, 5, 6]. The theoretical background of non-linear optics is outlined in section 2.1.

The inherent interface sensitivity can be exploited experimentally for the investigation of functional surfaces by triggering the respective functionality *via* applying an external stimulus and monitoring the induced changes. As the $\chi^{(2)}$ tensor reflects the electronic structure of the system, these 'induced changes' in principle span any alteration of the interfacial electron density, ranging from the static charge rearrangement in the fulgimide ring-opening/ring-closure isomerization and the differences in the π-system orientation between the *trans*- and *cis*-photostationary states of an azobenzene-functionalized self-assembled monolayer to the dynamic charge redistribution in donor and acceptor materials for organic photovoltaics due to the pump-induced excitation of electron–hole pairs (excitons) and the subsequent charge transfer across the D/A interface, respectively. Two different SHG experiments are conducted in the framework of this thesis as outlined in section 2.3. First, time-resolved second harmonic generation (section 2.3.1) in which a pump pulse excites electron–hole pairs and the temporal evolution of an exciton population is subsequently investigated by varying the femtosecond time delay between pump and probe pulse which results in a temporal resolution on the order of 50 fs, i.e., close to the Fourier-transform-limit. Second, illumination experiments (section 2.3.2) in which the switching state of a surface is read out by alternately illuminating the sample using of cw-diodes and probing the respective interfacial non-linear optical response. Monitoring the overall switching state reveals system parameters as reversibility and thermal stability, while the isomerization kinetics allow to deduce the respective switching cross-sections. In both cases additional geometric information are obtainable by applying polarization-resolved SHG (section 2.3.3), i.e., by varying the polarization of the detected, the probe

and if appropriate the pump beam, respectively, to selectively probe $\chi^{(2)}$ tensor elements. Finally, by tuning the wavelength of the pump beam, spectroscopic SHG (section 2.3.4) measurements are feasible which for example allows for the determination of the energetic position of electronic states.

The accordingly arising technical requirements to conduct these experiments are the topic of section 2.2. This part on the experimental setup is subdivided into three sections. (1) In-coupling of the probe (and pump) laser beam(s) and modification regarding pointing, power, temporal compression (and overlap), polarization and wavelength, as well as guidance of the out-coupled laser pulses, primarily regarding the separation of the SHG signal from residual pump-, probe beams and illumination photons are outlined in section 2.2.1. (2) Mounting of the sample under protective conditions regarding atmosphere and interfering external light sources but allowing for in- and out-coupling of the laser beams, sample illumination and adjustment and optical verification of spatial overlaps is the topic of section 2.2.2. (3) Detection and analysis of the SHG signal and data procession are outlined in sections 2.2.3 and 2.2.4, respectively.

2.1. Theory: Non-linear Optics

According to Maxwell's equations, a medium exposed to an external electric field gets polarized, i.e., the electrons are displaced with respect to their cores and themselves become sources of the overall electric field $\mathbf{E}$ which satisfies Gauss' law:

$$\nabla\mathbf{E} = \frac{1}{\epsilon_0} \cdot \rho = \frac{1}{\epsilon_0}(\rho_f - \nabla\mathbf{P}), \tag{2.1}$$

where $\rho = \rho_f + \rho_b$ is the sum of free and bound charges (i.e., permanent and induced dipoles) and ϵ_0 is the vacuum permittivity. The macroscopic dielectric polarization of a medium $\mathbf{P}$ is for small electric fields $\mathbf{E}$ given by:

$$\mathbf{P} = \epsilon_0 \chi \mathbf{E}. \tag{2.2}$$

The linear response of the material is thus described by the electric susceptibility χ which in general is a tensor of second order. If the strength of the external electric field is not neglectable in comparison to the atomic Coulomb field, the electron elongation becomes anharmonic and the proportionality between the dielectric polarization and the polarizing electric field is invalid. This is the case for the femtosecond laser pulses applied in the experiments regarding the framework of this thesis. These reach peak intensities on the order of $10^8 \frac{V}{m}$ which is according to Coulomb's law on the order of one per mill of the interatomic electric fields. In this case, $\mathbf{P}$ is expanded in terms of $\mathbf{E}$:

$$P_i = \epsilon_0 \cdot \Big(\sum_j \chi^{(1)}_{ij} \cdot E_j + \sum_{jk} \chi^{(2)}_{ijk} \cdot E_j E_k + \sum_{jkl} \chi^{(3)}_{ijkl} \cdot E_j E_k E_l + \cdots \Big). \quad (2.3)$$

$\chi^{(2)}$ and $\chi^{(3)}$ are the non-linear susceptibilities of second and third order, respectively. The second order non-linear response of a medium to the presence of two laser beams modeled as a plain wave with frequencies ω_1 and ω_2

$$\mathbf{E} = \mathbf{E}_1 \cdot \mathrm{e}^{-i\omega_1 t} + \mathbf{E}_2 \cdot \mathrm{e}^{-i\omega_2 t} + \text{c.c.}, \quad (2.4)$$

where c.c. denotes the complex conjugated, can be evaluated for the simplified example of an isotropic medium (i.e., $\chi^{(2)}_{ijk} = \chi^{(2)}\delta_{ijk}$):

$$\begin{aligned} P^{(2)}_i/(\epsilon_0 \cdot \chi^{(2)}) = &\Big(E^2_{1,i} \cdot \mathrm{e}^{-i2\omega_1 t} + E^2_{2,i} \cdot \mathrm{e}^{-i2\omega_2 t} + \text{c.c.} \Big) \\ &+ 2\Big(E_{1,i} E_{2,i} \cdot \mathrm{e}^{-i(\omega_1+\omega_2)t} + \text{c.c.} \Big) \\ &+ 2\Big(E_{1,i} E_{2,i} \cdot \mathrm{e}^{-i(\omega_1-\omega_2)t} + \text{c.c.} \Big) \\ &+ 2\Big(E^2_{1,i} + E^2_{2,i} \Big). \end{aligned} \quad (2.5)$$

These four terms correspond to the second order non-linear effects of second harmonic generation, sum frequency generation, difference frequency generation (DFG) and electro-optical rectification (EOR), respectively. While in SHG, SFG and DFG laser pulses with frequencies $2\omega_{1,2}$, $\omega_1 + \omega_2$ and $\omega_1 - \omega_2$ are emitted, respectively [141], the EOR creates a DC field with the duration of the excitation. The latter effect can therefore be used to create THz radiation out of a sub-picosecond excitation [142, 143]. By writing down the vector equation for the second order dielectric polarization

$$\mathbf{P}^{(2)} = \epsilon_0 \chi^{(2)} \mathbf{E}\mathbf{E}, \quad (2.6)$$

a special property of second order non-linear effects becomes immediately evident: for systems invariant under inversion symmetry, the $\chi^{(2)}$ tensor has to vanish as otherwise equation 2.6 could for non-vanishing electric fields not be fulfilled. As a consequence, experimental methods exploiting second order non-linear effects as the SHG setup realized in the framework of this thesis are inherently sensitive to surfaces and interfaces as these break the inversion symmetry [5]. In this context, the average inversion symmetry with regard to the wavelength of the probing laser beam is sufficient [144]. Of the complete material response at frequency 2ω [43]:

$$\begin{aligned} \mathbf{P}^{(2)}(2\omega) &= \mathbf{P}^{(2)}_{\text{bulk}}(2\omega) + \mathbf{P}^{(2)}_{\text{surface}}(2\omega) + \mathbf{P}^{(\text{Q})}_{\text{bulk}}(2\omega) \\ &= \chi^{(2)}_{\text{bulk}}(2\omega)\mathbf{E}\mathbf{E} + \chi^{(2)}_{\text{surface}}(2\omega)\mathbf{E}\mathbf{E} + \chi^{(\text{Q})}_{\text{bulk}}(2\omega)\mathbf{E}\nabla\mathbf{E}, \end{aligned} \quad (2.7)$$

the surface dipole term is the only remaining, if the bulk dipole term vanishes due to the mentioned symmetry reasons and the bulk quadrupole term is neglectable. The latter approximation is not generally justified but can usually be applied for thin functional layers investigated in reflection symmetry as discussed for example in [13, 145, 146] and references therein. The approximation is surely valid and the dominance of the $\mathbf{P}^{(2)}_{\text{surface}}$ is term accordingly verified, if observed induced changes in the non-linear susceptibility are: (a) substantial in magnitude and (b) unambiguously attributable to changes in the interfacial electron density. This requirement is for example fulfilled for well-defined photochromic interfaces with large switching-induced NLO contrast or layered structures for which the respective functionality (e.g., charge carrier dynamics) is only observed perpendicular, i.e., not parallel to the interfaces. Therefore, the susceptibility $\chi^{(2)}$ referred to in the remainder of this thesis represents the 'second order non-linear surface dipole susceptibility': $\chi^{(2)} \equiv \chi^{(2)}_{\text{surface}}$. The measured SHG intensity accordingly becomes:

$$\begin{aligned} I_{\text{SHG}}(2\omega) &\propto |\mathbf{P}^{(2)}(2\omega)|^2 \\ &\propto |\chi^{(2)} E(\omega) E(\omega)|^2 \\ &= \Big(|\chi^{(2)}|^2 + \chi^{(2)*}\Delta\chi^{(2)} + \chi^{(2)}\Delta\chi^{(2)*} + |\Delta\chi^{(2)}|^2 \Big) I^2(\omega) \\ &\approx I_0(2\omega) + \Delta I_{\text{ind}}(2\omega, \Delta\chi^{(2)}), \end{aligned} \tag{2.8}$$

where the asterisk denotes the complex conjugated. Here, an induced change in the second order non-linear susceptibility $\Delta\chi^{(2)}$ is introduced. In the last calculation step of equation 2.8 this change is assumed to be small in comparison to the steady state susceptibility which results in an approximately linear correlation between the measured SHG intensity $I_{\text{SHG}}(2\omega)$ and the induced susceptibility change $\Delta\chi^{(2)}$. As the latter in turn is proportional to the number of switched chromophores or the amount of excited electron–hole pairs, important system characteristics as the conversion cross-sections (chapter three) and the relative excitation density (chapter four) can be derived, respectively.

In addition to the three-wave-mixing processes described by equations 2.7 and 2.8, one four-wave-mixing phenomenon arising from the third order non-linear dielectric polarization is important in the framework of this thesis, namely electric field enhanced second harmonic generation (EFISH) [42, 43]. Although this process should *prima facie* only negligibly contribute to an overall signal as $\chi^{(i)} >> \chi^{(j)}$, $j > i$ holds for the non-linear susceptibilities, the EFISH signal becomes important when (a) the involved electric field is strong compared to the probing laser peak intensities and (b) the bulk inversion symmetry is broken by the polarizing DC field. The EFISH contribution is of relevance in the case of charge transfer across a donor/acceptor heterojunction

which leads to the formation of an interfacial electric field E^{DC} and accordingly alters the non-linear response at the SHG frequency 2ω [13]:

$$\mathbf{P}^{\mathrm{NL}}(2\omega) = \mathbf{P}^{(2)}(2\omega) + \mathbf{P}^{\mathrm{EFISH}}(2\omega). \tag{2.9}$$

The generated second harmonic field

$$\begin{aligned} \mathbf{E}(2\omega) &= \mathbf{E}^{(2)}(2\omega) + \mathbf{E}^{\mathrm{EFISH}}(2\omega) \\ &\propto \chi^{(2)}\mathbf{E}(\omega)\mathbf{E}(\omega) + \chi^{(3)}\mathbf{E}(\omega)\mathbf{E}(\omega)\mathbf{E}^{\mathrm{DC}}(0), \end{aligned} \tag{2.10}$$

leads to the detected intensity

$$\begin{aligned} I(2\omega) &= |\mathbf{E}^{(2)}(2\omega) + \mathbf{E}^{\mathrm{EFISH}}(2\omega)|^2 \\ &\approx I(2\omega, E^{\mathrm{DC}} = 0) + \alpha[\chi^{(2)*}\chi^{(3)} + \chi^{(2)}\chi^{(3)*}]I^2(\omega)E^{\mathrm{DC}}, \end{aligned} \tag{2.11}$$

where α is a constant, $\chi^{(i)*}$ denotes the complex conjugated of $\chi^{(i)}$ and a third term quadratic in $\chi^{(3)}$ is already neglected due to $\chi^{(2)} >> \chi^{(3)}$. Therefore, the SHG signal amplitude change arising from the charge transfer is proportional to the interfacial electric field and in the plate capacitor approximation $E^{\mathrm{DC}} = 2Q/A\epsilon_0\epsilon_r$ also to the amount of transferred charge Q [13].

Finally, although not relevant for the investigation of surfaces by means of second order non-linear effects exploiting the inherent interfacial sensitivity, 'phase matching' is of particular importance for tunable femtosecond lasers as outlined in section 2.2.1. In equation 2.4 the position dependence of the electric fields are omitted. When the above described plain wave

$$\mathbf{E}_\alpha = \mathbf{E}_\alpha \cdot \mathrm{e}^{-i(\mathbf{k}_\alpha \mathbf{x} + \omega_\alpha t)} + \mathrm{c.c.}, \tag{2.12}$$

with the wave vector $\|\mathbf{k}_\alpha\| = \omega_\alpha n(\omega_\alpha)/c$, where n and c are the refractive index and the speed of light, respectively, travels through a non-linear, non-centrosymmetric medium, waves with $\mathbf{k}_\gamma = \mathbf{k}_\alpha \pm \mathbf{k}_\beta$ are generated at each point in space which partially annihilate due to the dispersion relation $n = n(\omega_\alpha)$. This destructive interference can be avoided by using birefringent crystals as for instance potassium dihydrogen phosphate (KDP) [147]. In these materials the refractive index $n = n(\omega_\alpha, \xi)$ depends on the crystal orientation ξ and usually exhibits one axis of extraordinary refractivity. Accordingly, the crystal can be oriented to fulfill the phase matching condition for which the differently polarized fundamental and non-linear waves experience equal velocities [148].

2.2. Experimental Setup

The topic of this section is the technical implementation of the SHG experiment, regarding the femtosecond laser setup (section 2.2.1), the experimental

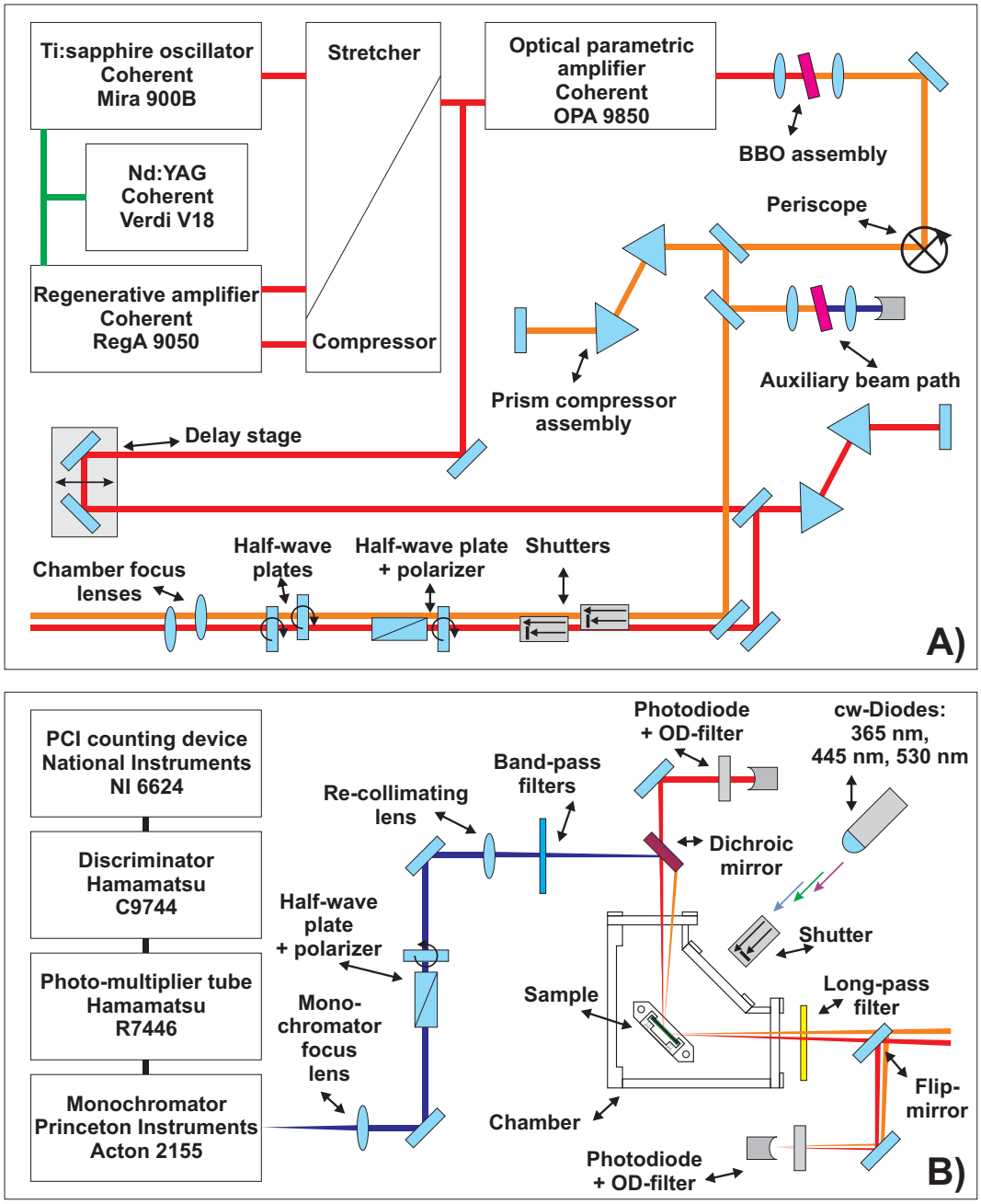

Figure 2.1. (A) Illustration of the laser setup utilized for generation and modification of the 800 nm probe beam (red) and the visible pump beam (orange). (B) Schematic representation of in-coupling of pump and probe beam and cw-illumination, as well as out-coupling, modification and detection of the 400 nm second harmonic beam (blue) and signal processing. (Mechano-) optics not relevant in the framework of this thesis omitted for clarity. Labeled elements are explained in the text. Schemes not according to scale.

chamber (section 2.2.2), light detection and signal processing (section 2.2.3) and data processing (section 2.2.4). An overview on the experimental setup is given in figure 2.1.

2.2.1. Laser Setup

A 300 kHz regenerative amplifier (Coherent RegA 9050) pumped by a Nd:YAG frequency doubled cw-laser (Coherent Verdi V18) and seeded by a mode-locked Ti:sapphire oscillator (Coherent Mira 900B) produces pulses of around 50 fs duration centered at the fundamental wavelength of 800 nm with a spectral width of around 30 nm. In comparison to the oscillator output, this temporal pulse compression is reduced in the amplification process primarily due to inevitable bandwidth losses in pulse-stretching and -compression needed to avoid laser-induced damage to the RegA optics. Nevertheless, the increase in pulse power from around 3 nJ for the 80 MHz oscillator pulse train to the approximately 6 μJ RegA output is essential to enable both, the second harmonic generation probe process and the non-linear conversions in the wavelength tunable pump pulse generation, simultaneously. The latter is done by means of an optical parametric amplifier (Coherent OPA 9850). Through super-continuum and difference frequency generation processes, this device converts the major part of the fundamental beam to near-IR wavelengths between 1050 nm and 1350 nm. The output is subsequently frequency doubled by phase-matched bulk second harmonic generation to visible light of wavelengths between 652 nm and 575 nm in the framework of this thesis. The achievable pulse energies depend on the selected wavelength and are on the order of 80 nJ per pulse. In order to avoid beam damage to the organic samples, it is reduced to below 30 nJ per pulse by de-tuning the focus for the frequency doubling process. The pump beam is pre- and re-compressed by adding negative second order dispersion by means of a pair of highly dispersive prisms (Thorlabs AFS-FS). For rough adjustment, an auxiliary beam path is available which allows for optimizing the temporal compression by means of the yield of another frequency doubling process.

By combining a Glan Thomson polarizer (Thorlabs GTH10M-B) with an achromatic half-wave plate (Thorlabs AHWP10M-980) the probe beam pulse energy is set to values between 100 nJ and 300 nJ, i.e., sufficiently low to avoid beam damage to the organic samples. The pulses are compressed by means of a second pair of highly dispersive prisms (Thorlabs AFS-SF10) fine-tuned to maximize the SHG signal from the sample. This additional modification of the temporal beam profile is necessary as the grid-compressor of the RegA needs to be set to maximize the efficiency of the DFG process for the pump beam generation which has a significant offset in comparison to the probe beam dispersion mostly due to the additional polarizer in the 800 nm beam line.

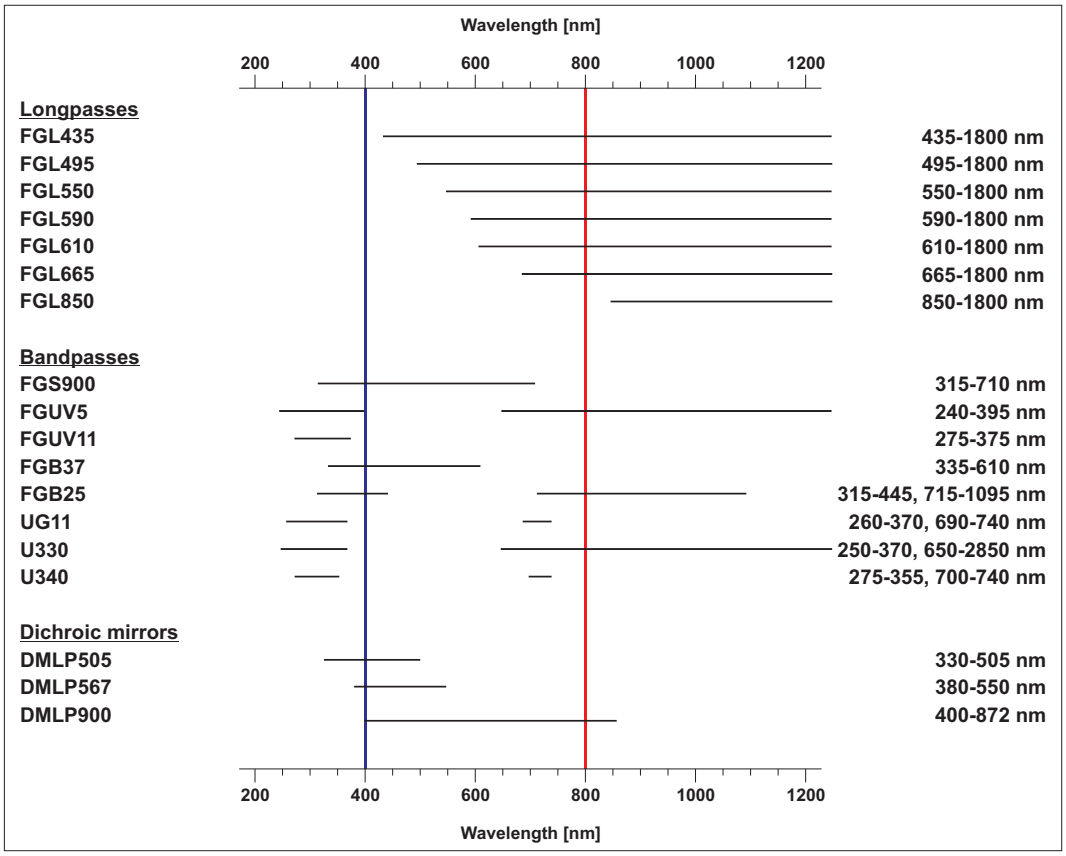

Figure 2.2. Transmittance of the available long- (top) and bandpass filters (center) as well as reflectivity of the dichroic mirrors (bottom) at the experimentally relevant wavelengths. The fundamental and SHG wavelengths are indicated in red and blue, respectively.

A variable temporal delay between the two beam lines is introduced by means of a piezo driven automatic stage (PI M-505.4DG). The 100 mm free path of the stage allows for the introduction of up to 667 ps total delay in step sizes of approximately 0.11 fs. Mismatches in the temporal overlap of up to ± 0.3 μs can therefore directly be accounted for by searching for the sum frequency generation signal at a highly non-linear GaAs (gallium arsenide, Wafer Technology, undoped single crystal, orientation (100)$\pm 0.1°$, polished) reference sample (section 2.3.1). For larger temporal offsets, an auxiliary beam path of equal length is available at which both beams are focused onto a photodiode (Thorlabs DET110). Thus searching for the temporal overlap on microsecond timescales by means of an oscilloscope is enabled (LeCroy Waverunner, 0.05 ns resolution). As a home-built non-collinear optical parametric amplifier (NOPA), which covers a different spectral range (480 nm to 600 nm) in com-

parison to the IR-OPA, also is in temporal overlap with the probe beam, the delay stage is incorporated to vary the probe beam path length. SHG signal instabilities originating from stage motion are not observed despite thoroughly conducted investigations.

Two half-wave plates (Thorlabs AHWP10M-600, AHWP10M-980) are used to vary the pump and probe beam polarization, respectively. The polarization of the SHG signal is read out by means of a half-wave plate (Thorlabs AHWP10M-600) in combination with a polarizer (B. Halle PRQ).

Pump and probe beam are focused onto the sample using two N-BK7 bi-convex lenses (Thorlabs LB1391-A and -B, respectively). The focal lengths of 400 mm allow for a focal diameter of up to 200 μm. The focus is set by means of manual delay stages to maximize the SHG signal and to pump an area slightly larger than the probed spot, respectively. Both beams travel through a long-pass colored glass filter (Thorlabs FGL435L) immediately before reaching the sample which cuts off undesired wavelengths shorter than 435 nm, i.e., close to the SHG wavelength of 400 nm.

The fundamental and the SHG beam are separated by means of a dichroic mirror (Thorlabs DMLP505) through which the residual 800 nm beam is transmitted and subsequently detected using a photodiode (Thorlabs SM1PD1A, Si: 350 nm – 1100 nm) to measure the linear reflectivity of the sample (*vide infra*). The dichroic mirror reflects the 400 nm SHG pulses towards the monochromator. The pump beam does not reach the monochromator, as it is impinging under a small angle with respect to the sample surface normal, while the probe beam passes the sample horizontally. In addition, sets of colored glass filters are applied as even stray light is often significantly more intense than the SHG signal. The available filters, band-passes and dichroic mirrors are depicted in figure 2.2. For the experiments conducted in the framework of this thesis a set of the following three filters has been used: FGS900, FGB25 and FGB37. The SHG beam is re-collimated (Thorlabs LB1391-A) and focused into the monochromator using an N-BK7 bi-convex lens with a focal length of 150 mm (Thorlabs LB4965-A), thus matching the distance between entrance slit and monochromator grid.

Three monochromatic diodes which emit at 530 nm (Thorlabs M530L2), 445 nm (Newport LQN445-50C) and 365 nm (Thorlabs M365L2) are available for illumination experiments. Home-built, automatized shutters can be incorporated to sequentially control pump and probe beam and the illumination diodes.

2.2.2. Experimental Chamber

Protection of sample and monochromator against external light sources is ensured by means of a box built from anodized aluminum rods, PVC plates

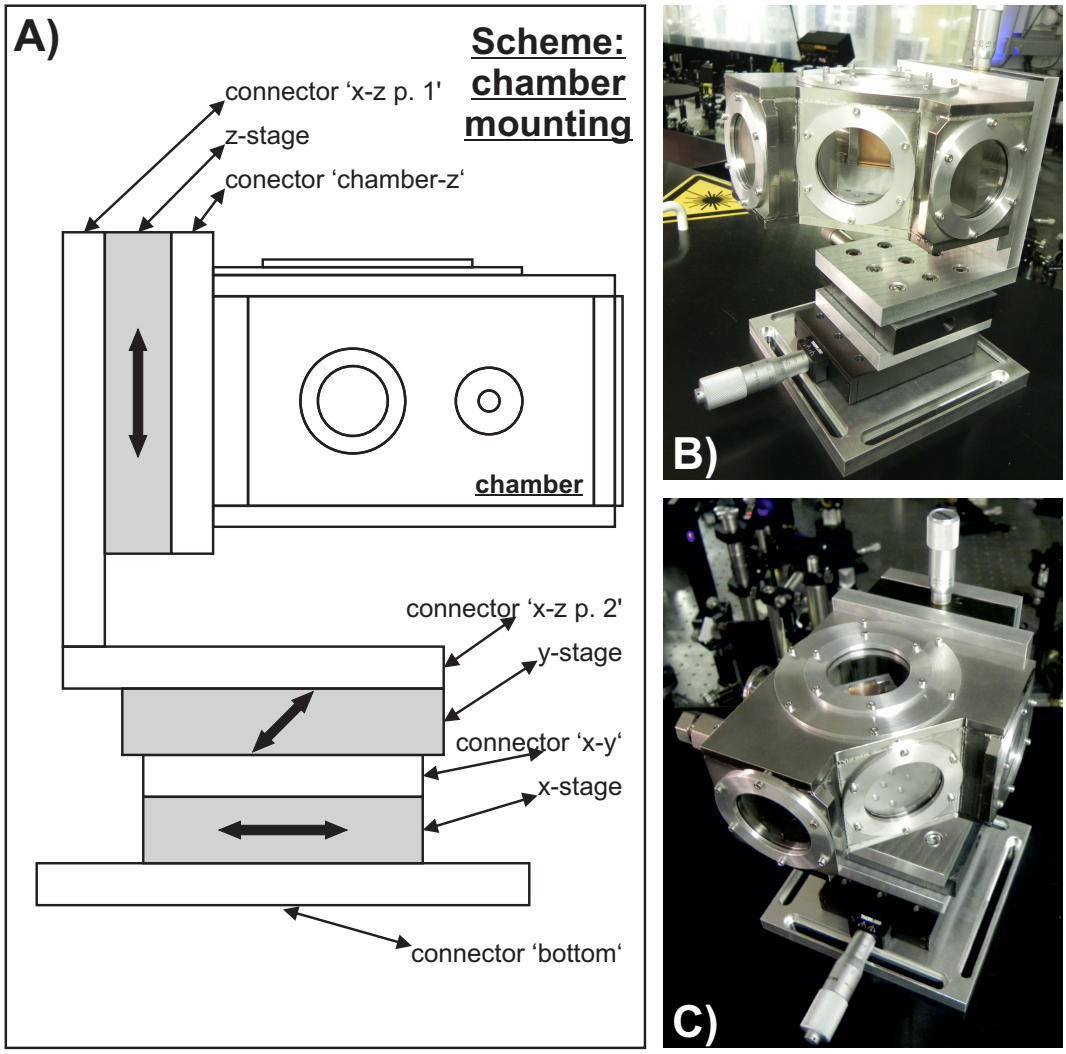

Figure 2.3. Schematic side view (A) and photographs (B, C) of the home-built experimental chamber. Three manual delay stages enable sample positioning. Exchanging the sample is accomplished by removing the top cover. The whole chamber can be unscrewed at the 'chamber-z'-connector for sample mounting inside of a glove box. A VCR and an ISO-KF flange allow to establish an inert gas atmosphere. Three view ports allow for simultaneous laser in- and out-coupling as well as illumination or microscope based observation.

and fireproof fabric. The home-built experimental chamber is depicted in figure 2.3. Drawings of the prime functional components are shown in figures 2.4, 2.5 and 2.6, respectively. The chamber was designed to fulfill the following purposes. (1) The sample position needs to be controllable on all three axes. (2) Besides the accessibility for the laser beams, the possibility for simultaneous illumination or microscope based sample observation is required. (3) To avoid the exposure of the organic samples primarily to oxygen and water, the sample needs to be mounted under protective gas atmosphere. (4) The possibility to quickly switch samples is desired. (5) Mounting two samples simultaneously enables direct referencing and simplifies the determination of time zero, i.e., the time delay setting at which pump and probe pulse trains are in temporal overlap (section 2.3.1).

Three manual delay stages (Standa 7T67-25) allow sample positioning with a precision of one micrometer within a range of 25 mm, which corresponds to the dimensions of the sample back plate (*vide infra*). The sample is mounted under an angle of 45° with respect to the incident laser beams. The possibility of controlling of the sample position on both axes which span the laser beam plane accordingly renders a readjustment of the outgoing beam path subsequent to sample repositioning unnecessary.

The windows for laser in- and out-coupling are made of optically polished, 3.0 mm thick CaF_2 (Korth CaF_2-UV) which is transparent between 130 nm and 1200 nm. The experimental chamber dimensioning is strongly restricted by the demand for a third view port through which the sample is not only accessible by the monochromatic diodes in illumination experiments as depicted in figure 2.4A. The central window is also used for the rough adjustment of the laser spot overlap in pump–probe experiments (while the fine adjustment is done by optimizing the SFG signal, section 2.3.1). The restriction arises from the 95 mm working distance of the trinocular stereo microscope (LOMO SF-100T) through which the laser spot overlap on the sample is monitored *via* the diffusely scattered part of the laser light. Figure 2.6B shows the laser beams out of overlap on a GaAs reference sample captured by means of a CCD camera (The Imaging Source DMK 21AU04) connected to the microscope.

Preventing the exposure of the samples to air is necessary for the investigation of most organic samples. It is for example known that P3HT:PCBM based organic solar cells degrade upon oxygen [149] and water exposure [150] and that the resulting loss in charge carrier mobility reduces the OPV efficiency [151]. To establish an inert gas atmosphere (nitrogen, purity '5.0'), a DN 16 ISO-KF and a 6LV-4-VCR-3S-6MTB7 (with SS-4-VCR-1 counter) flange are available as shown in figure 2.5A. 2.0 mm thick nitrile butadiene rubber O-ring seals (Reiff O-Ring NBR 70) are used in 1.6 mm and 1.3 mm deep flutes on both sides of each window and for the removable top cover, respectively (cf. figures 2.4B and 2.5B, respectively), to seal the welded stainless

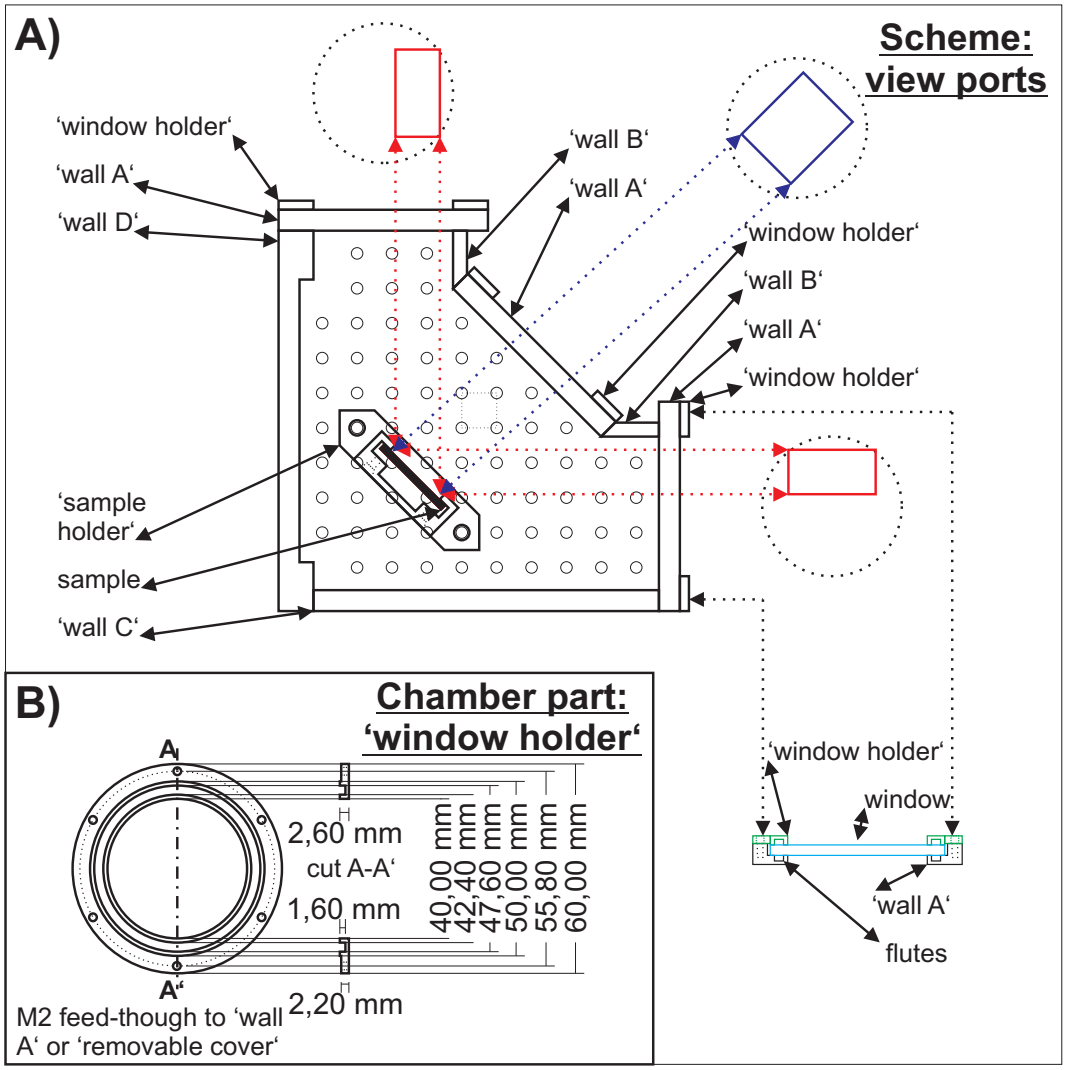

Figure 2.4. (A) Top view of the experimental chamber including laser and illumination view lines to the sample shown in red and blue, respectively. The prime design issue is the simultaneous sample accessibility by either probe beam and a cw-diode or by pump and probe beams in TR-SHG experiments. The latter restricts the distance between sample and central window to 95 mm corresponding to the working distance of the microscope, needed to monitor the spatial laser overlap. (B) Technical drawing of the 'window holder' designed to maximize view port diameters and to minimize the samples distance to the microscope by countersinking the windows into the chamber walls.

steel chamber.

The sample holder is modularized to facilitate a fast sample exchange. The body part shown in figure 2.6A is extractable from the experimental chamber through the chamber cover which is removable as shown in figure 2.5. A 25 mm by 25 mm copper plate (Gemmel OF-Cu-CW008A, 99.95 % purity) is slid into the body part and tightened to the vertical front nibs by means of rearward screws. Two samples of sizes up to 12 mm by 12 mm can be mounted simultaneously to the copper back plate. This allows for fast referencing by solely altering the z-axis position of the chamber. A sample holder carrying an adsorbate covered sapphire plate and a GaAs wafer fragment (section 2.3.1) is shown in figure 2.6C.

For the photochromic interfaces investigated in the framework of this thesis, the attachment strategy based on self-assembled monolayer formation dictates the choice of the substrate, *viz.* gold and silicon as discussed in section 3.1.3. In contrast, for thin functional films prepared by spin coating or vacuum evaporation, optically polished sapphire substrates (CrysTec, (0001)-orientation) are chosen due to a vanishing (interfacial) SHG response and a high thermal conductivity in contrast to glass substrates [152].

Establishing temperature control by thermally isolating the sample holder against the chamber and by attaching a Peltier-element and a thermocouple, actuated and read out *via* a feed-through in the ISO-KF flange, will be the subsequent step facilitated by the sample holder design and the choice of materials.

The technical drawings of the residual experimental chamber parts are shown in appendix B.

2.2.3. Light Detection and Signal Processing

The SHG and SFG signals are detected by means of a photo-multiplier tube (Hamamatsu R7446) attached to a monochromator (Princeton Instruments Acton 2155). The monochromator focal length is 150 mm which results in a wavelength resolution of 0.4 nm using a 32 mm by 32 mm grating with 1200 grooves/mm and a 300 nm blazing. The grating efficiency is between 65 % and 70 % at the wavelengths of 400 nm and 333 nm, which correspond to the SHG signal from the 800 nm probe beam and the shortest SFG wavelength detected in the framework of this thesis, respectively.

The photo-multiplier tube responds to wavelengths between 160 nm and 680 nm. It has its peak quantum efficiency of 19 % corresponding to a photocathode sensitivity of 60 mA/W at the wavelength of maximum response of 400 nm. The typical amplification is $6.7 \cdot 10^6$. The maximum supply voltage of 1250 V is uniformly distributed among the circularly arranged nine dynode stages between cathode and anode. The minimum dark count rate is specified

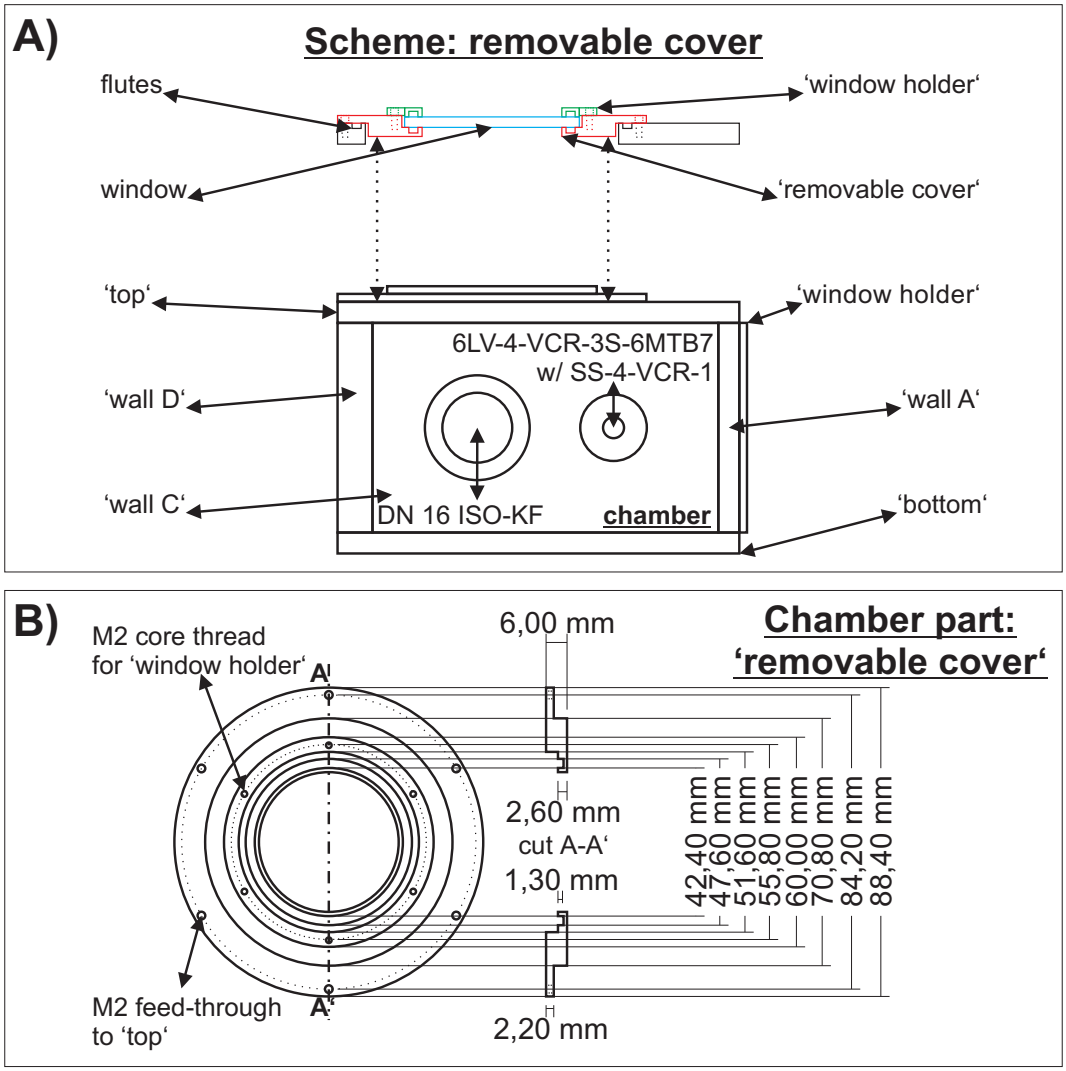

Figure 2.5. Schematic side view (A) and technical drawing (B) of the 'removable cover'. The sample holder is extractable through an opening with 71 mm diameter when the cover is removed. An additional top view port provides accessibility for an IR-viewer.

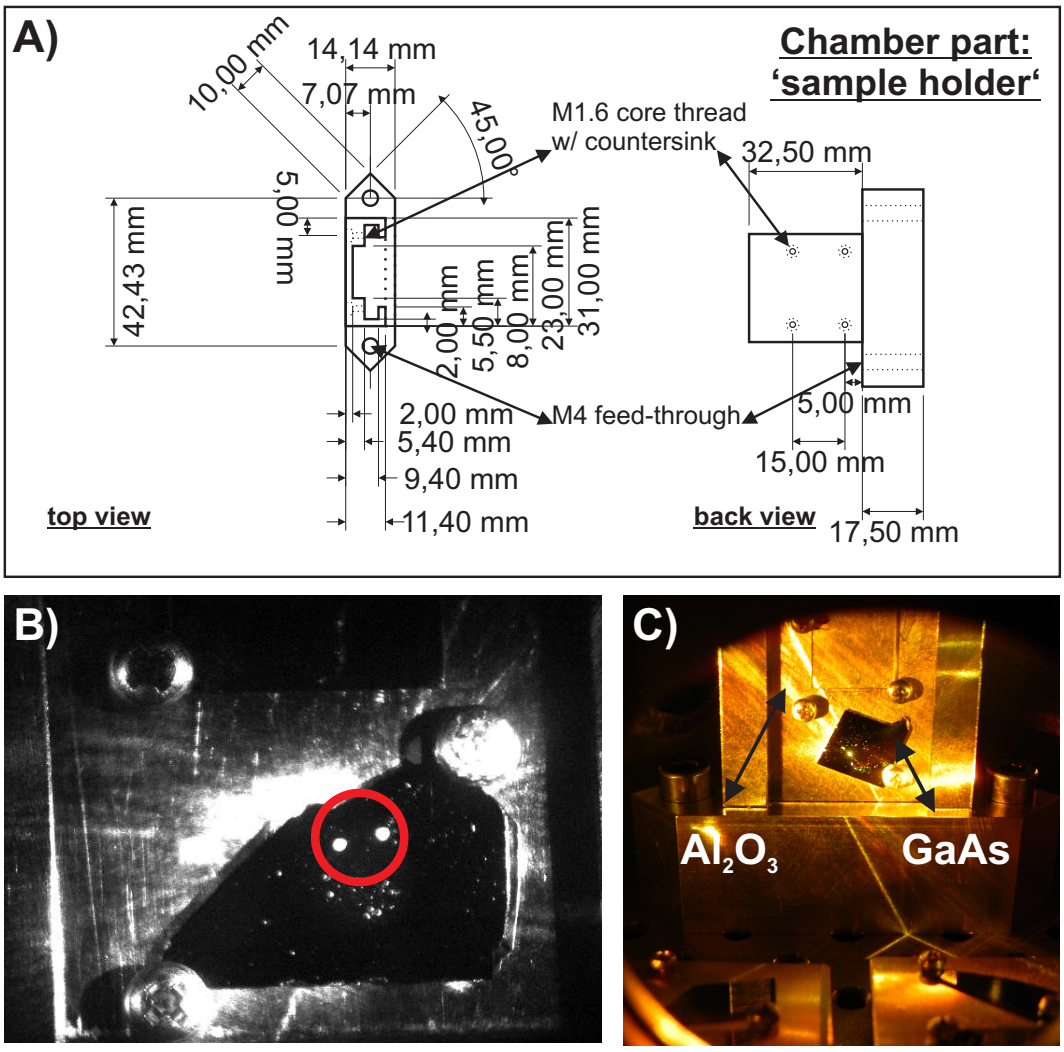

Figure 2.6. (A) Technical drawing of the sample holder. The copper base plate is slid-in from the top and tightened to the vertical front nibs by means of rearward screws. (B) Photograph of a GaAs reference sample taken by the CCD camera attached to the trinocular microscope. The laser beams marked in red are not in overlap. (C) Photograph of a twin sample holder carrying an adsorbate-coated sapphire sample (top) and a GaAs reference (bottom).

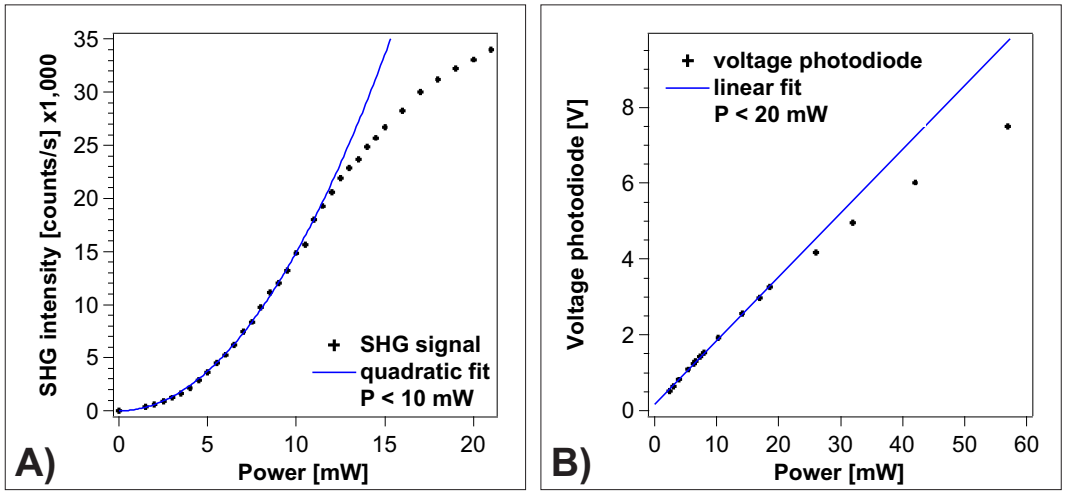

Figure 2.7. (A) SHG data obtained for an inorganic GaAs sample. As indicated by the fit (blue) the signal amplitude correlates quadratically with the probe beam power and accordingly with the number of probing photons. Above 20,000 counts/s the inability of the photo-multiplier tube to detect several photons per laser pulse results in an increasing deviation from the quadratic correlation. (B) The photodiode utilized to monitor the linear optical sample response *via* the reflectivity, saturates above 20 mW residual power.

to ten counts per second. The temporal response is limited by the electron transition time which is on the order of 22 ns. This is on the one hand well below the laser repetition rate of 3.33 μs but does on the other hand not allow to detect several photons per femtosecond pulse. The restriction to the detection of one event per laser pulse leads to the practical limitation of the count rate to roughly a tenth of the laser pulse frequency. Otherwise the Poisson approximation to the binomial distribution becomes inadequate as the probability of multiple events per pulse is no longer neglectable [153]. This is in correspondence with the experimental findings on a GaAs sample illustrated in figure 2.7A. For the inorganic sample the number of generated SHG photons should correlate quadratically with the number of probing photons, the latter being proportional to the probe beam power. As indicated by the fit to the data for powers below 10 mW, this is the case for up to 20, 000 counts/s, above which an increasing deviation from the quadratic correlation is observed. Although analytical schemes for the extension of the 'linear dynamic counting range' exist [154], count rates requiring such statistical treatment are not encountered for the probe beam powers applicable for the non-destructive investigation of organic samples in the framework of this thesis. Finally, the principal choice for the counting mode instead of analogous data acquisition is obvious from the encountered SHG signal intensities.

A counting unit (Hamamatsu C9744) is used to discriminate electronic noise against actual events by comparing the current pulses coming from the photo-multiplier tube after pre-amplification to a tunable discrimination level. It thus converts the analogous signal input into digital TTL (transistor–transistor logic) voltage levels at the output connector to the PCI data acquisition card (National Instruments NI 6624). The discrimination level is set to U_D = 126.0 mV for the experiments conducted in the framework of this thesis. This value corresponds to the expected ten dark counts per second from the photo-multiplier tube.

The supply voltage to the photo-multiplier tube is set to U_S = 800 V for the conducted experiments by means of a high stability power supply (Knott NSHV -3.5 BN649 S/N 343). This value corresponds to the center of the working plateau of the tube, i.e., the voltage at which the probability for a single photoelectron to start an electron avalanche is maximized while the likelihood of an electron cascade due to emission of electrons from the dynodes mediated by the electric field is still neglectable. The working plateau is determined by stepwise measuring the count rate under illumination as a function of the supply voltage. Accordingly, the system parameters U_S and U_D need to be found iteratively if electronic components of the setup are exchanged.

The monochromator–tube–discriminator assembly is protected by a μ-metal shielding (Meca Magnetic, 1 mm thickness), i.e., a box constructed of an alloy of 80 % nickel, 15 % iron and 5 % molybdenum which shields the sensitive electronic components against magnetic fields due to the relatively high magnetic permeability. This is primarily necessary as the sensitivity of the photon counting unit to electronic pulses of approximately 5 ns duration (the rise-time of the R7446 is specified to 2.2 ns, the fall-time is comparable) demands for a fast-switching electric circuit which is, in turn, susceptible to external magnetic fields.

As mentioned above, in addition to the primary SHG (or SFG) signal, the linear sample response is measured in terms of its reflectivity by means of a photodiode. This allows for monitoring the laser system stability as the linear reflectivity is considerably less sensitive to the interface in comparison to the second order non-linear SHG process. The signal is acquired *via* an analogous input port of the PCI device in terms of the voltage which drops across a 330 Ω series resistor. Proportionality between current and light intensity is ensured by reversely biasing the photodiode with a diode voltage of U_{Diode} = 10.0 V. The AC part of the diode's response to the pulsed laser is averaged out by means of a 470 nF capacitor operated in parallel. To avoid saturation of the photodiode, additional optical filters are applied to reduce the power of the reflected beam behind the dichroic mirror to below 20 mW in accordance with the measured saturation curve shown in figure 2.7B.

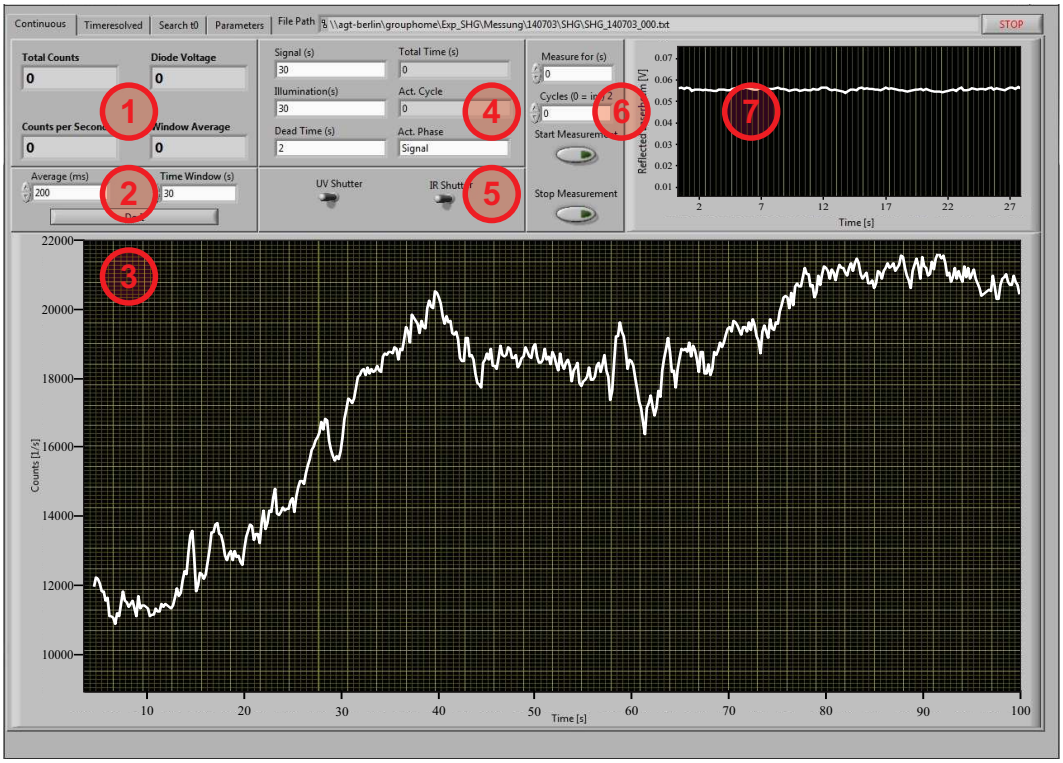

Figure 2.8. Program interface for continuous and sequential measurements. Controls and indicators regard: (1) total, actual and average count rate and current diode voltage, (2) integration time and display history, (3) SHG intensity, (4) sequential settings, (5) shutter settings, (6) measurement duration or number of iteration cycles and (7) diode voltage history.

2.2.4. Data Processing

The basic interface of the measuring program is depicted in figure 2.8. The program was developed in NI LabVIEW 10 which is the native programming language equipped with the PCI acquisition device. The input is an integer representing the physical counter which upon activation increments for each TTL pulse from the counting unit. The most rudimentary form of converting this input into an evaluable data stream is to incorporate the system time to convert the 'counts' to 'counts per second'. The temporal quantization is not necessarily one second as fast changes in the signal amplitude could be masked. The integration time should flexibly be chosen for each measurement according to the signal-to-noise ratio and the 'counts per interval' correspondingly need to be interpolated to 'counts per second'. A value of 200 ms was found to be favorable for count rates on the order of $1,000$ counts/s.

The data are displayed and saved to plain text files in terms of two dimen-

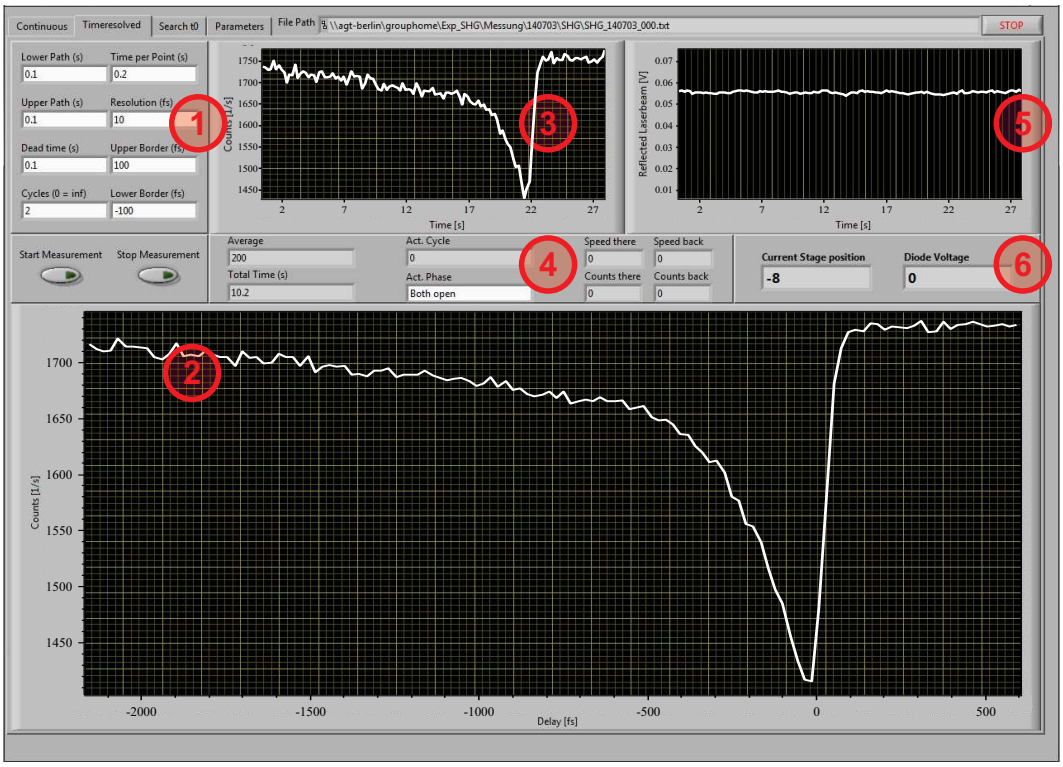

Figure 2.9. Program interface for time-resolved measurements. The controls and indicators regard: (1) maximum delays, resolution, integration time and background, (2) averaged TR-SHG intensity, (3) current TR-SHG intensity, (4) calculated measurement and delay stage parameters, (5) diode voltage history and (6) current relative delay stage position and diode voltage.

sional arrays containing pairs of 'counts per second' *vs.* 'time', the latter being the difference between the actual system time and the starting system time in intervals of the integration time. Additionally, the analogous voltage input from the referencing photodiode is displayed and saved in the same intervals. The simultaneous availability of the linear and the non-linear sample response has proven to be useful to detect misalignments in the laser system. For instance, a rising SHG signal amplitude upon tuning the prism compressor due to an optimized temporal compression of the laser pulses, accompanied by a decrease of the reflected light intensity indicates a beam-clipping at the edge of one of the prisms and an according loss in bandwidth.

Apart from measuring the SHG (or SFG) signal continuously or for a preset interval, primarily regarding the switchable samples, another measuring mode is implemented in which the program iteratively cycles through measurement and illumination phases. Mechanical shutters controlled *via* analogous outputs of the PCI device are automatically opened and closed for example to inves-

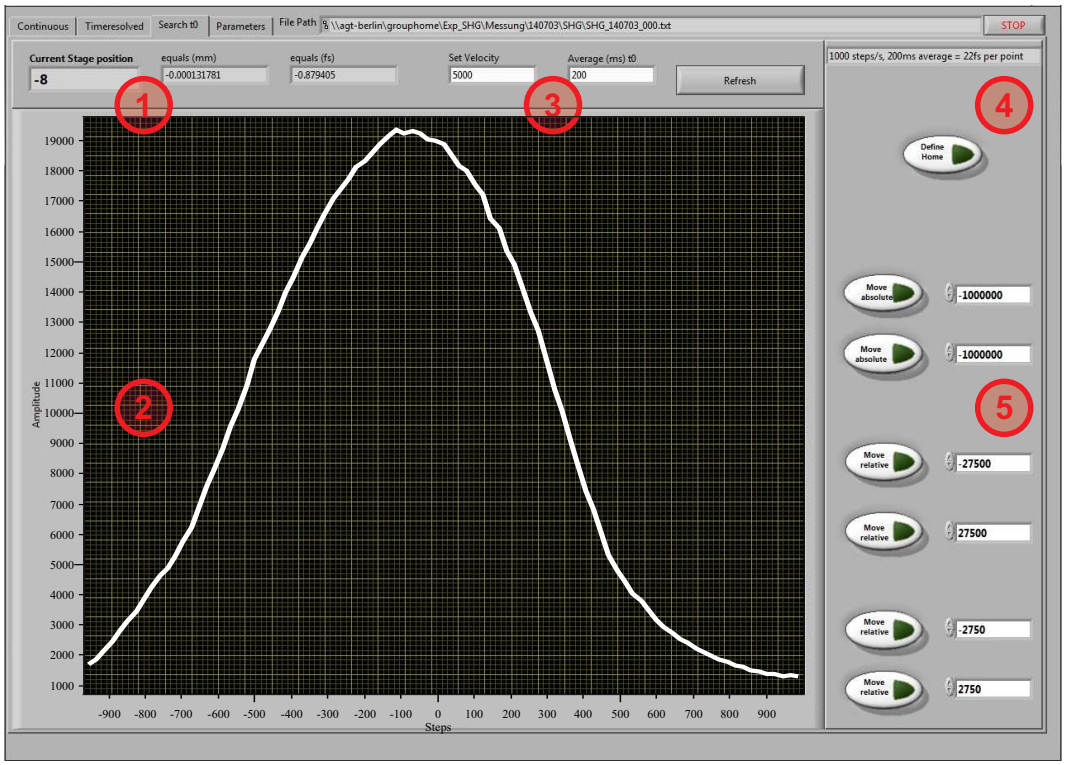

Figure 2.10. Program interface for manual delay stage control. The controls and indicators regard: (1) current delay stage position, (2) SHG or SFG intensity, (3) stage velocity and integration time as well as display history reset, (4) define home control and (5) preset delay stage positions.

tigate a stepwise switching of a sample. Dead times in which both shutters are closed are implemented to account for the time the mechanical apertures need to move. Alternatively, manual control of the shutters is provided. The termination condition for each non-continuous measurement is checked in real time for every iteration of the inner loop which corresponds to measuring, displaying and saving of one data point.

For the time-resolved measurements an iterative data acquisition is designated. The corresponding program interface is shown in figure 2.9. Measuring iteratively simplifies the detection of possible beam damage in pump–probe experiments which is highly relevant for the investigation of organic samples. It also allows to adapt the integration time during long term measurements by adding or removing iteration cycles during the measurement. The recorded data for an iteration is weighted against the preceding cycles to form the average which is subsequently written to a new file to enable the accessibility of both, the overall average and each individual cycle's data. This is also done for the delays which are calculated from the relative actual delay stage

position acquired for each data point individually and the system time, i.e., in real time. Both the data of the actual cycle and the overall average are displayed simultaneously to simplify the detection of possible beam damage. Through automatized shutter control, signal backgrounds arising from both laser beams are acquired, while the delay stage resets between the cycles. Besides the maximum positive and negative delays and the number of iterations, the measurement accuracy needs to be set in terms of delay step width and the data acquisition time for each step. While the former defines the resolution, the latter corresponds to the integration time regulating the signal-to-noise ratio as stated above.

In addition to the automatic mode, the delay stage may also be controlled manually to facilitate the detection of time zero. The program panel providing this functionality is illustrated in figure 2.10. Although the SFG signal is displayed as a function of the delay in this mode, the actual termination condition is the preset final delay stage position. For the correctly aligned setup, time zero is with certainty detected for the highly non-linear GaAs sample at a velocity of $10,000$ steps/s, corresponding to 1.1 ps/s scanning speed.

The basic development was done using the 300 kHz RegA output frequency as reference, detected by means of a fast photodiode. Proof of principle is given by the data presented in figure 2.11: the cross-correlation of pump and probe pulse deduced by means of the SFG signal is on the order of 50 fs which is according to the laser system parameters (figure 2.11A) and the SFG and SHG wavelengths of 339 nm and 401 nm are as expected for pump and probe wavelengths of 586 nm and 800 nm, respectively (figure 2.11B). Furthermore, the SHG count rate scales quadratically with the probe beam power (cf. figure 2.7A).

2.3. Experimental Procedures

The two basic conductible measurement modes are time-resolved SHG (section 2.3.1), i.e., the observation of pump-induced exciton dynamics on a femtosecond timescale and illumination experiments (section 2.3.2) in which the interfacial electron density is statically altered by addressing photochromic units with the appropriate illumination wavelengths. In both cases additional geometric information is obtainable by controlling the laser beam polarizations (section 2.3.3). Furthermore, TR-SHG is conductible in a spectroscopic mode by varying the pump beam wavelength (section 2.3.4).

2.3.1. Time-resolved SHG

Assuming pump and probe beams are set to the desired wavelengths, roughly temporally compressed and aligned to hit the sample and the supply- and

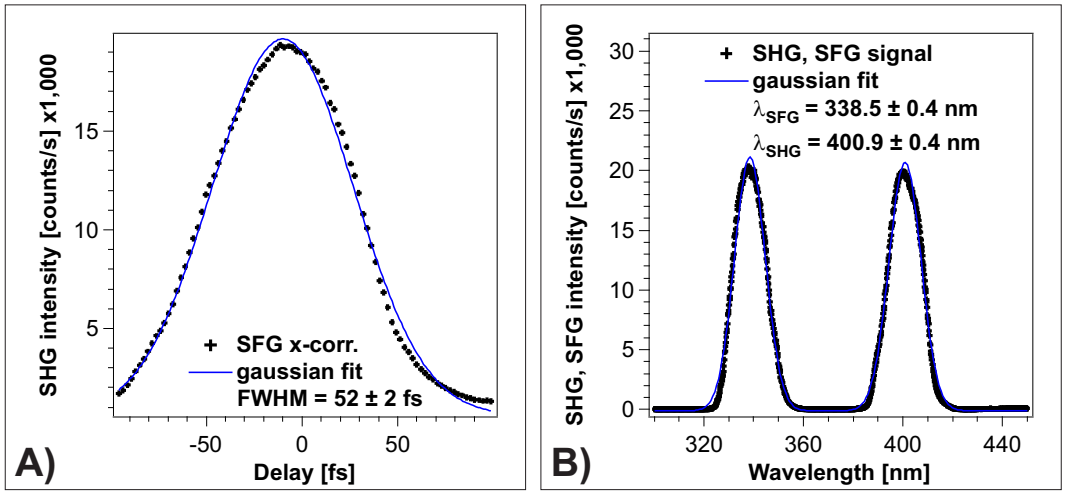

Figure 2.11. (A) The width (FWHM) of the cross-correlation of the SFG signal shown in (B) and accordingly the temporal resolution of the respective pump–probe experiment is 52 ± 2 fs. (B) Turning the monochromator grid in an automatized mode, enables to measure the wavelengths of SFG and SHG beams. The determined wavelengths of 339 nm and 401 nm are as expected for pump and probe wavelengths of 586 nm and 800 nm, respectively. Both data sets measured for an inorganic GaAs sample.

discrimination voltages are appropriately adjusted as outlined in the previous section, a time-resolved SHG experiment is set-up as follows. (1) The spatial overlap of pump and probe beam on a GaAs reference sample (*vide infra*) is established *via* observing the diffusely refracted laser spots by means of the microscope (cf. figure 2.6B). (2) The SHG beam is focused into the monochromator set to 400 nm by flipping the filter set out of the outbound beam path and adjusting on the fraction of the 800 nm probe beam reflected of the dichroic mirror by means of an IR-viewer. (3) With the filters flipped back into the outbound beam path, the SHG signal amplitude is maximized by fine tuning the monochromator in-coupling and by optimizing the temporal compression of the 800 nm prism compressor. (4) The temporal overlap is established by manually controlling the delay stage (figure 2.10) to find time zero with the monochromator set to the SFG wavelength. The highly non-linear GaAs reference sample allows for a simplified detection of time zero due to its strong SHG and SFG (bulk) responses as the crystal structure inheres no inversion symmetry [155]. (5) Iteratively reducing the width of the cross-correlation with the pump beam prism compressor and increasing the SFG signal amplitude by fine tuning the pump beam pointing, optimizes the temporal and spatial overlap between pump and probe beam. (6) The chamber z-stage is utilized to switch from the GaAs reference to the actual sample. With the monochro-

mator set back to 400 nm, the fine tuning of the in-coupling is repeated. (7) Finally, the sample is checked for homogeneity, beam damage and undesired non-linear effects like exciton–exciton annihilation (*vide infra*) [156–158] and pump and probe beam powers are accordingly set.

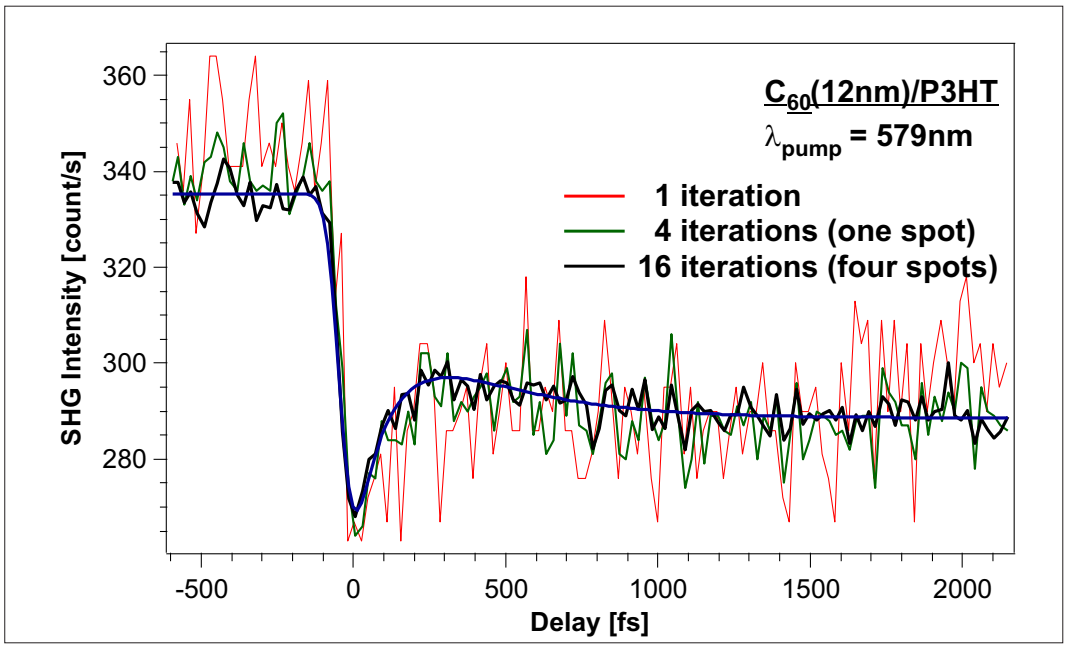

Figure 2.12. The signal-to-noise ratio significantly improves while the observed dynamics and the SHG intensity remain unaltered during four iterations (red to green) and by averaging among four spots (green to black).

An improvement of the signal-to-noise ratio should be achieved by measuring both iteratively and repetitively at different sample spots. As shown in figure 2.12, the quality of the TR-SHG data significantly improves from the first to the fourth cycle and further by averaging the data measurement at four different spots. The prime advantages of this approach are the exclusion of beam damage by comparing the current iteration to the averaged data (cf. control panel shown in figure 2.9) and the surveillance of homogeneity. Furthermore, dynamics at short and large delays should be measured separately to allow for applying different resolutions which results in comparable exposure times for different measurements.

A variation of the pump beam power yields information on the relative amount of excited electron–hole pairs, i.e., according to equation 2.8 a linear correlation between the numbers of pump photons and initially excited excitons exist, if two conditions are fulfilled. (1) The observed pump-induced TR-SHG signal amplitude changes have to be small in comparison to the steady state signal level. (2) The pump beam power has to be sufficiently low to exclude

undesired non-linear effects as exciton–exciton annihilation [156–158] or even a thermal modulation of the absorbance which has been observed for P3HT at very high excitation densities [159].

The data are processed by normalization to the average SHG intensity at negative delays, i.e., the probe beam advances the pump beam, and by averaging equal measurements conducted for different sample spots. The evaluation is subsequently done by means of a generalized fitting routine implemented in Igor Pro 6.02A which iteratively convolutes the Gaussian cross-correlation profile (cf. figure 2.11A) with the following set of functions accounting for the dynamic response of the sample to the excitation. (1) Up to three exponential functions model different excitonic de-excitation and recombination pathways. (2) The (analytic) bi-exponential solution to a three-state coupled rate equation describes the delayed population of an intermediate state (e.g., the charge transfer state) out of an initially excited population:

$$\frac{\tau_2 \cdot \tau_1}{\tau_{1\to 2} \cdot (\tau_1 - \tau_2)} \cdot \left(\exp\left(-\frac{t - t_0}{\tau_{1\to 2}}\right) - \exp\left(-\frac{t - t_0}{\tau_2}\right) \right), \tag{2.13}$$

where τ_1, τ_1 and $\tau_{1\to 2}$ are the time-constants for the initial and final state and the coupling constant, respectively. (3) A step function accounts for excitonic species which decay on timescales considerably longer than the delays applied in the measurement.

2.3.2. Illumination Experiments

Illumination experiments are conducted by sequentially illuminating the photochromic samples with monochromatic diodes of appropriate wavelengths to drive the isomerization. The according change in the second order non-linear susceptibility arising from static charge redistribution and geometric (π-electron system) rearrangement, is measured by means of the SHG signal amplitude. These experiments are conducted for the *trans* $\leftrightarrow$ *cis* isomerization of an azobenzene-functionalized SAM using a 365 nm and a 445 nm diode, respectively. In ethanolic solution, illumination at 365 nm almost exclusively excites the *trans*-isomers. In contrast, no absorption band solely inherent to the *cis*-form exists and the excitation at 445 nm is accordingly chosen as the difference in the absorption spectra of both isomers is maximal at this wavelength [160]. Although the absorption bands differ considerably for different chromophore environments [161], these wavelengths appear to be suited for the azobenzene SAMs, as well [162]. For the ring-opening reaction and the Z $\leftrightarrow$ E $\leftrightarrow$ C conversion of a fulgimide-functionalized SAM, a 530 nm and a 365 nm diode are available, respectively. Although when solved in benzene, each of the investigated fulgimide forms absorbs UV light at 365 nm, the absorption band of the E-form is dominant at this wavelength. In contrast, light

of 530 nm wavelength is exclusively absorbed by the colored C-fulgimide [163]. While no results on UV/visible spectroscopy measurements on the investigated fulgimide SAM are available to date, the applicability of these wavelengths to trigger the reversible isomerization has been demonstrated for this [80] and a similar system [164].

The respective photostationary states are represented by a certain SHG signal amplitude $I_{\mathrm{SHG}}(\mathrm{PSS})$. According to equation 2.8 the intermediate signal levels correlate approximated proportional to the percentage of switched molecules: $I_{\mathrm{SHG}} \approx I_{\mathrm{SHG}}(\mathrm{PSS}) + \Delta I_{\mathrm{SHG}}$. Evaluating the transient signal amplitude as a function of the applied photon dose n_{P} by means of a saturation function

$$\Delta I_{\mathrm{SHG}} = \Delta I_{\infty} \cdot \Big[1 - \exp(-\sigma \cdot n_{\mathrm{P}})\Big], \tag{2.14}$$

thus yields the effective switching cross-section σ. Confusion needs to be avoided here, as the change in the SHG signal amplitude is indeed proportional to the number of contributing chromophores according to equation 2.8, as equation 2.14 describes the (induced) modification of the second order susceptibility and not of the (inducing) electric field. This formula is of course only applicable if single switching events are independent of each other. In contrast, a cooperative switching of whole islands of another azobenzene-functionalized self-assembled monolayer *via* nearest neighbor interactions has been observed [165]. Furthermore, the cooperative denaturation of azobenzene-functionalized foldamers subsequent to single molecule isomerization has been reported [166]. Finally, it has to be remarked that the detection limit of a cooperative switching behavior is limited by the number of chromophores needed to resolve a switching even against the background which originates for example from the conjugated electron system of an alkyl chain. If for instance the above described free behavior would be preceded by switching single 'active grains' within each island, i.e., a two-step isomerization process, this would probably not be resolvable. The resolution of the SHG setup developed and realized in the framework of this thesis can be estimated by considering the large platform SAMs [96] which were also investigated and for which no switching event has been resolvable. However, the chromophore density in these systems is on the order of 2.4 molecules per square nanometer [167] and hence an order of magnitude lower in comparison to the photochromic interfaces described in chapter three [80, 99, 102]. Considering these results, the resolution of the present SHG setup is estimated to be on the order of one to ten molecules per square nanometer, given first hyperpolarizabilities comparable to the investigated chromophores. As a side note, different end-group modifications of the azobenzene chromophore in these experiments by means of methyl, methoxy and trifluoromethyl groups did not improve the resolvability.

Besides automatized sequential illumination measurements for the deter-

mination of the switching cross-sections, the second conductible illumination experiment is the iterative complete switching between the respective photostationary states over several cycles. From these measurements the reversibility of the isomerization processes can be deduced from the reproducibility of the SHG signal amplitudes representing the respective photostationary states. By introducing additional waiting times, the thermal stability of the isomers incorporated in the respective self-assembled monolayers is observable. As these measurements last several hours, monitoring the stability of the laser system by measuring the linear reflectivity of the sample is obligatory as outlined in section 2.2.3.

2.3.3. Polarization-resolved SHG

Polarization-resolved SHG enables the derivation of geometric information on the investigated interfaces. First of all, the $\chi^{(2)}$ tensor reflects the (electronic) geometry of the system and by varying the polarization of the probe beam and by reading out the polarization of the SHG signal, the tensor elements are systematically accessible [6]. Secondly, polarization-resolved SHG is applicable to investigate the smoothness of interfaces [33, 34]. Choosing the coordinate system such that the surface defines the xy-plain and the surface normal accordingly points in the z-direction, the p- and the s-polarized probe beam are of the form:

$$\mathbf{E}_{\mathrm{s}} = E_0 \begin{pmatrix} 0 \\ 1 \\ 0 \end{pmatrix}, \qquad \mathbf{E}_{\mathrm{p}} = \frac{E_0}{\sqrt{2}} \begin{pmatrix} 1 \\ 0 \\ 1 \end{pmatrix}. \tag{2.15}$$

With $P_i^{(2)} = \epsilon_0 \sum_{jk} \chi_{ijk}^{(2)} E_j E_K$ the corresponding material responses become:

$$\begin{aligned} P_i^{(2)}(\mathbf{E}_{\mathrm{s}}) &= \epsilon_0 E_0 \chi_{iyy}^{(2)} \\ P_i^{(2)}(\mathbf{E}_{\mathrm{p}}) &= \epsilon_0 \frac{E_0}{2} \cdot [\chi_{ixx}^{(2)} + \chi_{ixz}^{(2)} + \chi_{izx}^{(2)} + \chi_{izz}^{(2)}]. \end{aligned} \tag{2.16}$$

The p- and s-polarized detection settings result in measured SHG intensities:

$$\begin{aligned} I_{\mathrm{s}}^{SHG}(\mathbf{E}_{\mathrm{s}}) &\propto |\chi_{yyy}^{(2)}|^2 \\ I_{\mathrm{p}}^{SHG}(\mathbf{E}_{\mathrm{s}}) &\propto |\chi_{xyy}^{(2)} + \chi_{zyy}^{(2)}|^2 \\ I_{\mathrm{s}}^{SHG}(\mathbf{E}_{\mathrm{p}}) &\propto |\chi_{yxx}^{(2)} + \chi_{yxz}^{(2)} + \chi_{yzx}^{(2)} + \chi_{yzz}^{(2)}|^2 \\ I_{\mathrm{p}}^{SHG}(\mathbf{E}_{\mathrm{p}}) &\propto |\chi_{xxx}^{(2)} + \chi_{xxz}^{(2)} + \chi_{xzx}^{(2)} + \chi_{xzz}^{(2)} + \chi_{zxx}^{(2)} + \chi_{zxz}^{(2)} + \chi_{zzx}^{(2)} + \chi_{zzz}^{(2)}|^2. \end{aligned} \tag{2.17}$$

For systems inhering a macroscopic preferential molecular alignment as for example in Langmuir films, it has been shown that it is possible to identify these

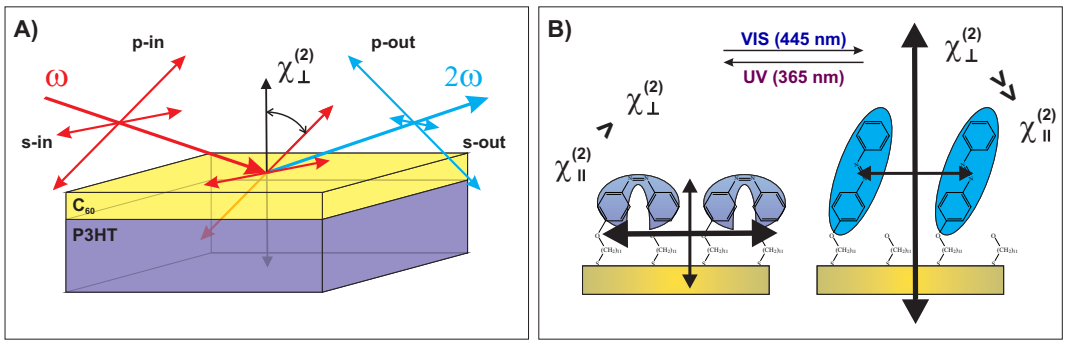

Figure 2.13. (A) For samples which are homogeneous parallel to the interface as the layered C_{60}/P3HT (chapter four), the SHG signal arising from an s-polarized probe beam vanishes due to symmetry reasons (for simplicity, only the non-linear response of one interface is shown). (B) Switching from the upstanding *trans*-azobenzene, to the bent *cis*-form reduces the NLO response perpendicular to the interface due to the rearrangement of the π-electron system (chapter three).

second order non-linear susceptibilities with molecular first hyperpolarizabilities and accordingly derive the molecular orientation at the surface [3, 26]. For the photochromic interfaces investigated in the framework of this thesis an average distribution of molecules within the xy-plain has to be assumed. As demonstrated in section 3.2, density functional theory as well as correlated wavefunction methods are applicable to calculate average molecular hyperpolarizabilities and derive information on the alignment of the chromophoric units. As depicted in figure 2.13B a preferential orientation of molecules with highly electronically conjugated π-systems relative to the interface can directly be derived. This is done by comparing $I_{\mathrm{p}}^{SHG}(\mathbf{E}_{\mathrm{p}})$ to the SHG intensities measured for the other polarization combinations as solely in this polarization setting the dominating $\chi_{zzz}^{(2)}$ tensor-element is accessible, if the chromophores are aligned parallel to the surface normal.

The investigation of the smoothness of interfaces is of particular importance for systems as the C_{60}/P3HT heterojunction investigated in the framework of this thesis, as the successful preparation of a well-defined interface *via* spin coating and vacuum evaporation is demanding for verification. As illustrated in figure 2.13A, an s-polarized electric field vector possesses no component perpendicular to the surface and should therefore be 'unaware' of the presence of an ideally smooth interface between homogeneous layers. However, diffusion of molecules of one layer across the interface into the adjacent layer results in the formation of undefined interfacial clusters and domains [126, 127]. This potentially interferes with the unambiguous interpretation of the measured TR-SHG data due to recombination associated with interrupted percolation

pathways and cross-currents of electrons and holes [132]. Layered systems should therefore generally be examined for dynamics parallel to the interface.

2.3.4. Spectroscopic SHG

Two principal possibilities to conduct spectroscopic SHG measurements exist. First, the probe beam wavelength can be tuned. When either the fundamental or the SHG wavelength match an electronic transition, the signal gets resonantly enhanced [5,6]. Alternatively, the pump beam wavelength can be varied to obtain excited state dynamics as a function of the excitation wavelength. The latter possibility is applied for the time-resolved SHG experiments conducted in the framework of this thesis. As illustrated in figure 2.14 for a semiconducting (organic) sample, increasing the excitation energy *via* variation of the pump photon wavelength, enables the population of additional electronic bands and accordingly opens up additional de-excitation pathways. In the schematic example the corresponding SHG signal amplitude following the initial excitation switches from mono- to bi-exponential as the S_2 band is accessed.

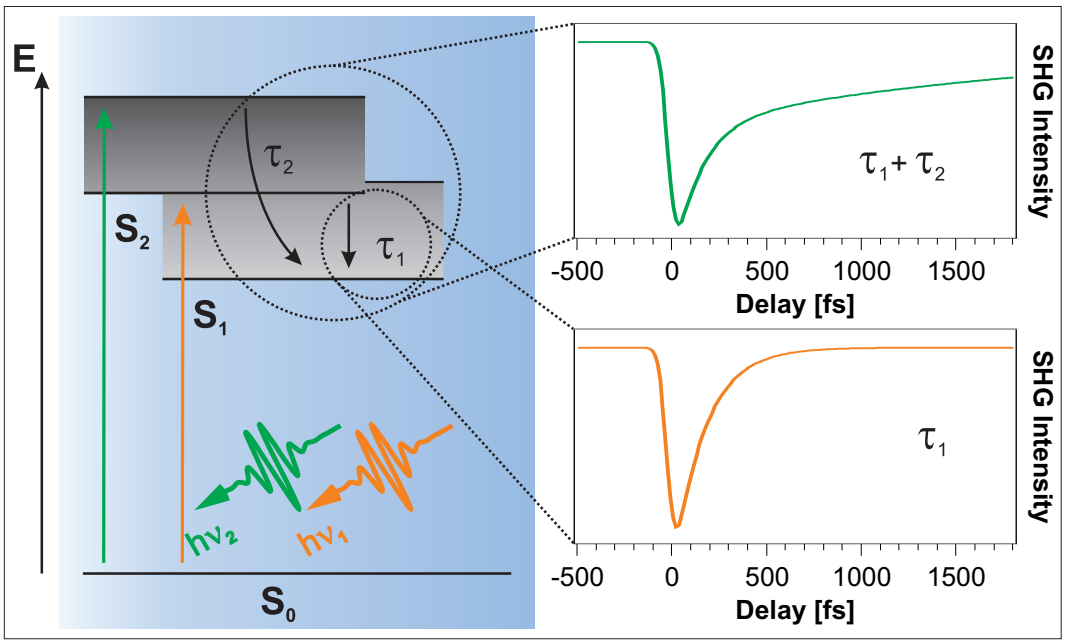

Figure 2.14. Schematic illustration of spectroscopic SHG measurements conducted by varying the pump beam wavelength. For higher excitation energies, the S_2 band of the (organic) semiconductor is accessed and the TR-SHG intensity subsequent to the initial excitation switches from mono- to bi-exponential.

Chapter 3

The Non-Linear Optical Response of Photochromic Interfaces

The topic of the present chapter is the investigation of photochromic interfaces by means of the SHG setup developed and realized in the framework of this thesis. It is demonstrated that the switching state of a fulgimide- (section 3.2) and azobenzene-functionalized (section 3.3) self-assembled monolayers can be read out *via* the non-linear optical contrast between the respective photostationary states. Furthermore, it is shown that the efficiency of the conversion processes is derivable in terms of the respective cross-sections and that information on the interfacial molecular alignments is accessible in polarization-resolved measurements. As demonstrated for the fulgimide SAM, a more detailed understanding of the NLO properties of the photochromic interface can be obtained in conjunction with theoretical system modeling. In addition, it is shown for the azobenzene SAMs that the NLO contrast correlates with the chromophore packing density. This chapter begins with an introduction (section 3.1) regarding the photochromism of fulgimides and azobenzenes, the surface functionalization based on the attachment of these photochromic molecules *via* SAMs and the preparation of the investigated samples.

3.1. Introduction: Photochromic Molecules and Interfaces

Photochromism is defined as the reversible photoinduced conversion between two molecular states which possess different absorption spectra [168]. Among the most prominent examples are the ring-opening/ring-closure reactions of molecules like fulgimides [80, 169, 170] and fulgides [171–173], diarylethenes [48, 52, 174] or spiropyrans [66, 92, 175] and the conformational isomerization of azobenzene [99, 160, 176] and its derivatives [86, 93, 177]. Innovative examples of possible technological implementations for each of these classes

of molecules exist. While the electrocyclization of the former group is frequently associated with a change in electronic properties as for instance the demonstrated switching of the conductance through diarylethenes [52, 174], applications of the latter class often exploit the geometric rearrangements accompanying the isomerization of functionalized azobenzenes. For instance to switch the cell adhesion properties of surfaces [178, 179] or the wettability of Langmuir-Blodgett films [83]. However, as demonstrated in this chapter for the investigated fulgimide and azobenzene, changes in the degree of electronic conjugation and the orientation of the π-electron system can be expected to result in substantial NLO contrasts for each of these photochromic molecules and might hence lead to possible applications in future photonic and optoelectronic devices [68–70]. Three-dimensional optical data storage devices [48, 58], all-optical logic signal processing units [61, 180] or the utilization of spiropyran/merocyanine as cation sensors read out by the difference in the second order NLO susceptibility [71, 72] constitute only a few intriguing examples.

3.1.1. The Photochromism of Fulgimides

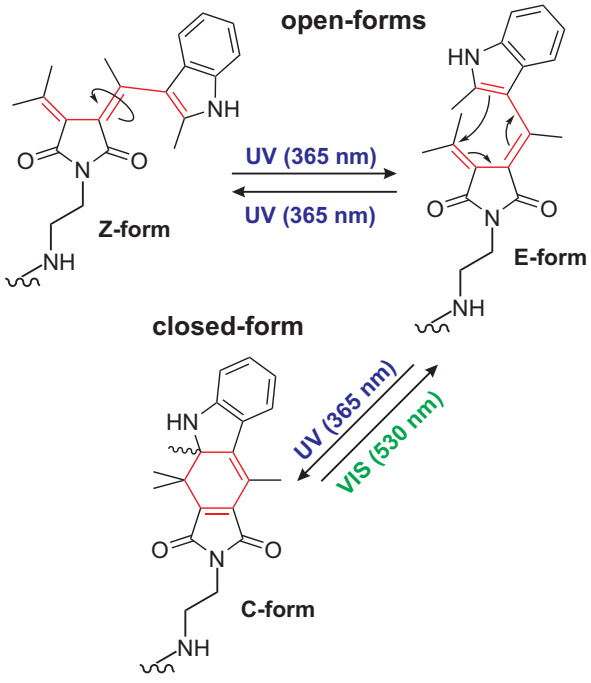

Figure 3.1. Photochromism of the investigated fulgimide. The ring-closure reaction is driven by UV light illumination at 365 nm. The hexatriene/cyclohexadien moieties between which the electrocyclization occurs according to the Woodward–Hoffmann rules [181] are indicated in red. A *trans* $\leftrightarrow$ *cis* isomerization is also operative at this wavelength. Visible light illumination at 530 nm induces the ring-opening reaction. A Z $\rightarrow$ C ring-closure is not operative due to the larger distance between the indole and the methylene group.

The first reported synthesis of a fulgimide dates back to 1957 [169]. Fulgimides are the imide derivatives of fulgides [171]. These offer the possibility of functionalization of the imide nitrogen for example for peptide- and protein-ancho-

ring [163] or as demonstrated here for the attachment to linker-groups in a SAM. Furthermore, the increased resistance to hydrolysis of the fulgimide imide ring in comparison to the fulgide anhydride is considered an advantage regarding possible applications [182, 183].

However, both fulgides and fulgimides are considered suitable for commercial applications due to: (1) complete thermal stability at ambient temperatures, (2) high conversion on irradiation (i.e., high respective product/educt ratios), (3) high quantum efficiencies for forward and reverse reactions, (4) good fatigue resistance and (5) straightforward synthetic methods suitable for large-scale synthesis [170]. Moreover, the ring-opening and ring-closure reactions of indolyl-fulgides and -fulgimides in solution, the latter being highly similar in electronic structure to the indolyl-fulgimides investigated within the framework of this thesis, were found to take place on timescales on the order of a picosecond, i.e., ultrafast and without formation of meta-stable intermediates [172, 173, 184, 185]. The latter constitutes an important prerequisite for the applicability of the Woodward–Hoffmann rules [181]. According to these, the photochemical process in the fulgide and fulgimide ring-closure reaction is the conrotatory electrocyclization of the central hexatriene moiety, as indicated in figure 3.1 for the here investigated fulgimide. As hexatriene possesses three carbon double bonds, the conrotatory transition from the initial to the final molecular orbital configuration is optically symmetry allowed and the ring-closure reaction can hence be photoinduced *via* UV light illumination [186, 187]. The result is an almost planar four-ring conjugated π-electron system (*vide infra*). The absorbance of the colored (C) fulgimide is therefore shifted to longer wavelengths and the back-reaction to the open *trans*-fulgimide (E) is accordingly inducible by means of visible light illumination [186, 187]. Aside from the electrocyclization, an additional *trans* $\leftrightarrow$ *cis* isomerization is operative upon UV light illumination, as also shown in figure 3.1. As the conformational isomerization towards the *cis*-form (Z) competes with the E $\rightarrow$ C coloration and Z $\rightarrow$ C ring-closure is not operative due to the large distance between the indole and the methylene groups, the Z $\leftrightarrow$ E isomerization is generally considered an energy-wasting, undesired process [188]. It has been shown that quantum yields and final isomer ratios of the processes driven by UV light illumination can be tuned by the choice of the substituents not directly involved in the electrocyclization [189–191]. The rations between the three forms of the here investigated fulgimide shown in figure 3.1 in benzoic solution were determined to be (Z/E/C) = 6/15/79 and 6/94/0 for UV- and the visible-PSS, respectively [80].

The applicability of these chromophores has been demonstrated for example for re-writable holographic films [192] or for switchable energy transfer channels constructed of donor-fulgide-acceptor triads [193]. Regarding possible applications in optical data storage devices, it has been shown that the

fulgide switching state can be read out by means of IR laser diodes, i.e., without triggering the ring-opening/ring-closure reaction [194]. Another promising example is the covalent attachment of a fulgimide to an oxazine. The latter exhibits pronounced fluorescence upon excitation with red light (650 nm) solely when the fulgimide group has been switched to the open state with green light (530 nm) in advance [195]. En route towards molecular optoelectronics, examples as a molecular transistor optically gated *via* the switching state of a fulgimide are promising [180]. Intriguingly, also the applicability of a fulgimide–porphyrin–dithienylethene triad as an all-optical logic signal processing unit with four individually addressable switching states has been demonstrated [61].

3.1.2. The Photochromism of Azobenzenes

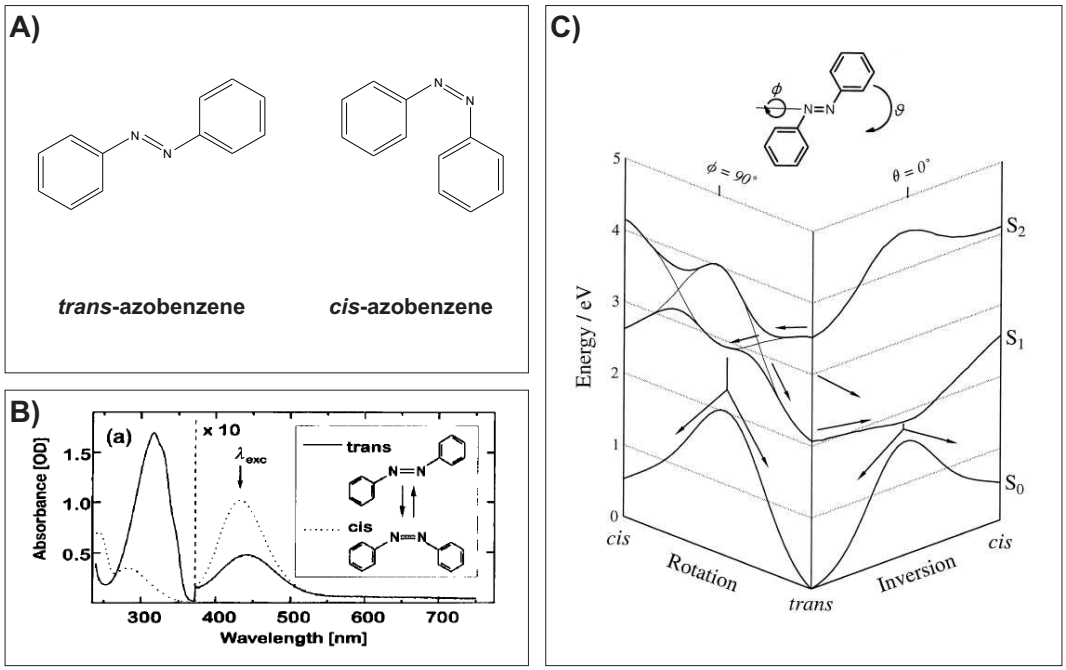

Figure 3.2. (A) Structural formulas of *trans*- and *cis*-azobenzene. (B) Ground state UV/visible absorption spectra of both azobenzene isomers in ethanol reproduced from ref. [160]. (C) Scheme of the potential energy curves of the ground state S_0 and first and the second excited state S_1 and S_2 of azobenzene, respectively. The arrows indicate possible relaxation pathways following the optically dipole allowed $\pi \rightarrow \pi^*$ excitation between ground and second excited state. The *trans* $\leftrightarrow$ *cis* isomerization either follows the out-of-plane rotation around the dihedral C–N=N–C angle (ϕ) or the in-plane inversion around the C–N=N bond angle (Θ). Reproduced from ref. [196].

The first report on the coincidental experimental observation of the existence of the *cis*-form of azobenzene due to the irreproducible solubility of an azobenzene containing solution under exposure to sun light dates back to 1937 [176]. The prototypal molecular switch has been subject to a vast amount of studies ever since, due to reversibility and speed of the photoswitching process and the simplicity of chemical modification and incorporation into complex molecular structures [197].

Azobenzene exhibits the two isomeric forms shown in figure 3.2A. In solution, the *trans* $\rightarrow$ *cis* isomerization is achieved by illumination with UV light while the reverse process, the *cis* $\rightarrow$ *trans* conformational change is induced by blue light as indicated by the different absorption spectra of both forms shown in figure 3.2B. As both absorption spectra overlap to a certain degree, illumination of an azobenzene containing solution results in photostationary states containing both isomers. For example for the azobenzene derivative 6-(4-trifluoromethyl-4'-azobenzeneoxy)-hexane-1-thiol (synthesized for use in self-assembled monolayers) solved in ethanol, photostationary states containing 10-15 % and 70-75 % *trans*-isomers were found under illumination with UV and visible light, respectively [161]. Although the ground state energy of the *cis*-isomer is 0.6 eV higher than the one of the *trans*-form, the thermal *cis* $\rightarrow$ *trans* back reaction is still hampered by an activation barrier on the order of 1.0 eV [98]. Accordingly, the half-life of the meta-stable state is on the order of hundreds of hours at room temperature, depending on the solvent [198].

The two feasible realizations of the isomerization concerning the nuclei movement on the picosecond timescale are the out-of-plane rotation around the C–N=N–C dihedral angle and the in-plane inversion around one of the C–N=N bond angles, as indicated by the potential energy curves of azobenzene in figure 3.2C. Out of the ground state S_0, the n $\rightarrow \pi^*$ excitation corresponding to the transition to the first excited state S_1 is optically dipole forbidden [199] in contrast to the $\pi \rightarrow \pi^*$ transition to the S_2 state. Which of the two pathways dominates, is controversially discussed [200] but present consensus points towards rotation [201] for both the *trans* $\rightarrow$ *cis* [202] and the *cis* $\rightarrow$ *trans* [203] isomerization.

3.1.3. Chromophore Immobilization and Self-Assembled Monolayers

As already mentioned in the introduction, a critical step on the route towards technical application of molecular switches, for example exploiting their differences in (non-linear) optical properties for three-dimensional optical data storage devices [48] or the observed conductivity switching for utilization within electric circuits [52], is to find an immobilization strategy upon which the

functionality is preserved.

Primary of research interest is the investigation of isomerization processes in almost ideally defined systems prepared by vacuum evaporation of the functional molecules onto solid surfaces. In this regard, especially noble metals are thoroughly investigated due to their chemical inertness which was widely considered to preserve the switching ability.

However, in most reported cases the photochromism is quenched upon physisorption. A light-induced isomerization has for example never been observed for azobenzene adsorbed in its thermally more favorable *trans*-form [201, 204, 205] on Au(111) [92]. Even a switching within an STM junction has only been achieved on the Au(111) surface [206, 207], but not on Ag(111) [208, 209]. Another example is trimethyl-6-nitrospiropyran for which the thermal stability is reversed upon adsorption onto the Au(111) surface due to the zwitterionic character of the open merocyanine form which leads to a strong ionic binding to the gold surface [175]. As a result, the ring-opening which can be induced by electron attachment in the STM junction or thermally, is irreversible whereas the photochromism is quenched completely [85].

For these systems two reasons for a suppressed photochromism are generally considered. One is a steric hindrance of conformational changes in the switching process due to the presence of the surface. The other is the existence of surface-derived ultrafast de-excitation channels [86] competing with the nuclei movement which is for the free molecule know to take place on a picosecond timescale [98, 210]. An alternative explanation is the recently proposed 'loss of bi-stability' upon physisorption, i.e., a significant reduction of the thermal barrier for one of the isomers found for *cis*-azobenzene adsorbed on Au(111) and Ag(111), respectively [201].

These findings imply the necessity of a precise fine-tuning of the adsorbate-substrate interaction [87] for which different strategies are known [45]. One prominent example is 3,3',5,5'-tetra-*tert*-butyl-azobenzene (TBA) which is the result of the attempt to restore the surface quenched photochromism by adding bulky spacer groups to reach an electronic and geometric decoupling between the substrate and the photochromic unit of the adsorbate molecule. TBA was found to be switchable upon illumination and with the STM tip on the Au(111) surface [74, 93, 211]. However, no *trans* $\leftrightarrow$ *cis* isomerization has been reported for TBA/Ag(111) [212] and for the Cu(111) and Au(100) surfaces [207]. Ironically, the decoupling strategy leads to a stronger binding to the substrate with respect to azobenzene [213] and the partial success rather results from the coincidental restoration of the photochromism of TBA/Au(111) than from a preservation. The photoisomerization of TBA/Au(111) is not induced by the intramolecular $n \rightarrow \pi^*$ or $\pi \rightarrow \pi^*$ transition as in the free molecule [89] but by the creation of a positive ion resonance (PIR), instead. A PIR is a substrate-mediated excitation mechanism in which a photohole relaxes to

the gold *d*-band edge located around -2.0 eV below the Fermi-level (E_F) followed by hole attachment to the highest occupied molecular orbital (HOMO) of TBA centered around -1.88 eV [94]. On the one hand, the inactivity of this substrate-mediated isomerization mechanism for azobenzene/Au(111), where the energetic overlap between the HOMO of the molecule and the gold *d*-band is only reduced by 110 meV [92], pronounces the necessity for a precisely balanced adsorbate–substrate interaction. On the other hand, substrate-mediated alternative photoisomerization pathways as *via* the discussed creation of a PIR or also a negative ion resonance (NIR) [214], offer additional design strategies for the adsorbate/substrate system as an entity.

Another example for a precisely tuned adsorbate–substrate interaction is 4-anilino-4'-nitroazobenzene/Cu(111) which has been reported to be photoswitchable, achieved *via* the appropriate push-pull balance between chemically attractive end-groups and a van der Waals interacting aromatic backbone [86]. Finally, it was demonstrated that an ultrathin passivating NaCl layer neutralizes the influence of a Cu(111) substrate on the molecular orbitals of adsorbed pentacene molecules [215]. The same strategy also restores the hydrogen tautomerization of naphthalocyanine on Cu(111) which is in contrast quenched on bare Cu(100) [216]. An NaCl passivation has also been applied to restore the functionality of azobenzene derivatives on the Ag(111) surface which led to reversible isomerization in the STM junction *via* inelastic electron tunneling [208] and the *trans* $\rightarrow$ *cis* but not the back reaction upon illumination [209].

While a detailed understanding of the fundamental isomerization processes in the aforementioned systems is of particular importance for an actual future development of devices based on molecular switches [217], numerous more application-oriented approaches to incorporate the photochromic unit into chemical environments exist which offer different advantages and disadvantages as outline hereinafter.

Polymers containing stereoisomeric chromophores like for example azobenzene undergo mechanic deformations upon isomerization rendering them inappropriate for optical data storage due to the relatively low isomerization speed [81]. However, the inducible macroscopic changes enable surface pattern writing which is for example utilized to photofabricate surface relief gratings [82]. Also, the photoswitchable wettability [83] or magnetization [84] of azobenzenes-functionalized Langmuir-Blodgett-films was demonstrated, albeit in both cases accompanied by a certain fatigue in reversibility.

Interface functionalization *via* attachment of photochromic molecules containing SAMs is the approach chosen for both photoswitchable surfaces investigated within the framework of the present thesis. SAMs are ordered molecular assemblies formed by the adsorption of an active surfactant on a solid surface [218]. One of the major advantages of this approach is that the adsorbate–substrate as well as the adsorbate–adsorbate interactions can

be tuned *via* the length of the anchoring groups and by incorporating spacers [80,100,101,104,162], respectively. Different strategies like the self-assembly of rather large triazatriangulenium (TATA) ions [96,167] or adamantane cores [95] onto which the functional unit is directly attached, exist. However, most frequently functionalized long-chain hydrocarbons are immobilized usually either *via* sulfur bonding to a gold substrate [99, 219, 220] or grafting directly onto a silicon surface [79, 221, 222].

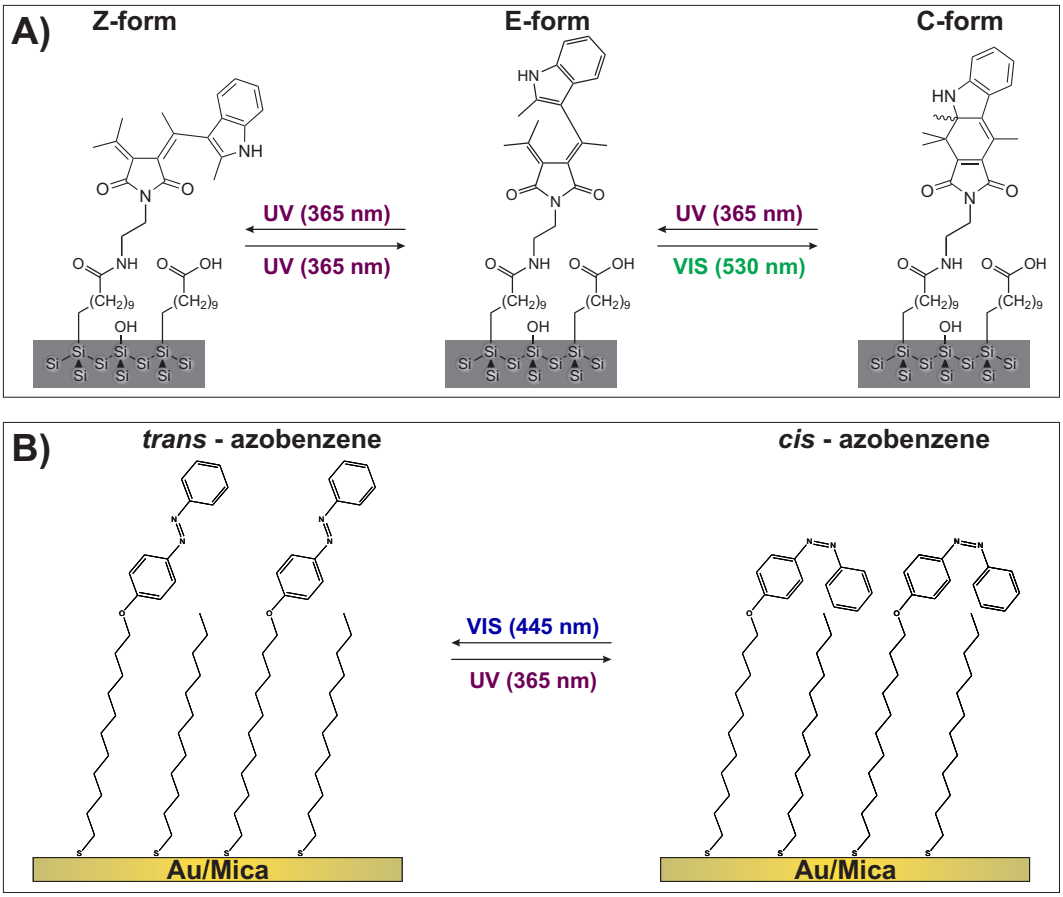

Figure 3.3. (A) The on-chip synthesis of the photochromic fulgimide SAM on Si(111) results in a chromophore packing density of approximately 25 % with respect to the available silicon sites. Residual positions are either OH-terminated or covered by carboxy-terminated alkyl chains. (B) A photochromic azobenzene SAM/gold interface is obtained by: (a) decoupling chromophore and substrate using undecanethiol chains and (b) intermixing dodecanethiol spacers to reduce the chromophore packing density. Photoreactions operative at the respective interfaces are indicated in both panels.

The packing density of these self-assembled monolayers is the crucial pa-

rameter regarding the photoisomerization ability. Steric hindrance [104], but also excitonic coupling, i.e., an ultrafast excitation dissipation among adjacent chromophores due to π-stacking as found for azobenzene–alkanethiol–SAMs on gold [102,103,105] are possible reasons for a quenched photochromism. Besides the above mentioned platform strategies, steric hindrance can be avoided by: (a) using sufficiently wide spacers [165], (b) an on-surface functionalization in which only a fraction of the available surface positions is occupied [80, 164] or (c) by intermixing unmodified (alkyl) chains (i.e., which do not carry a chromophore) [100, 101, 104]. A combination of differently modified chromophores regarding electronic configuration influencing attachments to avoid excitonic coupling has also been proposed [177]. Strategy (b) is pursued for the photochromic fulgimides discussed in section 3.2. The azobenzene-functionalized SAMs which are the topic of section 3.3 are attached to the gold substrate from an immersion which additionally contains a variable fraction of unmodified alkyl chains, according to strategy (c).

Switching the fulgimide-functionalized surface is expected to result in a pronounced change in the SHG signal amplitude as the degree of the electronic conjugation is significantly increased in the reaction towards the closed form, for which the delocalization of the π-system extends over four conjugated rings. As the hyperpolarizability-vector [97] of the closed fulgimide incorporated in the SAM is expected to point almost perpendicular to the surface [80], a pronounced reduction in the SHG signal amplitude measured in the direction of the surface normal is expected upon the ring-opening reaction. In contrast, for the azobenzene SAMs the expected contrast arises from the 'geometric' reorientation of the π-system and according reduction of the electronic conjugation perpendicular to the interface, when the photochromic units are switched from the *trans*-form, which is explicitly measured or implicitly expected to be oriented upright for various alkanethiols [99–104], to the bent *cis*-azobenzene.

3.1.4. Preparation of the Fulgimide and Azobenzene SAMs

The fulgimide samples were prepared by Andreas Hebert in the group of Prof. Karola Rück-Braun at the Institut für Chemie at the Technische Universität Berlin. The Si(111) surface was cleaned with piranha solution (H_2O_2/H_2SO_4, 1/3 v/v) for 30 minutes at 100°C, rinsed with ultra pure water and etched with 40 % ammoniafluoride solution for 15 minutes, to obtain a hydrogen-terminated silicon surface. Afterwards, the cleaned and dried hydrogen-terminated silicon surface was thermally reacted with pure methyl undec-10-enoate for 2 hours at 160°C to establish an ester-terminated monolayer. After cleavage of the ester head group by means of hydrochloric acid (5.5 M, 3 hours, 40°C) an carboxy-terminated monolayer was achieved. The photoswitch is immobilized

by immersing the carboxy-terminated surface in a solution containing a 85:15 mixture of (E/Z)-fulgimides (5 mM), HCTU (2-c6-chloro-1H-benzotriazole-1-yl)-1,1,3,3-tetramethylaminium hexafluorophosphate) as a coupling agent (10 mM) and diisopropylethylamin (10 mM) in acetonitrile for 2 hours. Subsequently, the samples were rinsed with acetonitrile and dichlormethane, blown dry, and stored under argon. This on-chip functionalization of the Si(111) surface results in a well-defined organic/inorganic hybrid system as schematically depicted in figure 3.3A. The fulgimide photoswitch coverage is approximately 25 % of the initially H-terminated Si(111) sites. The residual positions are either OH-terminated or covered with the carboxy-terminated alkyl chains. Detailed information are given in ref. [80].

The here investigated azobenzene samples were prepared by Thomas Moldt and Daniel Brete in the group of Prof. Martin Weinelt at the Fachbereich Physik at the Freie Universität Berlin. 300 nm thick annealed gold films on mica were immersed for 20 hours in a methanolic solution containing the desired mixture of 11-(4-(phenyldiazenyl)phenoxy)undecane-1-thiol and dodecane-1-thiol and subsequently rinsed in pure methanol, blown dry and stored under argon. A scheme of the resulting SAM is depicted in figure 3.3B. As the samples were prepared under exclusion of UV light (yellow-light conditions, cut-off wavelength 500 nm), purely *trans*-functionalized azobenzene SAMs were obtained. The simultaneous preparation of two samples in one immersion enabled the determination of the chromophore coverage by means of x-ray photoelectron spectroscopy (XPS) measurements on the 'twin-sample' carried out by Daniel Przyrembel in the group of Prof. Martin Weinelt, Freie Universität Berlin. By referencing the respective N1s peak areas to the ones of a densely packed sample, the chromophore packing density can be estimated with an accuracy below ± 5 %. Detailed information will be given in ref. [162].

All measurements on the photochromic interface are conducted using a 800 nm probe beam. This wavelength is not in overlap with neither absorption band [80, 160]. The probe beam powers are kept below 40 mW for which no beam damage is observed within time windows corresponding to the exposure times during the measurements for neither SAM. Experiments are conducted under protective gas atmosphere (nitrogen, purity '5.0') except for certain measurements on the azobenzene SAMs as outlined in section 3.3.5.

3.2. Reversible Photoswitching of a Fulgimide-Functionalized Self-Assembled Monolayer

Incorporating photochromic molecules into organic/inorganic hybrid materials may lead to photoresponsive systems. In such systems the second order non-linear properties can be controlled *via* external stimulation with light at an appropriate wavelength. By creating photochromic molecular switches containing self-assembled monolayers on Si(111), efficient reversible switching is demonstrated which is accompanied by a pronounced modulation of the non-linear optical response of the system.

The concept of coupling photochromic Si interfaces and NLO properties enables to generate switchable second order NLO materials [62, 223] with potential for application in emerging optoelectronic and photonic technologies [63, 68, 69]. Two-photon writing in (three-dimensional) optical data storage [58, 59, 195] and chemical sensors, read out by their non-linear optical response [71, 72] are only two obvious examples. The most striking advantage of such systems derives from symmetry considerations [6]. The second order NLO response of a sample is inherently restricted to its symmetry-breaking interface [5]. Accordingly, no bulk contribution exists which results in a very high NLO signal contrast even for single functional layers [3, 7] and buried interfaces [14, 28]. As a consequence, truly two-dimensional layered functional units are realizable by anchoring and aligning molecular switches at a planar solid surface.

A well-defined organic/inorganic hybrid system, a flat Si(111) surface functionalized with a self-assembled monolayer containing a fulgimide moiety is chosen. The approach of an on-chip functionalization of H-terminated Si(111) is known to result in high-quality, densely packed SAMs for which most importantly the fulgimide photochromic properties [170, 188] are preserved [80, 164].

The intrinsic interface sensitivity of SHG makes it an ideal probe to demonstrate that at ambient conditions a photoinduced switching of the SAM/Si(111) hybrid system between two thermally stable photostationary states is indeed achieved and accompanied by a reversible and pronounced modulation of the NLO response (section 3.2.1). Regarding possible future applications, the also observed well-defined alignment of the chromophores (section 3.2.2) and the according contrast in the molecular hyperpolarizabilities perpendicular to the surface (section 3.2.3) as well as the high efficiencies of the ring-opening/ring-closure reactions in terms of large switching cross-sections (section 3.2.4) are equally important.

3.2.1. Non-Linear Optical Contrast, Reversibility and Thermal Stability

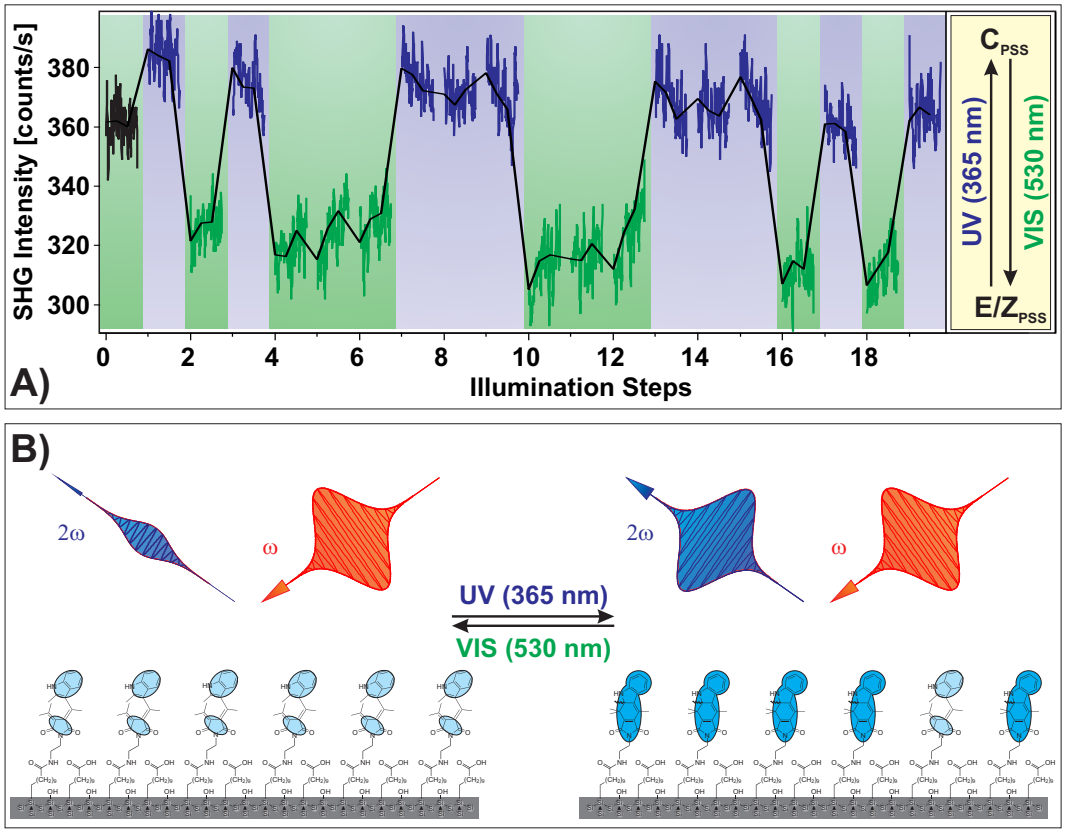

Figure 3.4. Reversible photoswitching of the NLO response of the fulgimide SAM. (A) The SHG data labeled in purple and green denote measurements conducted subsequent to UV (365 nm, photon dose $n_{\mathrm{UV}} = 2.0 \cdot 10^{19}$ cm^{-2}) and visible (530 nm, $n_{\mathrm{vis}} = 1.6 \cdot 10^{19}$ cm^{-2}) light illumination, respectively. The black curve represents the initial state prior to illumination. The pronounced NLO contrast results in SHG signal amplitude changes of 17 ± 6 % and is attributed to the ring-opening/ring-closure reactions. (B) Illustration of the correlation between the NLO contrast measured in the SHG experiment and the rearrangement of the π-electron system in the electrocyclization.

Figure 3.4 shows the SHG signal amplitude as a function of the illumination steps. A large second order NLO contrast is observed when the sample is illuminated with UV light at a wavelength of 365 nm. The signal amplitude change is reversible by exposing the sample to visible light at 530 nm wavelength. The average signal contrast between the two photostationary states is determined to be 17 ± 6 %. It is known, that solutions containing pho-

tochromic fulgides and fulgimides get enriched with the colored C-form upon exposure to UV light and that the accordingly emerging pronounced absorption band of the C-form can be utilized to trigger the reverse ring-opening reaction by means of visible light illumination [170, 182, 186–188, 195, 224]. In high performance liquid chromatography (HPLC) measurements, the Z/E/C-ratios of the here investigated fulgimide solved in benzene were determined to be 15/85/0 prior to illumination, 6/15/79 in the UV-PSS (referred to as C-PSS) and 6/94/0 for the visible-PSS (referred to as E/Z-PSS), respectively [80]. Furthermore, the calculated average first hyperpolarizabilities (section 3.2.3), which constitute the molecular equivalent to the second order non-linear susceptibility, are significantly larger for the C-form in comparison to the E- and Z-fulgimides. The observed SHG signal level changes are therefore assigned to the light-induced conversion of the photochromic interface between the two photostationary states.

Interestingly, the initial SHG amplitude is significantly larger than the average E/Z-PSS signal level (figure 3.4, black *vs.* purple curves). This difference at least partially arises from the aforementioned diverging isomer ratios upon synthesis and subsequent to the first two illumination steps. The reason is, that exposure to UV light establishes a PSS between all three forms while visible light solely drives the C $\rightarrow$ E reaction. However, the measured deviation cannot completely be rationalized in terms of the different E/Z-ratios in the initially prepared state and in the E/Z-PSS, respectively. According to the calculated hyperpolarizabilities (section 3.2.3) high SHG signal levels need to be attributed to C-fulgimides which are absent in both states. This allows for two possible interpretations. Either the attempt to avoid UV light exposure of the sample prior to the measurements did only partially succeed as the ring-opening/ring-closure reactions are highly efficient (section 3.2.4). Or the ratios between the isomers at the surface differ from the ones in solution. Fortunately, a third possibility can be excluded. The presence of C-fulgimides which are not participating in the conversion process as found for a similar interface [164] would not result in an SHG amplitude lower than the average C-PSS signal level. In analogy, an increasing number of 'inactive' E- or Z-isomers would result in a successive decrease of the amount of C-fulgimides and accordingly reduce the NLO contrast with each illumination cycle, which is not observed.

The reversibility of the photochromic reaction is tested by alternately illuminating the sample with photon doses of $n_{\mathrm{UV}} = 2.0 \cdot 10^{19}$ cm^{-2} and $n_{\mathrm{vis}} = 1.6 \cdot 10^{19}$ cm^{-2} to trigger the ring-closure and -opening reactions, respectively. These doses are approximately one order of magnitude higher than sufficient to switch the sample between the PSSs in both cases, as quantified in section 3.2.4. No reduction in the NLO contrast is observed within the given accuracy for the 19 conducted illumination steps and no a fatigue in the response of the

photochromic interface, i.e., no sign of laser- or illumination-induced damage, is observed. However, a slight reduction in laser stability resulting in a 1.5 % drop of SHG signal intensity during the measurement is observed and accounted for as outlined in appendix C.

The thermal stability of the photostationary states at room temperature is verified separately, as shown in figure 3.5. In both cases, two illumination steps are conducted and repeated subsequent to an initial measurement (i.e., without prior illumination) after a waiting period of one day. The data are normalized to the respective C-PSS signal levels and compared with respect to the NLO contrasts. Within the given experimental accuracy, the photochromic interface is found to remain in the respective PSSs. Hence, a significant activation barrier exists which avoids thermally activated reverse reactions. This is in accordance with the expectations as fulgimides are considered to be completely thermally stable [170] even at elevated temperatures [225].

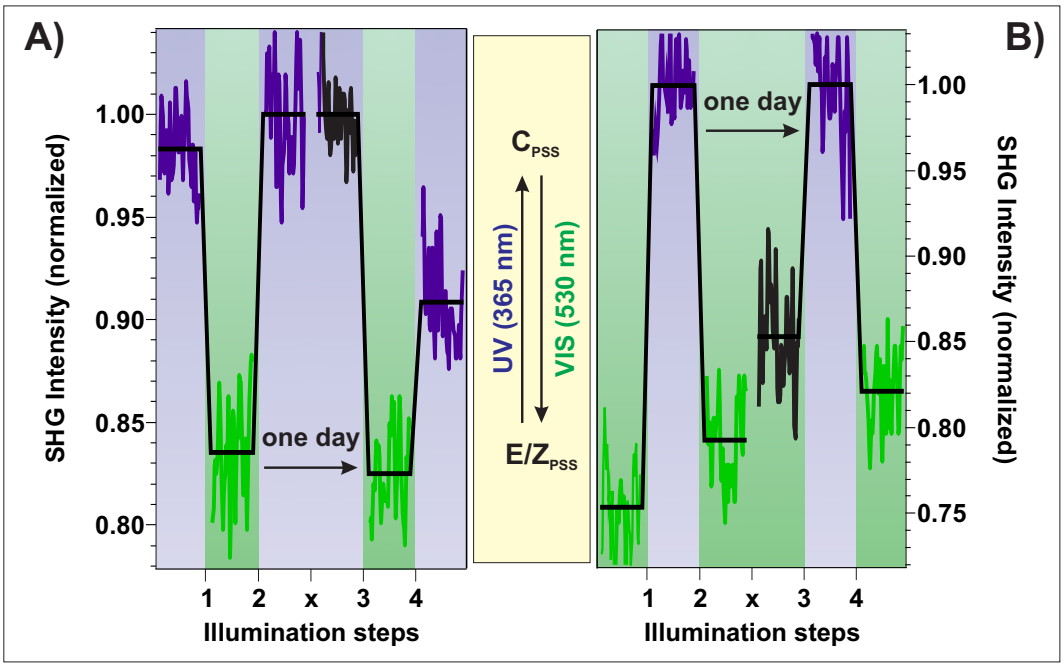

Figure 3.5. The C-PSS (A) and the E/Z-PSS (B) of the fulgimide SAM are thermally stable at room temperature within the given accuracy on a timescale of one day. To account for possible diverging measurement conditions, the data are normalized to the respective C-PSS signal levels prior and subsequent to the waiting period to compare the relative amplitude changes in the switching cycles. Black curves denote measurements without prior illumination. The applied photon doses are $n_{\mathrm{vis}} = 1.6 \cdot 10^{19}$ cm^{-2} (530 nm) and $n_{\mathrm{UV}} = 2.0 \cdot 10^{19}$ cm^{-2} (365 nm), sufficient to reach the respective PSSs.

3.2.2. Interfacial Molecular Alignment

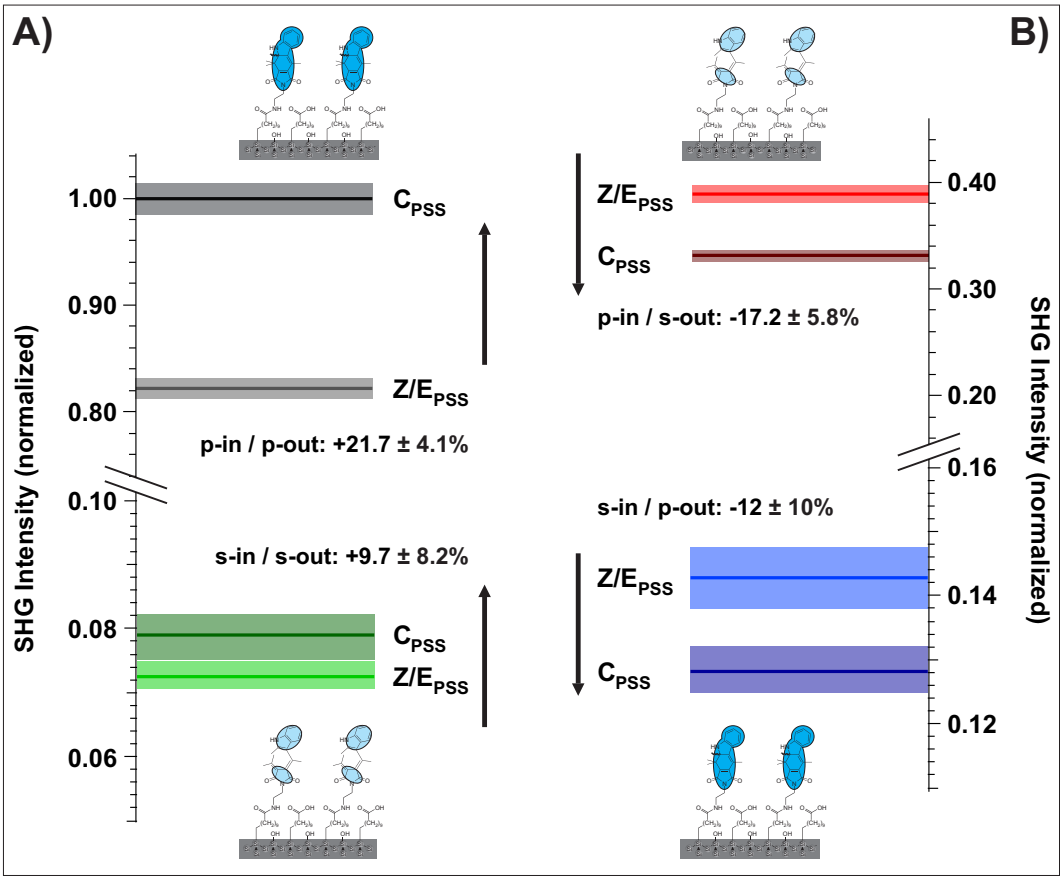

Figure 3.6. Results of the polarization-resolved SHG measurements on the fulgimide SAM for the polarization combinations (A) p-in/p-out (black) and s-in/s-out (green) and (B) p-in/s-out (red) and s-in/p-out (blue), where 'in' and 'out' denote the polarizations of the 800 nm probe and the 400 nm SHG signal beam, respectively. Darker colors in both panels represent the C-PSS. Colored areas indicate the experimental uncertainty. Data normalized with respect to the most intense component (p-in/p-out, C-PSS) for comparability.

In order to investigate the molecular alignment of the fulgimide SAMs, polarization-resolved SHG measurements are conducted. Figure 3.6A shows the results of these measurements for the in- and outbound beams both p-polarized (black) and both s-polarized (green). Figure 3.6B displays the signals measured for the 'mixed' polarizations p-in/s-out (red) and s-in/p-out (blue), where 'in' and 'out' denote the polarizations of the 800 nm probe beam and the 400 nm SHG signal beam, respectively. The darker colors in both panels depict the data obtained for the C-PSS. SHG signal amplitude changes induced

by switching to the C-PSS are indicated by the black arrows. The signal level increases in the ring-closure reaction when in- and outbound beams are equally polarized (figure 3.6A), while the opposite is observed for mixed polarization settings (figure 3.6B).

Two important observations can be derived from the data displayed in figure 3.6. (1) Considering the relative SHG signal amplitudes measured for the four polarization combinations, the p-in/p-out setting results in the strongest NLO response, followed by the p-in/s-out combination. In contrast to these two, the other two settings result in comparably low signal levels. (2) For the ring-opening reaction the p-in/p-out signal intensity displays the most pronounced relative and absolute change, it decreases by 21.7 ± 4.1 %. In contrast, for the second strongest p-in/s-out combination the signal amplitude increases by 17.2 ± 5.8 % in the ring-opening reaction.

The implications are the following. (1a) According to equation 2.17, the p-in/p-out setting is the only polarization combination in which the diagonal $\chi^{(2)}_{zzz}$ component perpendicular to the surface [6] is probed. The domination of the p-in/p-out combination therefore implies an orientation of the electronic π-system of the C-fulgimide perpendicular to the surface and hence a molecular alignment primarily along the surface normal. (1b) In the p-in/s-out combination, the minor-diagonal tensor elements are accessible which describe a correlation between the non-linear polarizability in the z-direction and along the other axes, respectively. The implication might be a slight tilt of the chromophore with respect to the surface normal. However, further investigations of the molecular alignment are necessary, for example obtainable by combining NEXAFS (near edge x-ray absorption fine structure spectroscopy) measurements and theoretical modeling [102]. (2a) The pronounced decrease in the NLO response upon ring-opening measured in the p-in/p-out combination can be attributed to the reduction in the degree of the electronic conjugation perpendicular to the surface by reducing the extend of the π-system from the four-ring conjugated C-fulgimide to the open structure. (2b) The p-in/s-out polarization combination samples the minor-diagonal $\chi^{(2)}$ tensor elements of the z-axis. A rising signal amplitude measured for this setting upon ring-opening thus implies an increasing non-linear polarizability along the bisecting cone between the surface normal and the interface and might be attributable to a reorientation of the indole moiety from perpendicular to the surface into this direction.

In summary, these findings coincide with the expectations. In the densely packed layer, the C-fulgimide is apparently oriented predominantly parallel to the surface normal. This results in a large non-linear susceptibility perpendicular to the surface arising from the highly conjugated four-ring π-system. Upon ring-opening, this conjugation along the surface normal is interrupted, giving rise to the observed pronounced NLO contrast. However, in comparison to

the more intuitive interpretation of the data on the azobenzene chromophore alignment (section 3.3.2), the comparably complex molecular structure of the investigated fulgimide demands for an additional theoretical modeling, as discussed in the following section.

3.2.3. Theoretical Modeling of the NLO Response

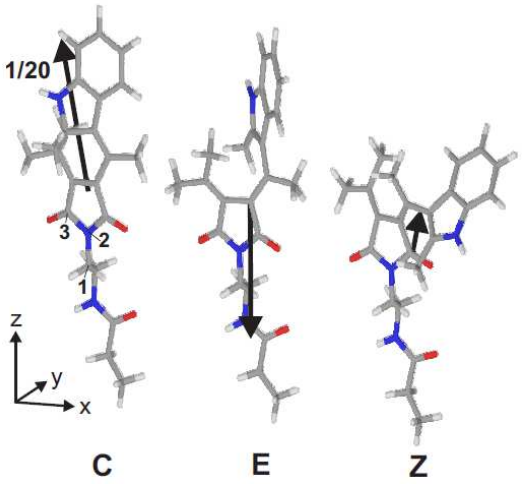

Figure 3.7. Structures of C-, E- and Z-fulgimides optimized at the B3LYP/6-311++G** level of theory. Atoms '1' and '2' span the z-axis, atom '3' defines the xz-plane. Nitrogen, oxygen, carbon and hydrogen atoms are shown in blue, red, gray and light-gray, respectively. Respective hyperpolarizability vectors $\boldsymbol{\beta} = (\beta_x, \beta_y, \beta_z)$ are also shown. $\boldsymbol{\beta}$(C) scaled by a factor of 1/20 with respect to $\boldsymbol{\beta}$(E) and $\boldsymbol{\beta}$(Z). Calculations performed in collaboration with the group of Prof. Saalfrank (Universität Potsdam).

In order to quantify the observations described in the preceding two sections, electronic structure calculations of closed and open fulgimides using density functional theory as well as correlated wavefunction methods are performed by Manuel Utecht in the group of Prof. Peter Saalfrank at the Institut für Chemie at the Universität Potsdam. The resulting components of the first hyperpolarizability $\boldsymbol{\beta}$, which is the molecular equivalent to the second order non-linear susceptibility $\chi^{(2)}$ amplify the understanding of the experimental data as the latter is proportional to the measured SHG signal.

In a first step hybrid density functional theory on the B3LYP/6-311++G** level is utilized to optimize structures for the free closed and open fulgimide molecular models with the anchored alkyl unit (-$(CH_2)_9$-Si) replaced by an ethyl group (-C_2H_5). Distinct minima are found for the closed C- and the open E-form, and several near-degenerate structures for the open Z-form, the latter all with similar geometries and first hyperpolarizabilities. On the applied level of theory, the E-fulgimide is the most stable followed by the Z- (0.01 eV higher) and the C-form (0.15 eV higher). In figure 3.7 the structures of C- and E-fulgimide as well as one of the near degenerate Z-forms are shown. As mentioned above, regarding the electronic structure and accordingly the

hyperpolarizability of the three molecules, the most striking difference between the open and closed structures is the delocalization of the π-electron system. The computed angles between the indole (2,3-benzopyrrole) and imide moiety (2,5-pyrrolidine) planes are 9° for the C-fulgimide, and 33° and 27° for E- and Z-forms, respectively. Hence, the π-electron system of the C-molecule is delocalized over four conjugated rings, while the torsion between the indole and imide planes interrupts this delocalization for the open isomers.

In a second step the dynamical hyperpolarizabilities $\boldsymbol{\beta}(2\omega;\omega,\omega)$ at frequencies $\omega = 2\pi c/\lambda$ corresponding to the excitation wavelength $\lambda = 800$ nm as adopted in the SHG measurements are calculated for the three molecular structures. The dynamic hyperpolarizabilities are determined at the MP2 (Møller-Plesset perturbation theory at second order) level at the B3LYP geometries, according to an established procedure described in reference [226]. Aligning the calculated molecular structures as depicted in figure 3.7, i.e., with the carbon atom '1' and the nitrogen atom '2' spanning the z-axis, results in an angle between the surface normal and the ethyl group of 33°. This is in accordance with the experimentally determined angle of the amide terminated alkyl linker chains with respect to the Si(111) surface normal of $28 \pm 8°$ [80]. The xz-plain is randomly defined by the maleimide 5-ring. As mentioned above, the important parameters are the difference in the averaged overall hyperpolarizability of the open- and closed forms β_0, defined as [97]

$$\beta_0 = (\beta_x^2 + \beta_y^2 + \beta_z^2)^{\frac{1}{2}}, \tag{3.1}$$

$$\beta_i = \beta_{iii} + \frac{1}{3}\sum_{j\neq i}(\beta_{ijj} + \beta_{jij} + \beta_{jji}), \tag{3.2}$$

and the orientation of the respective hyperpolarizability vector $\boldsymbol{\beta} = (\beta_x, \beta_y, \beta_z)$ with respect to the surface normal as depicted in figure 3.7. The calculated tensor elements shown in table 3.1 correspond to the expectations. The averaged hyperpolarizability β_0 is significantly larger for the C-fulgimide compared to the open forms which explains the pronounced NLO contrast observed in the SHG experiments. Furthermore, β_{zzz} is indeed identified as the dominating tensor element in accordance with results derived from the polarization-resolved SHG measurements. It has to be remarked, however, that the calculated differences in the tensor elements between the open- and closed-fulgimide are larger than the experimentally observed contrasts. Whether this discrepancy arises from an unordered alignment of the chromophores resulting in a reduction of the SHG signal contrast or a lowering of the alignment angle with respect to the surface normal of the fulgimide-functionalized SAM in comparison to the one determined for the amide layer [80], is so far unknown. Clarification could result from extending the calculations to a slab of fulgimide SAMs.

	C	E	Z
β_0	42244	1954	627
β_{zzz}	-49352.9	-1874.6	22.4
β_{yyy}	-75.3	-199.8	97.0
β_{xxx}	-57.7	169.2	-477.1
β_{ijk}	C	E	Z
yxx	201.3	45.8	356.3
xyx=xxy	160.1	-84.4	307.4
yyx=yxy	7.3	-47.7	74.5
xyy	32.3	-43.8	77.3
xzx=xxz	16044.5	448.1	341.6
zxx	9333.2	466.2	351.0
yxz=yzx	727.5	-129.1	31.5
xzy=xyz	20.1	28.1	37.8
zyx=zxy	329.1	-87.5	35.1
yzy=yyz	29.9	34.7	41.0
zyy	191.9	-56.5	48.8
zzx=zxz	-11455.9	313.2	227.0
xzz	-8516.9	225.1	222.6
zzy=zyz	3184.3	-750.5	88.9
yzz	5871.6	-937.8	111.3

Table 3.1. Elements of the hyperpolarizability tensor for the investigated fulgimides calculated with Møller-Plesset perturbation theory at second order at the B3LYP/6-311++G** geometries and the averaged overall hyperpolarizability β_0 according to equation 3.1. All values are given in atomic units, where one arbitrary unit corresponds to $8.641 \cdot 10^{-33}$ esu or $3.62 \cdot 10{-}42$ m^4/V. Calculations performed in collaboration with the group of Prof. Saalfrank (Universität Potsdam).

3.2.4. Ring-opening/Ring-closure Cross-Sections

To gain information about the switching efficiency for the photochromic interface, the light-induced ring-closure and -opening reaction pathways of the fulgimide-functionalized SAM on the Si(111) surface are quantified. The effective cross-sections (σ) for both reactions are thereby evaluated by using the change in the SHG signal amplitude as a measure for the switching process, i.e., the observed changes as a function of the respective photon dose are correlated with the number of switched molecules according to equations 2.8 and 2.14. This assignment is based on the implicit assumption that the fraction of surface immobilized molecules in the Z-form is equal in both photostationary states as found in solution [80], and accordingly do not contribute to the SHG signal contrast. The data shown in figure 3.8A and B is obtained by illuminating the sample with photon fluxes of $f_{UV} = 1.0 \cdot 10^{15}$ $s^{-1}cm^{-2}$ (365 nm) and $f_{vis} = 1.9 \cdot 10^{15}$ $s^{-1}cm^{-2}$ (530 nm), respectively. The solid lines represent fits according to a mono-exponential saturation function. From these fits, effective cross-sections of $\sigma_{E\rightarrow C} = 2.3 \pm 0.3 \cdot 10^{-18}cm^2$ for the ring-closure reaction and $\sigma_{C\rightarrow E} = 1.2 \pm 0.3 \cdot 10^{-18}cm^2$ for the ring-opening are derived.

These high cross-sections clearly indicate an efficient electronic decoupling

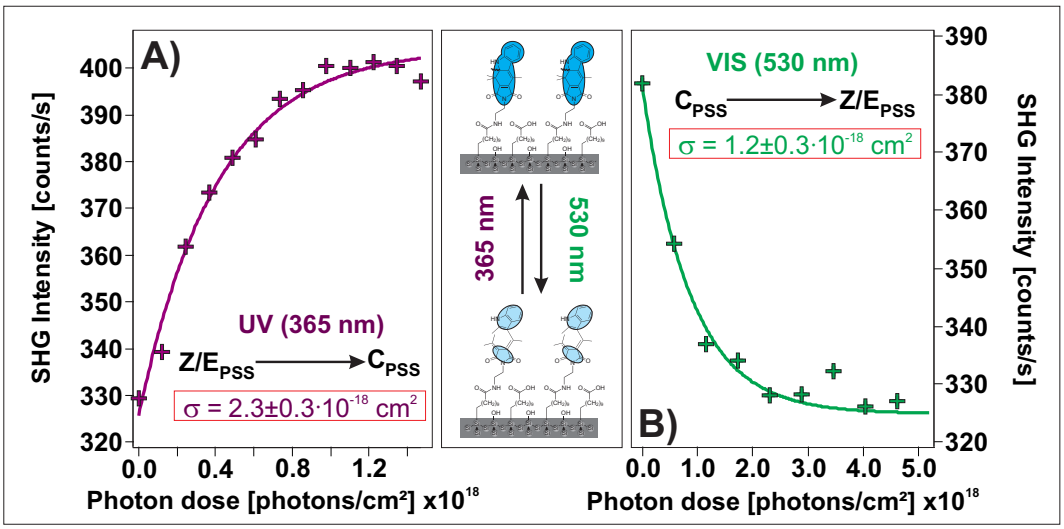

Figure 3.8. SHG signal amplitude as a function of the photon dose. (A) The rising signal level at $\lambda = 365$ nm UV light exposure is attributed to the increasing concentration of closed isomers in the ring-closure reaction $E/Z_{PSS} \rightarrow C_{PSS}$. (B) The decreasing amplitude at $\lambda = 530$ illumination is associated with the ring-opening reaction $C_{PSS} \rightarrow E/Z_{PSS}$. Solid lines in (A) and (B) represent fits using a mono-exponential saturation function, yielding $\sigma_{UV} = 2.3 \pm 0.3 \cdot 10^{-18}$ cm^2 and $\sigma_{vis} = 1.2 \pm 0.3 \cdot 10^{-18}$ cm^2, respectively.

of the molecular switch from the substrate as well as an electronic and steric decoupling within the molecular film. This is particularly evident in contrast to the already mentioned switch TBA physisorbed on a Au(111) metal substrate which possesses an effective cross-section nearly four orders of magnitude lower than the one for the here investigated SAM [94]. Remarkably, these cross-sections are on the same order of magnitude like the ones determined for the diluted azobenzene SAMs as discussed in section 3.3.3 and for the tripodal linker based azobenzene SAMs [95]. Furthermore, in the liquid phase comparable quantum yields for azobenzene [227] and numerous fulgimide derivatives [228] and equally fast excited state dynamics for both types of chromophores [229], [184, 185] were found. It is hence tempting to conclude from the comparably large cross-sections on an equally efficient decoupling of both photochromic units from the respective substrates and on an intramolecular conversion mechanism for the two photochromic systems.

The mono-exponential fits to the data imply a non-cooperative switching behavior, i.e., the absence of a collective switching mediated *via* nearest neighbor interactions [165]. Regarding the considerable separation of visible and UV absorption band of the colored C- and open E-fulgimide [163], respectively, it is likely that the absence of the C-form in the open-PSS observed in so-

lution [80] can also be assumed for the photochromic interface. At least for the ring-closure reaction, the absence of initially present 'seeding' isomers can accordingly be concluded. Although this argument does not hold for the ring-opening reaction, the data on both reaction paths solely show the saturating behavior and no initial exponential growth due to an increasing number of 'seeds'. A non-cooperative scenario appears thus to be more likely.

3.2.5. Summary: Fulgimide SAMs

The Si(111) surface modified by means of a fulgimide-functionalized self-assembled monolayer has been investigated due to the high potential of the well-defined organic/inorganic hybrid system for application in emerging optoelectronic and photonic technologies which arise from coupling photochromic and non-linear optical properties. Indeed, the reversible conversion ability of the photochromic interface between two PSSs has been found. The interruption of the electronic conjugation of the π-system in the photoinduced ring-opening reaction results in a substantial NLO contrast and accordingly in a difference of 17 ± 6 % between the SHG signal amplitudes of the respective photostationary states. Regarding possible future applications, the observed thermal stability of both PSSs at room temperature and the complete reversibility of the conversion reactions are as important characteristics of the investigated system as the high efficiency of the latter in terms of the cross-sections of $\sigma_{\mathrm{E}\to\mathrm{C}} = 2.3 \pm 0.3 \cdot 10^{-18}\mathrm{cm}^2$ and $\sigma_{\mathrm{C}\to\mathrm{E}} = 1.2 \pm 0.3 \cdot 10^{-18}\mathrm{cm}^2$ for ring-closure and -opening, respectively.

Furthermore, the assignment of the observed NLO contrast upon illumination to originate from the light-induced ring-opening and -closure reactions, has been verified *via* density functional theory as well as correlated wave-function method calculations. In conjunction with polarization-resolved SHG measurements, the theoretical results also allowed to conclude on the molecular alignment. First, the interruption in the electronic conjugation of the four-ring π-system of the C-fulgimide due to the torsion between the indole and imide planes for the open isomers results in a significant difference in the second order non-linear susceptibility and accordingly in a pronounced NLO contrast. Second, the alignment of the chromophores is predominantly parallel to the surface normal and the NLO contrast therefore applies perpendicular to the photochromic interface.

In summary, the aim to design a thermally stable, well-defined organic/inorganic hybrid system with efficiently and reversibly switchable non-linear optical properties has been achieved. Furthermore, the SHG probe has been proven to provide the appropriate means to read out the switching state of the photochromic interface *via* the non-linear optical response. The NLO contrast might even be improvable by chemically modifying the electronic structure of

the investigated fulgimide. The two possible achievements in this regard are: (a) an increased difference in the first hyperpolarizabilities between the E- and the C-fulgimide as a molecular parameter and (b) an increased difference in the interfacial second order non-linear susceptibility as a system parameter, by suppressing the undesired E $\rightarrow$ Z reaction which reduces the E $\rightarrow$ C yield.

3.3. Reversible Photoisomerization of Azobenzene-Functionalized Self-Assembled Monolayers

As already mentioned for the fulgimide SAM, the creation of a photochromic interface exhibiting reversibly controllable non-linear optical properties constitutes an important step en route towards novel photonic and optoelectronic devices [48, 58–72]. Due to reversibility and speed of the photoswitching process and the simplicity of chemical modification and incorporation into complex molecular structures [197], the prototypal molecular switch azobenzene is a promising aspirant in this regard. It is demonstrated here, that the strategy of a surface immobilization *via* incorporation into 'diluted' SAMs [79,80,100,101,104,164], i.e., by intermixing unmodified linker chains between the chromophore-functionalized alkyl groups, indeed preserves the switching ability.

Furthermore, a pronounced and fully reversible SHG signal amplitude alteration is observed for the azobenzene SAM diluted to a chromophore concentration of 75 ± 5 % upon illumination with UV and visible light which is attributed to the *trans* $\leftrightarrow$ *cis* isomerization (section 3.3.1). Polarization-resolved SHG measurements confirm the presumed primarily upright orientation of the *trans*-isomer [99–104] and indicate an into-plain bending of the beforehand interface-averted 'upper' phenyl-ring upon isomerization (section 3.3.2). In addition, the large isomerization cross-sections indicate an efficient decoupling of the chromophore unit from the substrate (section 3.3.3). The suppression of the photoisomerization ability is found to be a progressing effect which initiates already at intermediate coverages, justifying the dilution strategy (section 3.3.4). The thermal stability of the photostationary states, finally, appears to depend on the presence of ambient water. At room temperature a thermally induced *cis* $\rightarrow$ *trans* back reaction is observed under a protective gas atmosphere, but not if the sample is exposed to air (section 3.3.5).

3.3.1. Non-Linear Optical Contrast and Reversibility

The azobenzene SAM containing 75 ± 5 % chromophore-functionalized alkyl chains is illuminated with UV (365 nm, photon dose of $n_{\mathrm{UV}} = 1.3 \cdot 10^{20}$ cm^{-2}) and visible (445 nm, $n_{\mathrm{vis}} = 4.4 \cdot 10^{19}$ cm^{-2}) light to trigger the *trans* $\rightarrow$ *cis* isomerization and *vice versa*, respectively. As verified quantitatively in the following section, these photon doses are approximately one order of magnitude higher than required to reach the respective photostationary states.

Figure 3.9A shows the data obtained by alternately illuminating the azobenzene SAM and measuring the SHG signal amplitudes. The switching of the NLO response is found to be fully reversible over 19 illumination steps indicat-

ing no fatigue or laser-induced damage of the azobenzene SAM. The average change of the SHG signal amplitude which corresponds to the NLO contrast between *trans*- and *cis*-PSSs, is 19 ± 3 %. The 'geometric' reorientation of the π-system and according reduction of the electronic conjugation of the SAM perpendicular to the interface, which is the reason for this significant difference in the respective second order non-linear susceptibilities of the interface, is schematically illustrated in figure 3.9B.

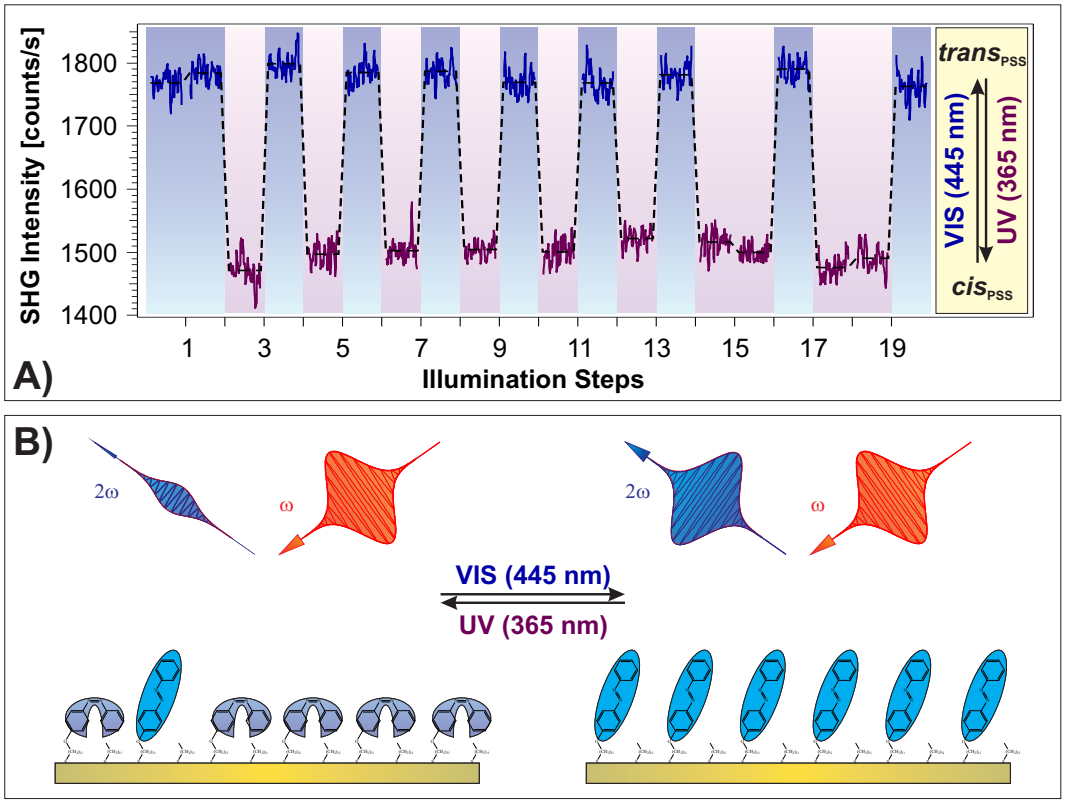

Figure 3.9. Reversible photoswitching of the NLO response of the azobenzene SAM. (A) The SHG data labeled in purple and blue denote measurements conducted subsequent to UV (365 nm, photon dose $n_{\mathrm{UV}} = 1.3 \cdot 10^{20}$ cm^{-2}) and visible (445 nm, $n_{\mathrm{vis}} = 4.4 \cdot 10^{19}$ cm^{-2}) light illumination, respectively. The pronounced NLO contrast results in SHG signal amplitude changes of 19 ± 3 % and is attributed to the *trans* $\leftrightarrow$ *cis* isomerization. (B) Illustration of the correlation between the NLO contrast measured in the SHG experiment and the 'geometric' rearrangement of the π-electron system in the isomerization.

As already mentioned in the introduction of this chapter, the samples are prepared under exclusion of UV light and should therefore solely contain azobenzene chromophores immobilized in their thermally favorable *trans*-form

[201, 204] prior to the illumination experiments. Accordingly, a comparison of the initial SHG signal amplitude prior to any light exposure and the average *trans*-PSS signal level, allows to estimate the isomer ratio in the *trans*-PSS. The prerequisite is the validity of the approximate proportionality of the isomerization-induced SHG signal amplitude change and the number of switched chromophores (equation 2.8). As depicted in figure D.1 of appendix D, the respective signal levels are equal within the given experimental accuracy. The upper limit of the fraction of *cis*-isomers in the *trans*-PSS is thus estimated not to be higher than approximately 20 %. This is a smaller fraction in comparison to the 25-30 % measured for a similar azobenzene solved in ethanol. However, this difference might be attributable to a shift of the absorption bands of the isomers due to the different chromophore environments in SAM and solution, respectively [161].

3.3.2. Interfacial Molecular Alignment

The results of the polarization-resolved SHG measurements on the azobenzene-functionalized SAMs are shown in figure 3.10. The data are obtained by setting the probe beam polarization to either 'p-in' (figure 3.10A) or 's-in' (figure 3.10B) which refer to an electric field vector aligned under an angle of 45° relatively to the surface normal or parallel to the interface, respectively. In addition, the polarization of the outgoing SHG beam is analyzed. The results on the s- and p-polarized 400 nm detection are shown in red and green ('s-out') and black and blue ('p-out'), respectively. Finally, each measurement is conducted on the *trans*- and the *cis*-PSS indicated by brighter and lighter colors, respectively. SHG signal amplitude changes induced by switching to the *cis*-PSS are indicated by the black arrows. The data are normalized with respect to the most intense component (p-polarized probe and detection, *trans*-PSS, black).

Four important observations can be derived from the depicted data. (1) Measuring with a p-polarized probe beam, i.e., when the probing electric field has a component perpendicular to the interface, results in SHG signal amplitudes which are two orders of magnitude larger than the ones measured for the s-polarized probe beam (cf. figure 3.10A *vs.* B). (2) The p-in/p-out polarization combination results in approximately one order of magnitude larger SHG intensities in relation to the p-in/s-out polarization setting (figure 3.10A black *vs* red curves). (3) The SHG signal amplitude measured with a p-polarized probe beam significantly decreases when switching from *trans*- to *cis*-azobenzene (figure 3.10A). (4) The SHG intensity measured using an s-polarized probe beam increases in the *trans* $\rightarrow$ *cis* isomerization (figure 3.10B).

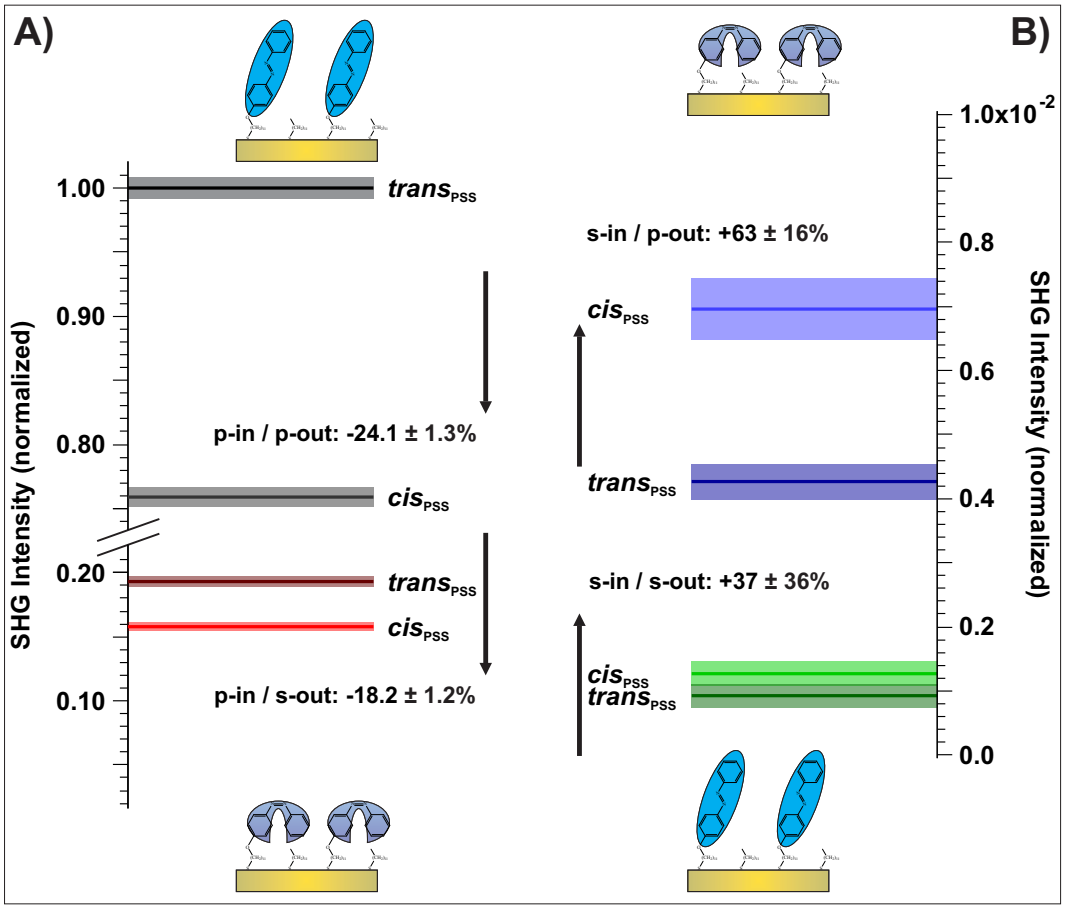

Figure 3.10. Results of the polarization-resolved SHG measurements on the azobenzene SAM for the polarization combinations (A) p-in/p-out (black) and p-in/s-out (red) and (B) s-in/p-out (blue) and s-in/s-out (green), where 'in' and 'out' denote the polarizations of the 800 nm probe and the 400 nm SHG beam, respectively. Darker colors in both panels represent the *trans*-PSS. Colored areas indicate the experimental uncertainty. Data normalized with respect to the most intense component (p-in/p-out, *trans*-PSS) for comparability.

Detailed theoretical calculations on the molecular hyperpolarizabilities are necessary to conclude from this data on the precise interfacial molecular alignment. Nevertheless, several implications resulting from these substantial differences upon varying the polarization settings can be derived. (1) The substantial difference in the SHG signal amplitude when measuring with a p- and an s-polarized probe beam, respectively, confirms the expectation that the *trans*-isomers are oriented perpendicularly to the surface. Note that: (a) the *cis*-PSS also contains a considerable number of molecules in the *trans*-state [161] and (b) a background exists which is attributable to the linker chains. As these are

inversion symmetric, the alkyl groups contribute to the second order nonlinear –surface– susceptibility *via* the hyperpolarizability along the chains which is interrupted at the symmetry breaking interface. A substantial contribution to the SHG signal amplitude measured with a p-polarized probe beam thus supports the expectation of a highly ordered, perpendicularly oriented self-assembled monolayer [99–104]. (2) That the p-in/s-out polarization setting also results in larger SHG signal levels in comparison to the measurements using an s-polarized probe beam, might indicate towards a slight tilting of the chromophores with respect to the surface normal for the azobenzene SAM with a chromophore packing density of 75 ± 5 %. The reason is that in this polarization combination the minor-diagonal components of the $\chi^{(2)}$ tensor are probed, which describe a correlation between the non-linear polarizability in the z-direction and along the other axes. (3) The pronounced decrease in the SHG signal amplitude measured perpendicular to the surface and its simultaneous increase parallel to the interface upon the *trans* $\rightarrow$ *cis* isomerization indicate an into-plain bending of the beforehand interface-averted 'upper' phenyl-ring, as the corresponding rearrangement of the π-electron system can be expected to result in a pronounced alteration of the interfacial second order non-linear susceptibility.

3.3.3. Isomerization Cross-Sections

In order to determine the efficiency of the isomerization reactions in terms of the respective cross-sections, the sample is illuminated applying sufficiently low photon fluxes of $f_{\mathrm{vis}} = 5.4 \cdot 10^{15}$ s^{-1}cm^{-2} (445 nm) and $f_{\mathrm{UV}} = 1.3 \cdot 10^{16}$ s^{-1}cm^{-2} (365 nm). In figure 3.11A and B the measured SHG signals are shown along with mono-exponential fits according to equation 2.14. The cross-sections obtained from these fits are $\sigma_{\mathrm{vis}} = 3.1 \pm 0.2 \cdot 10^{-18}$ cm^2 and $\sigma_{\mathrm{UV}} = 0.7 \pm 0.1 \cdot 10^{-18}$ cm^2 for the *cis* $\rightarrow$ *trans* and the *trans* $\rightarrow$ *cis* isomerization, respectively.

The comparison to azobenzene SAMs with rather large free space per molecule [95, 96] and to the fulgimide SAM in which only approximately every fourth linker chain is chromophore-functionalized which both exhibit comparable isomerization cross-sections on the one hand and to the four orders of magnitude less efficiently substrate-mediated photoswitching of the physisorbed system TBA/Au(111) [94] on the other hand, reveals the efficiency of the here investigated switching processes. It furthermore indicates the absence of an excitonic coupling for a major part of the chromophores at the packing density of 75 ± 5 % and an effective decoupling between the functional unit and the substrate and hence leads to the tempting conclusion on an intramolecular photoexcitation mechanism.

Judging from the mono-exponential correlation between the photon dose and the fraction of switched molecules on a non-cooperative switching behavior in

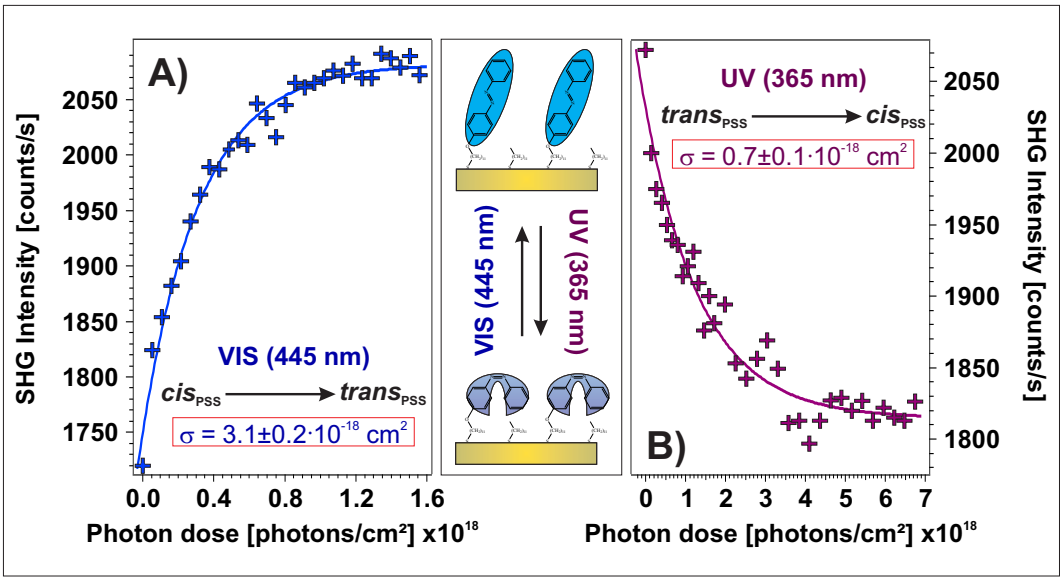

Figure 3.11. Cross-sections of *cis* → *trans* (A) and *trans* → *cis* (B) isomerization upon illumination with 445 nm and 365 nm, respectively. Shown are the respective SHG signal amplitudes as a function of the photon dose. The mono-exponential fits yield $\sigma_{\mathrm{vis}} = 3.1 \pm 0.2 \cdot 10^{-18}$ cm^2 and $\sigma_{\mathrm{UV}} = 0.7 \pm 0.1 \cdot 10^{-18}$ cm^2, respectively.

contrast to the switching of complete domains mediated by nearest-neighbor interaction observed for another system [165], is only possible with one restriction. As mentioned in section 3.1.2, due to (a) overlapping absorption bands of the isomers and (b) the statistical probability of an excited chromophore to relax back to the initial form, both the *trans*- and the *cis*-PSS contain a considerable residual fraction of the respective other isomer [161]. Whether the respective residual isomers serve as 'seeds' in a cooperative back-isomerization cannot be concluded. However, as the data on both isomerization paths solely show the saturating behavior and no initial exponential growth due to an increasing number of 'seeds', a non-cooperative scenario appears to be more likely.

It is remarkable that the cross-section of the *cis* → *trans* isomerization triggered by visible light illumination is larger than the one of the UV light-induced *trans* → *cis* conformation when considering the respective absorption bands of the two isomers [160]. Furthermore, the opposite is observed for a similar system [95], as expected. Whether this unusual finding is the result of (a) a shift in the absorption bands in comparison to solution due to the chemical attachment to the alkyl chain as mentioned above, or (b) the alignment of the transition dipole moments which can be expected to be different for the here in-

vestigated SAM in comparison to the large linker system studied by Wagner *et al.* [95], cannot be concluded. Further investigations are accordingly necessary, for instance by means of polarization-resolved UV/visible spectroscopy [162], a combined NEXAFWS and density functional theory approach [102, 177] or *via* a theoretical modeling of the measured polarization-resolved SHG data. The latter is currently in progress.

3.3.4. Influence of the Chromophore Packing Density on the Isomerization Ability

Figure 3.12 displays the results concerning the influence of chromophore packing density on the isomerization ability of the azobenzene SAMs. Samples with packing densities of 10 ± 5 %, 30 ± 5 %, 50 ± 5 %, 75 ± 5 % and 95 ± 5 % are examined (figure 3.12A). The average SHG signal amplitude contrasts of 3.2 ± 0.9 %, 18.1 ± 3.0 %, 18.9 ± 3.4 %, 18.9 ± 2.6 % and 2.3 ± 1.5 % are found, respectively (figure 3.12B).

The contrast does obviously not correlate linearly with the number of available chromophores. Given as a guide to the eye are two lines through the origin labeled 'min' and 'max', which represent fits through the first and the second data point (10 ± 5 % and 30 ± 5 %) and through the first and the fourth data point (10 ± 5 % and 75 ± 5 %), respectively. The red highlighted area resulting from these extrapolations constitutes the expected observable NLO contrast, when assuming a linear correlation between the number of immobilized chromophores and the switching-inducible SHG signal amplitude change. The obvious result is, that the NLO contrast measured for the 95 ± 5 % SAM is significantly lower than expected for a linear correlation (cf. 'min' in figure 3.12B). A quenching mechanism, i.e., either steric hindrance or an excitonic coupling as discussed in the introduction to this chapter is thus undoubtedly operative. The second finding derived from the data displayed in figure 3.12B is, that the quenching of the photoisomerization ability is a progressing effect. On the one hand, apparently already at intermediate coverages an increasing amount of chromophores is unable to switch as at least the NLO contrast measured for the 75 ± 5 % SAM is incompatible with the values determined for the SAMs with lower coverages (cf. 'max' in figure 3.12B). On the other hand, this result confirms the statistical mixture of chromophore-functionalized alkyl chains with the unmodified linkers found in XPS measurements for the here investigated [162] and a similar azobenzene SAM [177]. Upon immersion, the molecules apparently arrange to maximize the free space per molecule. This might either be mediated by a dipole–dipole repulsion among the azobenzene molecules [213, 230] or by a fully statistical distribution, if the van der Waals interaction strength among the chromophores is neglectable in comparison to the one between the alkyl chains. However, at a certain intermediate coverage,

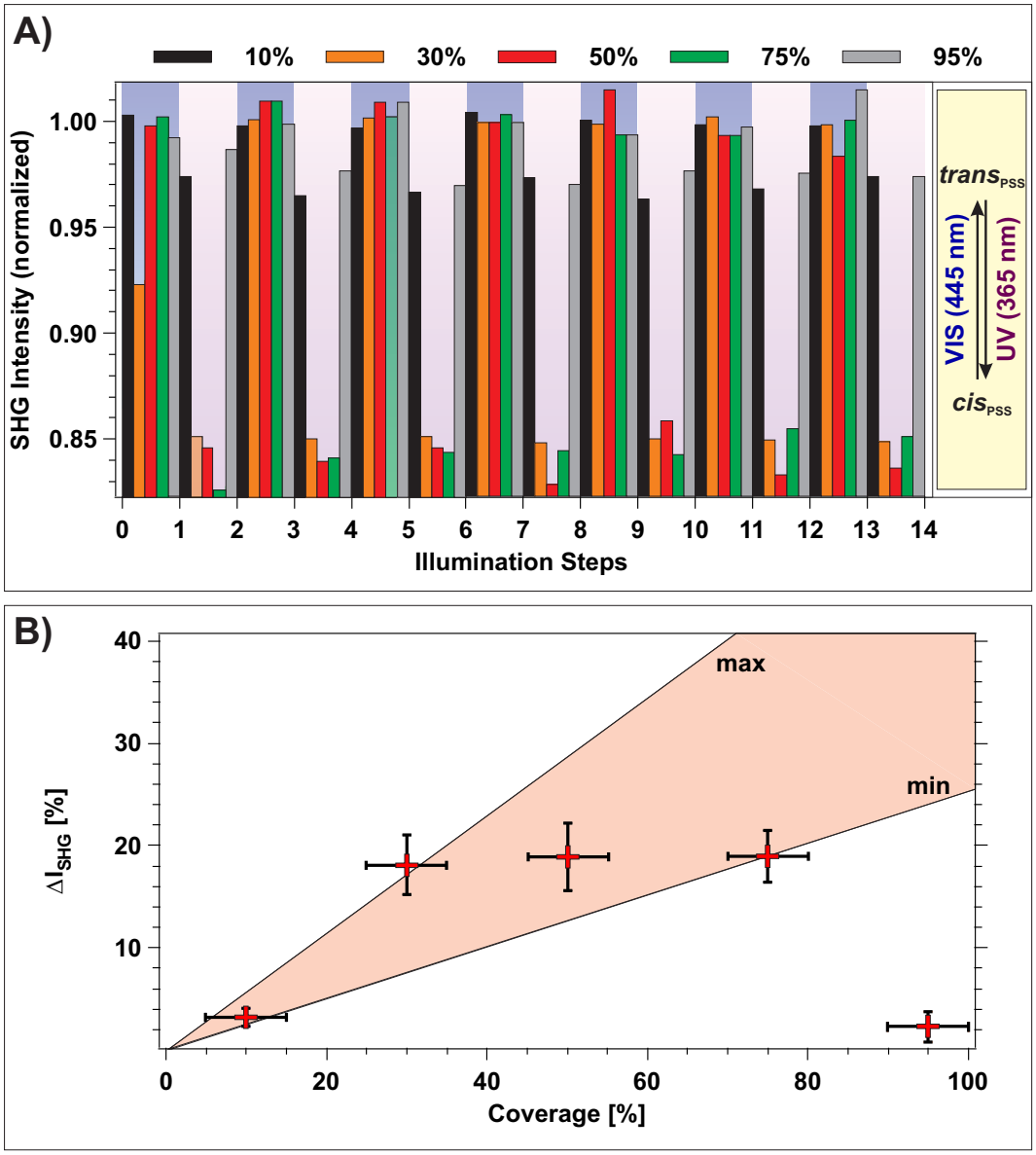

Figure 3.12. (A) Isomerization-induced SHG signal amplitude changes upon illumination with 365 nm and 445 nm of SAMs with different chromophore packing densities: 10 ± 5 % (black), 30 ± 5 % (orange), 50 ± 5 % (red), 75 ± 5 % (green) and 95 ± 5 % (gray). Data normalized to the average *trans*-PSS signal level of the 75 ± 5 % SAM for comparison. (B) Average NLO contrasts $\Delta I_{\mathrm{SHG}} = [I_{\mathrm{SHG}}(trans_{\mathrm{PSS}}) - I_{\mathrm{SHG}}(cis_{\mathrm{PSS}})]/I_{\mathrm{SHG}}(cis_{\mathrm{PSS}})$ as a function of the chromophore packing density. Comparably high contrasts are found for the intermediate coverages of 30 ± 5 %, 50 ± 5 % and 75 ± 5 %. However, it is considerably lower for the 10 ± 5 % and 95 ± 5 % samples, due to a lower amount of chromophores and hindrance of the photoisomerization ability, respectively.

the average intermolecular distance becomes to low to either provide sufficient free space for each chromophore to switch to the three-dimensional *cis*-form or to avoid an excitonic coupling among adjacent chromophores, depending on the exact quenching mechanism. Consequently, a further increase of the chromophore packing density from this point on, reduces the number of switchable chromophores.

In summary, the strategy of intermixing alkyl chains as spacer groups is justified by the observed quenching of the photoisomerization ability which is a progressing effect with an onset at intermediate coverages. Furthermore, the NLO contrast of the azobenzene SAM is found to be approximately constant in the range between 30 ± 5 % and 75 ± 5 % surface coverage. In this intermediate coverage regime, apparently a balance between an increasing number of chromophores and the progressing quenching of the photoisomerization ability of an increasing amount of chromophoric units exists.

3.3.5. Thermal Stability

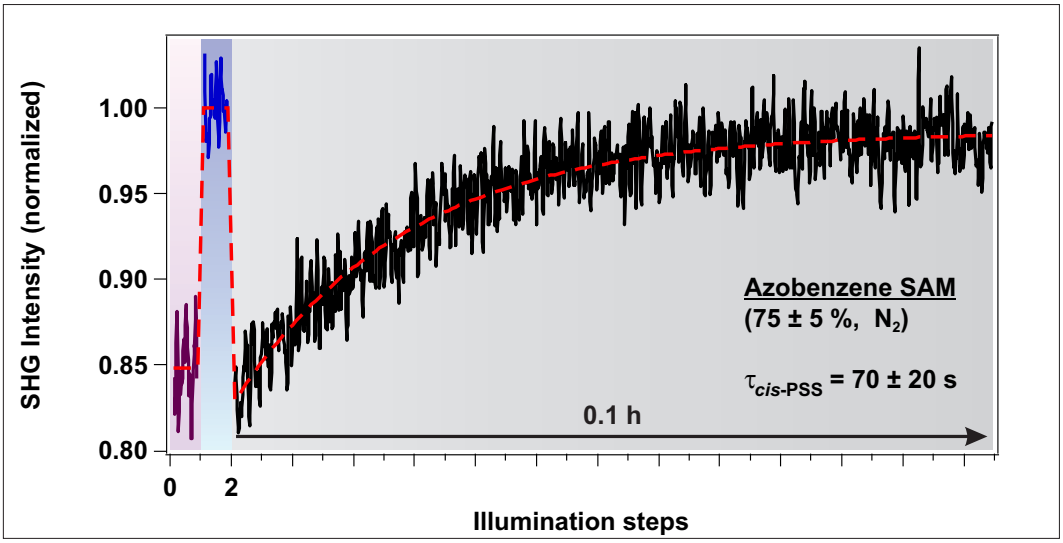

Figure 3.13. For the azobenzene sample with a packing density of 75 % a complete thermal *cis* → *trans* back-reaction is found to occur with a time-constant of $\tau_{cis\text{-PSS}} = 70 \pm 20$ s at room temperature when measuring under an inert gas (nitrogen, purity '5.0') atmosphere.

The results regarding the 75 % sample discussed in the previous sections 3.3.1, 3.3.2 and 3.3.3 are obtained by conducting the SHG illumination experiments in air. The reason for the choice not to measure in an inert gas (nitrogen, purity '5.0') atmosphere becomes evident from the data obtained for the initial exper-

iments conducted under a protective gas atmosphere, shown in figure 3.13. Under theses conditions, the *cis*-PSS is thermally unstable at room temperature. The sample switches completely back to the *trans*-PSS with a time-constant of $\tau_{cis\text{-PSS}} = 70 \pm 20$ s which is comparable to the one found for a similar diluted azobenzene SAM investigated under UHV conditions [101]. Repeating the illumination experiments on the same sample without the protective gas atmosphere, i.e., with the sample exposed to air, results in the data shown in figure 3.14. At these conditions, no indication for a thermal back-reaction is found within 1.5 h. This finding is of paramount importance as a thermal effect on the measurements described in the previous sections 3.3.1, 3.3.2 and 3.3.3 can accordingly be excluded. However, as exemplary shown for the 30 % sample in figure 3.15, the *cis*-PSSs of the other azobenzene SAMs are only partially stable at ambient conditions. The destabilization towards the *trans*-PSS occurs with a time-constant of $\tau_{cis\text{-PSS}} = 160 \pm 20$ s and accordingly by a factor of two slower in comparison to the 75 % sample under protective gas atmosphere. The thermal back-reaction stops at an intermediate SHG signal amplitude corresponding to roughly half of the chromophores in either switching state. This intermediate state is thermally stable for at least 17 h and can efficiently be switched back to the *trans*-PSS by means of 445 nm illumination, as also shown in figure 3.15. Preparation and measurement conditions are equal for the 75 % SAM and the other samples except for the humidity of approximately 60 ± 20 % and 30 ± 20 %, respectively.

In summary, three experiments on the influence of the presence of water on the thermal stability of the *cis*-PSS of the azobenzene SAMs are conducted, yielding the following results. (1) A fast and completely thermally mediated *cis* $\rightarrow$ *trans* back-reaction is observed for measurements under the protective nitrogen atmosphere. (2) A slower and only partial thermal back-reaction to a thermally stable intermediate state occurs, when measuring at low humidity. (3) The complete thermal stability of the *cis*-PSS is found at high humidity. In accordance with the instability of the UV-PSS under UHV conditions [101], this allows for the assumption that the co-adsorption of water apparently increases the barrier for a thermal back-reaction and thus stabilizes the *cis*-isomer. However, these results demand for further experimental and theoretical investigations.

It is necessary to elucidate the influence of the thermal effect on the correctness of the determined NLO contrasts of the SAMs with packing densities of 10 ± 5 %, 30 ± 5 %, 50 ± 5 % and 95 ± 5 % (section 3.3.4). The thermal back-reaction opposes the UV light-induced *trans* $\rightarrow$ *cis* isomerization and the measured SHG signal amplitude changes might thus be too small and accordingly not comparable to the NLO contrast of the thermally stable 75 % sample. The data discussed in section 3.3.3 yields a time-constant of 61 ± 4 s to switch the sample back to the *trans*-PSS by means of an illumination with 445 nm

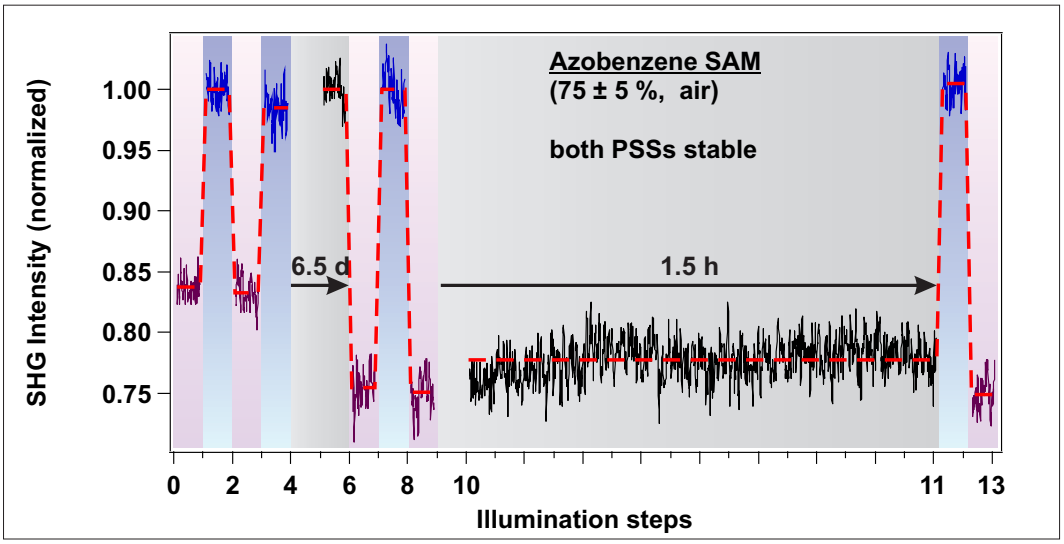

Figure 3.14. No indication for a thermal back-reaction at room temperature is found within 1.5 h for the 75 % azobenzene SAM when measuring at air.

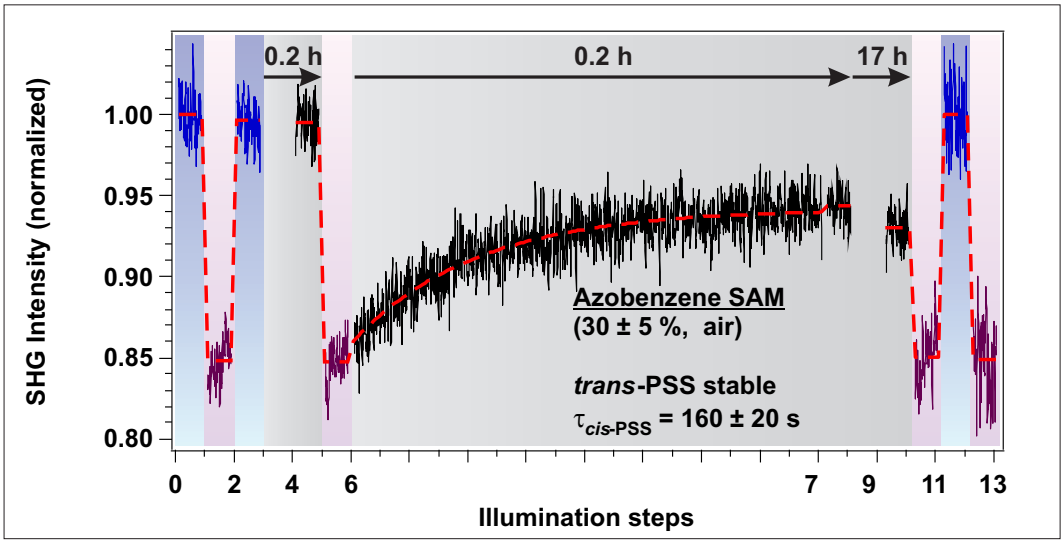

Figure 3.15. At low humidity a thermally induced back-isomerization to an intermediate state with a time-constant of $\tau_{cis\text{-PSS}} = 160 \pm 20$ s is observed as shown here for the 30 % sample. This state apparently contains approximately equal amounts of both isomers according to the respective SHG signal amplitudes. It is thermally stable for at least 17 h and can efficiently be switched back to the *trans*-PSS by means of by 445 nm illumination.

visible light at a power per area of $p_{\mathrm{vis}} = 2.4 \cdot 10^{-3}$ W/cm^2.

The comparison to the 160 ± 20 s measured for the thermal back-reaction allows to derive a 'power per area equivalent' (i.e., the power density needed to achieve the 445 nm illumination photoisomerization in the same time which the thermal back-reaction takes) of $p_{\mathrm{eqi.}} = 9.3 \pm 0.3 \cdot 10^{-4}$ W/cm^2. At the same time, the sample is illuminated with UV light at 365 nm which opposes the thermal reaction with a power density of $p_{\mathrm{UV}} = 11.6 \cdot 10^{-2}$ W/cm^2. Additionally considering a weighting-factor due to the different respective cross-sections of $\sigma_{\mathrm{vis}}/\sigma_{\mathrm{UV}} = 4.4 \pm 0.7$, these counteracting effects can be compared. The fraction of thermally switched *trans*-isomers in the *cis*-PSS is estimated to be 4 ± 2 % and thus below the given experimental resolution. The NLO contrasts determined in section 3.3.4 for the azobenzene SAMs with different packing densities are accordingly correct, as is the comparison of this data to the value measured for the thermally stable 75 % sample.

3.3.6. Summary: Azobenzene SAMs

Reversible control over the switching states of a self-assembled monolayer consisting of a three-to-one mixture of azobenzene-functionalized alkyl chains and unmodified linkers on gold has been demonstrated. The *trans* $\leftrightarrow$ *cis* isomerization has been triggered by illumination with visible (445 nm) and UV (365 nm) light, respectively, and the switching state of the photochromic interface has been read out *via* the difference in the second order non-linear susceptibility between the respective PSSs. The resulting observed average SHG signal amplitude change was determined to be 19 ± 3 %. Investigations on a correlation between the chromophore packing density and the isomerization ability by comparing the respective NLO contrasts revealed that this value is close to the optimum achievable compromise between the number of contributing chromophores and a progressing quenching of the isomerization ability with increasing packing density. The progressive quenching appears to be in agreement with the statistical mixtures of the two types of molecules found in XPS measurements for the here investigated [162] and similar azobenzene SAMs [177]. Apparently, the decreasing intermolecular distance increases the probability of an excitonic coupling between adjacent chromophores or results in steric hindrance. The applied strategy of intermixing unmodified spacer chains among the azobenzene-functionalized alkyl groups is thus justified.

It is surprising that the height of the barrier against the thermally induced *cis* $\rightarrow$ *trans* back-isomerization was found to depend on the amount of ambient water. A thermal stabilization of the meta-stable *cis*-isomer appears to be achievable *via* water co-adsorption. At room temperature, a thermal stability of the *cis*-PSS has solely been observed at sufficiently humid conditions, while low humidity resulted in the formation of an intermediate ther-

mal/photostationary state, i.e., the stabilization of solely a fraction of the *cis*-molecules. Finally, when measuring in a protective nitrogen atmosphere, i.e., under exclusion of water, a complete thermal back-reaction occured on timescales of seconds. These findings demand for a further investigation for example by means of targeted water deposition in an UHV chamber or in temperature-controlled SHG measurements.

The determined cross-sections of $\sigma_{\mathrm{vis}} = 3.1 \pm 0.2 \cdot 10^{-18}$ cm^2 and $\sigma_{\mathrm{UV}} = 0.7 \pm 0.1 \cdot 10^{-18}$ cm^2 are on the one hand on the same order of magnitude as (a) the values reported for azobenzene SAMs with rather large free space per molecule [95,96] and (b) the fulgimide SAM in which only approximately every fourth linker chain is chromophore-functionalized. On the other hand, these values are four orders of magnitude higher in comparison to the substrate-mediated photoswitching of the physisorbed system TBA/Au(111) [94]. Thus, the efficiency of the here investigated switching processes is revealed and an effective decoupling between the functional unit and the substrate is indicated, which leads to the tempting conclusion that the photoisomerization is triggered by an intramolecular photoexcitation mechanism.

Polarization-resolved SHG measurements provided evidence for the assumed origin of the NLO contrast to arise from the 'geometric' rearrangement of the π-electron system and thus from the according reduction in the degree of electronic conjugation perpendicular to the interface in the *trans* $\rightarrow$ *cis* isomerization. The second order non-linear susceptibility perpendicular to the surface is two orders of magnitude larger than parallel to the interface and it significantly decreases when the beforehand interface-averted 'upper' phenyl-ring is bent into plane, while the parallel component increases in the *trans* $\rightarrow$ *cis* isomerization. Additional detailed information on the chromophore alignment is obtainable, *via* a theoretical modeling of the azobenzene hyperpolarizabilities in accordance to the measured polarization-resolved SHG data, which is currently in progress.

In summary, the here investigated photochromic interfaces are highly relevant for possible future applications in novel photonic and optoelectronic devices due to the reversibly switchable, substantial NLO contrast and the high efficiency of the isomerization processes. Regarding further investigations, an increase of the NLO contrast could even be possible. This might for instance be achievable by adding an intermediate layer with low susceptibility between the linker-chains and the functional head-group.

Chapter 4

Ultrafast Charge Transfer Across a Donor/Acceptor Interface

The organic semiconducting donor polymer P3HT and the electron acceptor molecule C_{60} are chosen to test the applicability of the time-resolved second harmonic generation setup for the investigation of the photoinduced exciton dynamics inherent to these prototypal materials for organic solar cells. In particular, the intrinsic interface sensitivity and the femtosecond temporal resolution render the TR-SHG technique suitable for monitoring the ultrafast charge transfer across the C_{60}/P3HT interface, which is a decisive process in the light-to-current conversion in organic photovoltaics. As outlined in the introduction given in section 4.1, no consensus currently exists on the detailed mechanisms from the initial photoabsorption to the electron transfer in general and on the involvement of 'hot excitons' in particular [15, 118, 121, 122, 132]. The latter term refers to the necessity of supplying excess energy in an above-bandgap excitation. The TR-SHG probe provides the means to investigate this correlation as: (a) such hot excitons can be assumed to be highly delocalized [117, 119] and thus to induce a strong distortion on the interfacial electron density which is reflected in the susceptibility tensor $\chi^{(2)}$ [136, 137], (b) the formation of an electric field between donor and acceptor due to the CT, which results in an electric field enhancement of the SHG signal [13] and (c) a variation of the pump beam wavelength allows to selectively tune the amount of excess energy. As outlined in sample preparation section 4.2, the reason for investigating the well-defined single heterojunction C_{60}/P3HT instead of the usually chosen bulk-heterojunction P3HT:PCBM [110, 124, 125] is the desired avoidance of the formation of undefined interfacial clusters and domains [126, 127] which potentially interferes with an unambiguous interpretation of the measured TR-SHG data.

For the pristine P3HT sample the initial excitation of hot singlet excitons is found. These subsequently thermalize and localize on an ultrafast timescale within the bands of the polymer (section 4.3). In the presence of the acceptor, an ultrafast charge transfer is identified as the dominating relaxation channel (section 4.4). Interestingly, the charge transfer yield correlates with the excita-

tion wavelength and increases with the amount of excess energy (section 4.5).

4.1. Introduction: Charge Carrier Dynamics in Organic Photovoltaics

Organic solar cells based on semiconducting polymers or molecules offer potential advantages over inorganic photovoltaic devices (IPVs), such as light weight, low-cost fabrication and mechanical flexibility [110]. However, the photoconversion mechanisms are completely different in the two types of devices which renders established design principles of IPVs non-transferable to the novel organic materials. Most fundamentally, the absorption of a photon inside an inorganic junction results in the creation of an almost unbound electron–hole pair while in OPVs excitons are produced, i.e., mobile excited states [231]. Although energetically excited, the electron–hole pairs in organic semiconductors are still rather tightly bound due to the poorly screened Coulomb barrier [15]. Their separation requires the incorporation of an electron attracting material and the intermediate step of charge transfer from the donating semiconducting polymer or molecule to the electron acceptor [232].

The by far most commonly used electron acceptors are fullerenes *viz.* C_{60} [233] as shown in figure 4.1 (top) and its solution processable derivative [6,6]-phenyl-C_n-butyric acid methyl ester (n = 61: $PC_{60}BM$, n = 71: $PC_{70}BM$) [123, 234, 235]. Due to their high electron affinity and the superior ability to transport charge, these molecules are considered the best acceptor component currently available for OPVs [236]. Although few alternatives as electron-accepting silicon nanocrystals are proposed [132, 237], ongoing development rather focuses on improving modifications on fullerene derivatives [238, 239].

Regarding the electron donating component, however, numerous materials are currently tested. These range from a wide variety of solution processable molecules and polymers [120, 240, 241] to polymers with explicitly low bandgaps as PCPDTBT (poly[2,6-(4,4-bis-(2-ethylhexyl)-4*H*-cyclopenta[2,1-b;3,4-b']-dithiophene)-*alt*-4,7-(2,1,3-benzothiadiazole)]) [242] which are of potential use in organic tandem solar cells [243] to molecules like pentacene which are promising candidates to exceed the Shockley-Queisser-limit *via* singlet fission [14,112–116]. However, most OPVs are based on the semiconducting polymer P3HT shown in figure 4.1 (bottom). This material 'replaced' polyphenylene vinylene (PPV) on which early work was focused [233, 244], due to the improved absorption and increased hole mobility [245]. As the film morphology is known to have a significant influence on the OPV performance [246], it is important to consider the respective alkyl chain substituent positions at neighboring thiophene rings: as two equivalent positions are available, a random and a periodic arrangement along the polymer chain are feasible. The de-

gree of 'regioregularity' (RR) affects the hole mobility which is only for purest RR-P3HT comparable to the electron transport properties of PCBM [247]. While the 'regiorandom' (RRa) polymer forms amorphous films upon spin coating [246], RR-P3HT self-organizes into lamella structures of weakly interacting H-aggregates, i.e., a π-stacking-mediated superstructure [248], with an interchain distance of approximately 3.8 Å [249]. The aggregation has a significant impact on the electronic properties of the film which manifests in the energy level splitting [250] responsible for the characteristic absorption spectrum of RR-P3HT films exhibiting a pronounced vibronic pattern (while it is featureless for RRa-P3HT) [251].

As exciton diffusion lengths in organic semiconductors are short in comparison to the film thicknesses necessary for efficient optical absorption [157] the realization of an OPV using a single heterojunction suffers from low external quantum efficiencies [125]. Blending the electron acceptors into the active layer is considered to circumvent this problem by enabling to tailor the donor and acceptor domain sizes *via* the preparation parameters and by drastically increasing the area of the interface [248]. Since the first reported realization of a solar cell based on a polymer:fullerene blend in 1995 [244], numerous studies have been published on photovoltaic devices based on the bulk-heterojunction concept. One of the most prominent donor/acceptor systems is P3HT:PCBM [124]. But the wide spread of reported efficiencies of devices based on this prototypal blend [110], all being well below the values reached by state-of-the-art inorganic multi-junction solar cells [252], indicates the need for further investigations of the underlying ultrafast photoinduced dynamics at the D/A interface.

In particular, the role of the excess energy from above-bandgap excitation currently experiences revision from being generally considered to be lost in waste heat [14]. On the one hand, recent findings indicate the crucial role of hot excitons: (1) for populating the CT states [117], (2) to overcome the poorly screened Coulomb barrier in organic semiconductors and avoid trapping in relaxed CT ground states localized at the interface [15] and (3) to enhance the probability of charge dissociation out of delocalized CT states [118]. Furthermore, although theoretical modeling is generally difficulty due to the large system sizes [15], wavefunction-based *ab initio* calculations recently revealed that the experimentally observed delocalization of excitonic states accompanying the high energetic excitation [117] is crucial to the stabilization of the CT states [119]. On the other hand, for the ultrafast charge separation into band-like acceptor states in blends of small molecules and polymers with fullerenes, respectively, no indication for the need of thermal (i.e., in the sense of Onsager-like models [253]) excess energy has been found [120]. Furthermore, no correlation between the excitation energy and the external quantum efficiency (EQE) of a variety of OPV model systems has been found in recent exten-

sive studies [121, 122]. These contradicting results emphasize the necessity of a better understanding of the light-to-current conversion processes in organic votovoltaics.

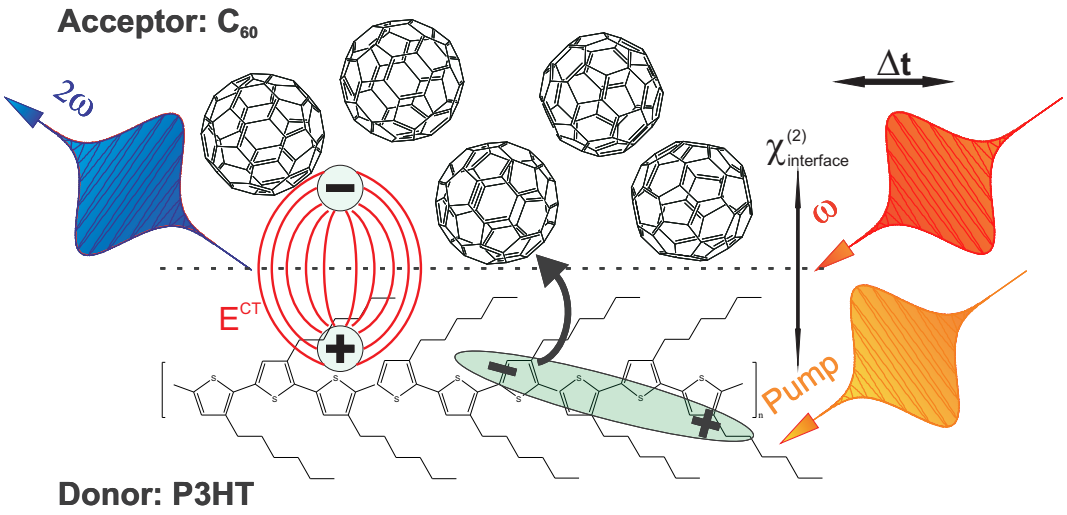

Figure 4.1. Schematic illustration of the TR-SHG experiment. A pump pulse generates hot, delocalized excitons in the semiconducting polymer P3HT. The corresponding distortion of the electron density is reflected in the second order non-linear susceptibility $\chi^{(2)}$ which is sampled by the probe pulse. In the presence of the electron acceptor C_{60} a charge transfer is possible. The corresponding formation of an interfacial electric field amplifies the SHG signal (EFISH). The introduction of a variable temporal delay Δt between the laser beams allows for monitoring the temporal evolution of the excitonic population and the CT dynamics in TR-SHG experiments.

Figure 4.1 illustrates, how time-resolved second harmonic generation is applied to investigate the charge transfer dynamics at the donor/acceptor interface on a femtosecond timescale. The applied 800 nm wavelength of the probe beam corresponds to a photon energy of 1.55 eV which is not absorbed by neither of the investigated compounds [12, 254]. While the pump photon energies of 2.15 eV to 1.90 eV are still well below the bandgap energy of the acceptor [39], the respective pump wavelengths of 576 nm to 652 nm are absorbed by the semiconducting polymer. Pump beam powers are kept below 3 mW which corresponds to an excitation intensity of 30 μJ/cm^2 close to the solar exposure [132], to avoid beam damage as monitored by means of iterative measurements and to exclude undesired effects as exciton–exciton annihilation [156–158] or even thermally induced absorbance shifts [159] as discussed below in terms of the SHG signal amplitude changes as a function of the pump beam power.

To prevent a degradation of the samples due to exposure to oxygen [149] or water [150], known to result in a loss in charge carrier mobility in organic donor polymers [151] all TR-SHG experiments are carried out under a protective gas atmosphere (nitrogen, purity '5.0').

4.2. Sample Preparation

Samples were prepared by Steffen Roland and Marcel Schubert in the group of Prof. Dieter Neher at the Institut für Physik und Astronomie at the Universität Potsdam by vacuum evaporation of C_{60} (99 % purity, purchased from MER, figure 4.1 top) and spin coating of RR-P3HT (regioregularity > 98 %, average molecular weight $< 50,000$ MW, purchased from BASF ('Sepiolid P200'), figure 4.1 bottom) onto optically polished sapphire substrates (purchased from CrysTec). The 15 g/l P3HT containing chlorobenzene solution was spun at 1800 rpm for 20 s at room temperature without additional annealing. Film thicknesses were in the case of C_{60} controlled *via* the dosing time which was calibrated by means of a quartz microbalance. For P3HT the absorbances were measured by means of UV/visible spectroscopy and gauged against the profilometrically determined height of the thickest film.

Pristine C_{60} and P3HT samples used as references with respect to the D/A sample. The latter was prepared by evaporating 12 nm C_{60} on top of a 50 nm thick P3HT absorption layer. Vacuum evaporation of the not soluble C_{60} was chosen instead of spin coating of PCBM to reduce diffusion of acceptor molecules into the donor layer. Stacked systems were selected instead of bulk-heterojunctions to reduce the complexity of the investigated system to a single, well-defined interface. This facilitates an unambiguous interpretation of the measured TR-SHG data as in bulk-heterojunctions a recombination associated with interrupted percolation pathways and cross-currents of electrons and holes cannot be excluded [132]. However, the photoinduced dynamics at the D/A interface of this model system can be expected to be very similar to those in P3HT:PCBM blends, as phase-separation results in the formation of domains of donor and acceptor molecules in the blends [126,127] and thus to (less well-) defined domain boundaries across which the charge transfer occurs in theses systems.

The verification of the success of the preparation strategy by means of polarization-resolved SHG measurements sensitive to interfacial roughness is given in appendix E.

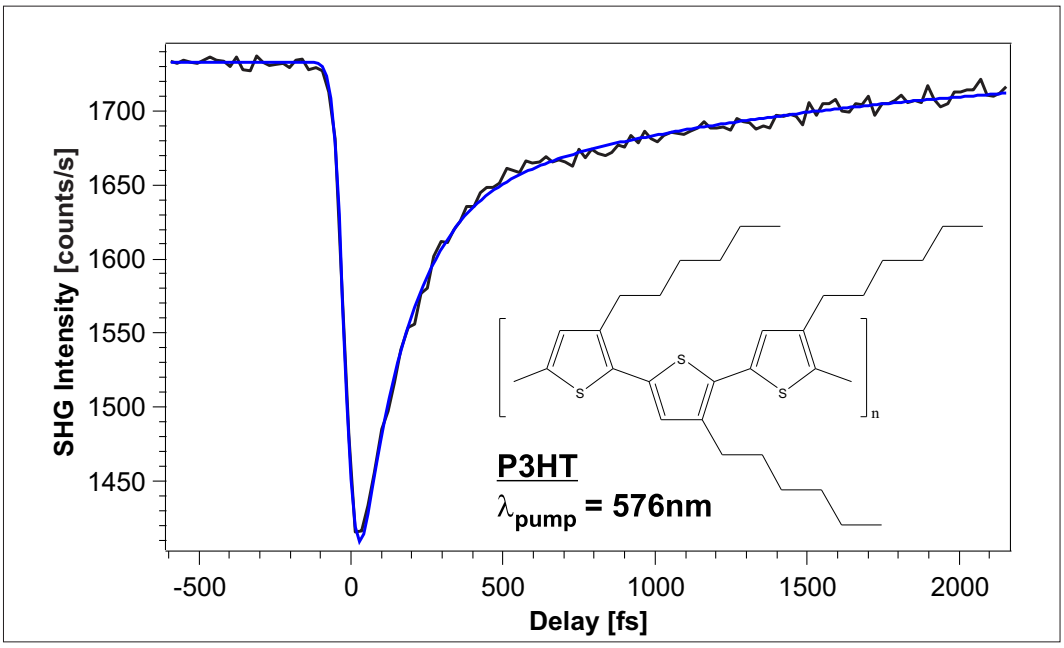

Figure 4.2. TR-SHG data of pristine P3HT. The pump beam induces a pronounced decrease in the SHG signal amplitude at time zero. The NLO response returns to the initial level within a few picoseconds. The fit (blue) is the iterative convolution of the cross-correlation with a bi-exponential function, yielding $\tau_1 = 154 \pm 6$ fs and $\tau_2 = 1370 \pm 80$ fs. The changes in the NLO response are attributed to the initial excitation and subsequent thermalization and localization of hot singlet excitons.

4.3. Exciton Dynamics in Pristine P3HT and C_{60}

Figure 4.2 shows the TR-SHG data of pristine P3HT. The pump-induced excitation at time zero leads to a decrease in the SHG signal amplitude which returns to the initial level within a few picoseconds. The data are fitted (blue curve) by iteratively convoluting the Gaussian profile of the cross-correlation of pump and probe pulses with a bi-exponential function yielding $\tau_1 = 154 \pm 6$ fs and $\tau_2 = 1370 \pm 80$ fs. Numerous studies have been conducted for the polymer, mostly based on time-resolved transient absorption spectroscopy. Consensus on the nature of the initial excitation apparently exists, that singlet excitons are immediately excited [128–133], although in some reports the possibility of an additional instantaneous population of polarons [130, 131], polaron pairs [128, 133] and even free charges [129] is discussed. In contrast, other groups report on the formation of interchain polarons not initially but

within less than one picosecond out of the initial singlet population [132], which might also explain the here observed time-constants. Another explanation for the fast decay of the TR-SHG signal might be the geminate recombination of polaron pairs reported by few groups [128, 133] while in contrast others attribute these decay channels to time-constants of hundreds of picoseconds or longer [129, 131, 255]. Regarding the aforementioned ultrafast interchain polaron formation, the question would be, why the SHG signal amplitude decreases by more than 20 % for the excitation of singlet excitons, while the presence of interchain polarons does not affect the signal level, in contrast. Considering the influence of excess charges and unscreened dipoles on the non-linear susceptibility of surrounding molecules revealed in theoretical studies and hyper Raman scattering experiments [136, 137], an alternative explanation for the observed dynamics appears to be more likely. It is known that the initial hot exciton population is highly delocalized and that their thermalization is accompanied by localization on ultrafast timescales [117, 130, 134, 135]. This delocalization can consequently be assumed to induce pronounced distortions in the electron density. As the latter correlates with the non-linear susceptibility, the observed TR-SHG signal evolution is assigned to originate from the initial excitation and subsequent energetic relaxation and corresponding localization of hot singlet excitons.

To elucidate why the thermalization within the donor occurs with two time-constants, the sample is investigated by means of spectroscopic SHG and UV/visible absorption measurements, the latter conducted by Marcel Schubert in the group of Prof. Dieter Neher at the Institut für Physik und Astronomie at the Universität Potsdam. Figure 4.3A shows the TR-SHG data on pristine P3HT obtained for different excitation wavelengths. In contrast to the bi-exponential decay found using pump wavelengths of 576 nm and 618 nm, only the fast decay is observed subsequently to the 652 nm excitation, yielding $\tau = 160 \pm 50$ fs. This is the only applied wavelength insufficient for the population of the S_2 band as depicted in figure 4.3B. Accordingly, the fast relaxation channel is associated with the energetically lower S_1 band. While the slow decay channel obviously needs to be associated with the S_2 band, several possibilities for the detailed underlying relaxation mechanism are conceivable. First of all, Brown *et al.* propose that the $S_0 \rightarrow S_1$ transition originates from an intrachain excitation while the $S_0 \rightarrow S_2$ excitation is associated with an interchain exciton [256]. In this regard, two differently (de-)localized species of electron–hole pairs would be excited and the localization within one and among adjacent chains would be the origin of the two observed time-constants, respectively. However, other groups report on a significantly improved agreement between experimentally observed and theoretically modeled absorption spectra by assuming an interchain excitation in the two-dimensional lamella aggregate structure regardless of the excitation energy, i.e., the existence of

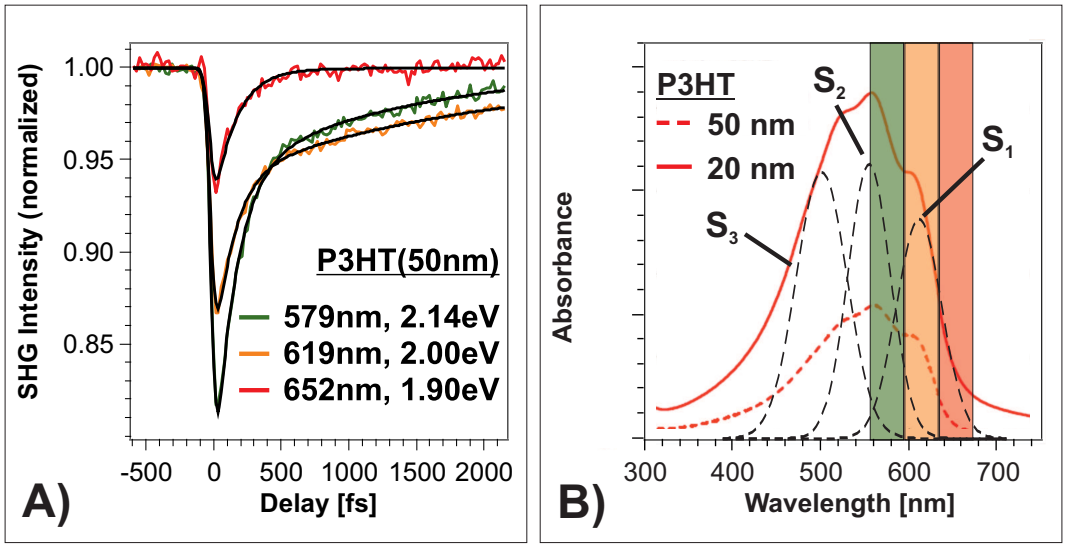

Figure 4.3. Spectroscopic TR-SHG data of pristine P3HT at varying pump beam wavelengths (A) and absorbance of the same sample (B). At 652 nm pump wavelength solely the S_1 band is populated and only the fast decay is observed ($\tau_1 = 160 \pm 50$ fs). At higher excitation energies also the S_2 band gets populated and the slow de-excitation channel is additionally observed. Black dashed lines in (B) indicate the (vibronic) absorption bands which derive from the π-stacking-mediated self-organized lamella RR-P3HT superstructure. The bars indicate the applied excitation wavelengths (colors not in accordance for presentation purposes). UV/visible measurement conducted by Marcel Schubert in the group of Prof. Dieter Neher, Universität Potsdam.

only one excitonic species [251, 257, 258]. Whether the slow decay channel needs to be associated with thermalization of excess vibronic energy (resulting from the Franck–Condon transition [251]) within the S_2 band or originates from an $S_2 \rightarrow S_1$ transition, cannot be concluded here.

For pristine C_{60} (figure 4.4) the TR-SHG signal amplitude rises during the excitation indicated by the cross-correlation shown in red. The SHG signal remains at the high level within the 20 ps time window of the measurement (cf. figure F.1, appendix F), indicating the population of a long-living excitonic state. The optically dipole allowed direct excitation of triplet excitons can be excluded as the origin of the SHG signal change due to the insufficient applied pump photon energy [39]. In contrast, Frenkel-type singlet excitonic states with nanosecond lifetimes are reported (although dipole forbidden) to be optically excitable with photon energies down to 1.57 eV [12, 39]. An alternative explanation for the observed NLO contrast accounting for the electron affinity of the acceptor molecules could be the direct excitation of 'charged

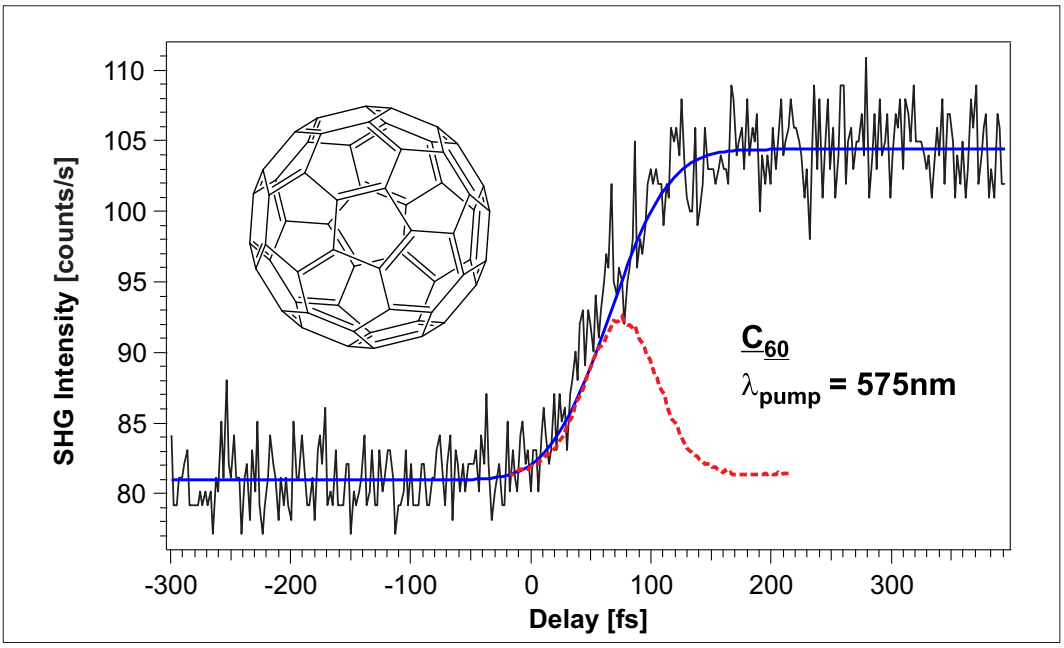

Figure 4.4. TR-SHG data of pristine C_{60}. The initial 575 nm excitation (cross-correlation shown in red) leads to an increase of the TR-SHG signal amplitude which remains constant for at least 20 ps (cf. figure F.1, appendix F). As this wavelength is insufficient for the excitation of triplet excitonic states and singlet transitions are optically dipole forbidden, the change in the NLO response is attributed to the population of long-living 'charged polarons'.

polarons' as predicted by theory [138,139] and observed in time-resolved spectroscopy [140]. An argument against the Frenkel-type singlet excitons is the expected formation of band-like states in fullerene aggregates [120] for which a change in localization on ultrafast timescales as observed for the semiconducting polymer and an according dynamic alteration of the NLO response would be expected. The 'charged polarons', however, constitute pairs of charges on adjacent molecules with a constant degree of localization and long term stability [140]. In this case, the symmetry breaking interface would be expected to give rise to an electric field enhancement of the SHG signal. Therefore, the latter assignment appears to be the more reasonable interpretation for the observed change in the SHG signal amplitude. Noticeably, the overall nonlinear response of the C_{60} sample is more than one order of magnitude smaller than for the pristine P3HT sample. On the one hand, this corresponds to the expectations as the applied visible wavelength is not absorbed by the acceptor material. On the other hand, this circumstance is also necessary for the unambiguous interpretation of the data on the D/A sample as derived in the following section.

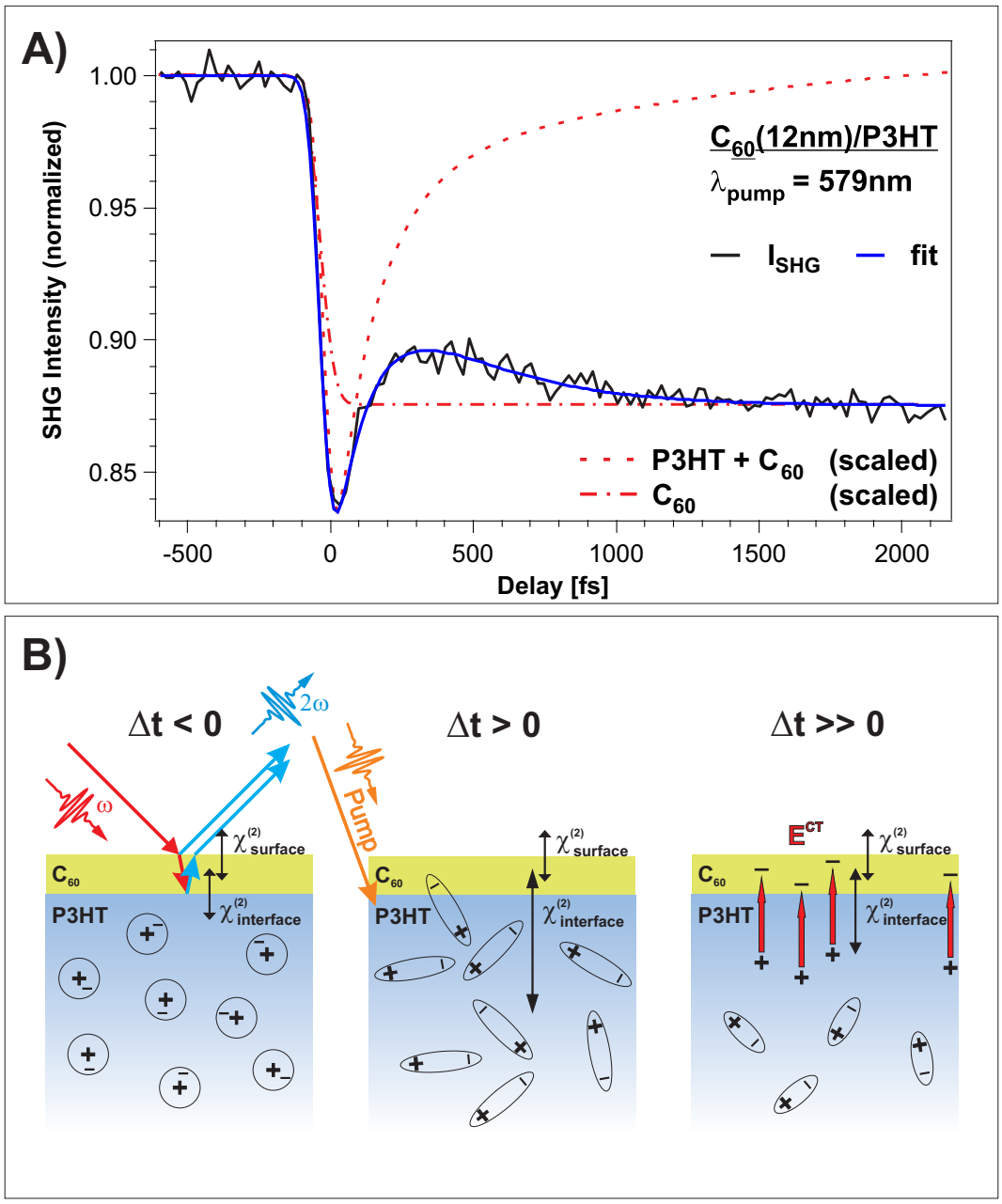

Figure 4.5. (A) The TR-SHG data of the C_{60}/P3HT sample imply an initial excitation of the donor and a subsequent time-delayed CT. The fit yields $\tau_{CT} = 320 \pm 20$ fs for the population of the intermediate state. The red dashed (sum of pristine P3HT and C_{60} data) and dash-dotted (amplitude-inverted C_{60} data) curves are guides to the eye (scaled for presentation purposes). (B) In contrast to the steady state (left), the system is initially distorted by hot, delocalized excitons (middle). At large delays these thermalize and localize. Albeit, the SHG signal gets enhanced by electric field formation resulting from CT (right).

4.4. C_{60}/P3HT Charge Transfer Dynamics

Figure 4.5A shows the TR-SHG data of the C_{60}/P3HT sample. The red dashed curve is given as a guide to the eye. It constitutes the sum of the TR-SHG data of both pristine samples (cf. figures 4.2 and 4.4) which should reflect the expected qualitative observation if the presence of the acceptor would not influence the induced dynamics in the donor and *vice versa*. While the initial signal decrease at short delays resembles the dynamics observed for pristine P3HT, the long term temporal evolution of the signal reflects a completely different behavior, as the SHG signal amplitude does not return to the initial level. It remains constant at the low level for the 50 ps time window of the measurement (cf. figure F.2, appendix F). The signal level at long delays cannot originate from a state which is directly populated by the pump beam as in the case of pristine C_{60}. This is qualitatively illustrated by the red dash-dotted line given as a guide to the eye, which is obtained by multiplying the normalized C_{60} signal by a factor of -0.5. As the topmost C_{60} layer is only 12 nm thin and the 579 nm excitation wavelength is within the optical gap of the acceptor [39], the pump beam initially predominantly excites hot, delocalized singlet excitons inside the donating P3HT layer. In the presence of the electron acceptor, an additional interface-derived de-excitation pathway besides the fast thermalization channel within P3HT exists, namely the charge transfer to C_{60}. Hence, the local maximum in the SHG signal of the D/A sample observed at a pump–probe delay of 350 fs denotes the turning point between the two non-equilibrium contributions to the SHG signal, *viz.*: (1) the decreasing distortion of the interfacial electron density by hot delocalized excitons (figure 4.5B medium panel) and (2) the field enhancement from the charge transfer across the interface (figure 4.5B right panel). The blue curve in figure 4.5A results from the iteratively convoluting fit which incorporates the thermalization of hot excitons and the delayed population of the CT state out of the initially excited singlet excitons. It yields $\tau_{\mathrm{P3HT}} = 146 \pm 8$ fs identical to the localization within P3HT and $\tau_{\mathrm{CT}} = 320 \pm 20$ fs for the population of the CT state. The latter time-constant fits well to other reported sub-picosecond population times of charge transfer states in similar systems as P3HT:PCBM [131], P3HT blends and bulk-heterojunctions with silicon [132], PCPDTBT:PCBM [118] or copper-phthalocyanine bilayers with C_{60} and C_{70} [15].

Interestingly, an additional population of the CT state delayed by several picoseconds due to exciton drift as reported by Guo *et al.* [131], is not observed here (cf. figure F.2, appendix F). Apparently the majority of the CT occurs on the ultrafast timescales prior to the hot exciton thermalization and localization. Furthermore, the picosecond decay channel assigned to either the thermalization and localization within the S_2 band or the $S_2 \rightarrow S_1$ interband

relaxation observed for the pristine P3HT sample, is apparently not competitive to the CT channel. This finding allows for the important conclusion that a strong coupling between the S_2 band and the CT state exists, which could be exploitable to increase the charge transfer yield by providing excess excitation energy, as elucidated in the subsequent section.

4.5. C_{60}/P3HT Charge Transfer Yield

As outlined in the experimental section, the amount of transferred charge is approximately proportional to the change in the SHG signal level at large delays [13]:

$$\Delta I_{\mathrm{CT}} \approx \eta \cdot I^2(\omega) E^{\mathrm{DC}}, \tag{4.1}$$

where the proportionality factor η contains the dependence on the dielectric function [259, 260] and the nonlinear susceptibility, $I(\omega)$ is the probe beam intensity and $E^{\mathrm{DC}} \propto Q^{\mathrm{CT}}$ is the interfacial electric field which is related to the transferred charge in the approximation of a parallel plate capacitor. Accordingly, the correlation between the CT yield and the excess excitation energy can be elucidated by measuring the SHG signal amplitude change $\Delta I_{\mathrm{CT}}(\lambda)$ at large delays as a function of the pump photon energy. However, as the absorbance of the donor also depends on the excitation wavelength, $\Delta I_{\mathrm{CT}}(\lambda)$ needs to be normalized to the number of initially excited electron–hole pairs. In the case of sufficiently low excitation densities to avoid undesired effects as exciton–exciton annihilation [156–158] or even thermally induced absorbance shifts [159] (and for small initial TR-SHG signal amplitude changes $\Delta I_0(\lambda)$ in comparison to the steady state signal level cf. equation 2.8), $\Delta I_0(\lambda)$ is proportional to the initial exciton population. That this is indeed the case for the conducted experiments is shown in figure 4.6. Both, the SHG signal changes at large and short delays $\Delta I_{\mathrm{CT}}(\lambda)$ and $\Delta I_0(\lambda)$, respectively, scale linearly with the pump beam intensity. If the excitons would act as quenchers for each other, the SHG signal changes as a function of the pump intensity would increasingly saturate. Therefore, $\Delta I_{\mathrm{CT}}(\lambda)/\Delta I_0(\lambda)$ is constant as a function of the pump power (figure 4.6B blue curve) while as a function of the excitation wavelength, this term constitutes a measure for the CT yield.

In a next step, the photon energy of the pump beam is varied to excite the polymer energetically above (576 nm), in overlap with (618 nm) and below (652 nm) the $S_0 \rightarrow S_1$ absorption maximum at 610 nm (cf. figure 4.3B). Figure 4.7A shows the spectroscopic TR-SHG data of the C_{60}/P3HT sample. The dynamics induced by the intermediate pump photon energy are identical ($\tau_{\mathrm{P3HT}} = 146 \pm 7$ fs, $\tau_{\mathrm{CT}} = 320 \pm 20$ fs) as for the 579 nm excitation. For the 652 nm excitation the charge transfer is slightly faster ($\tau_{\mathrm{P3HT}} = 154 \pm 26$ fs,

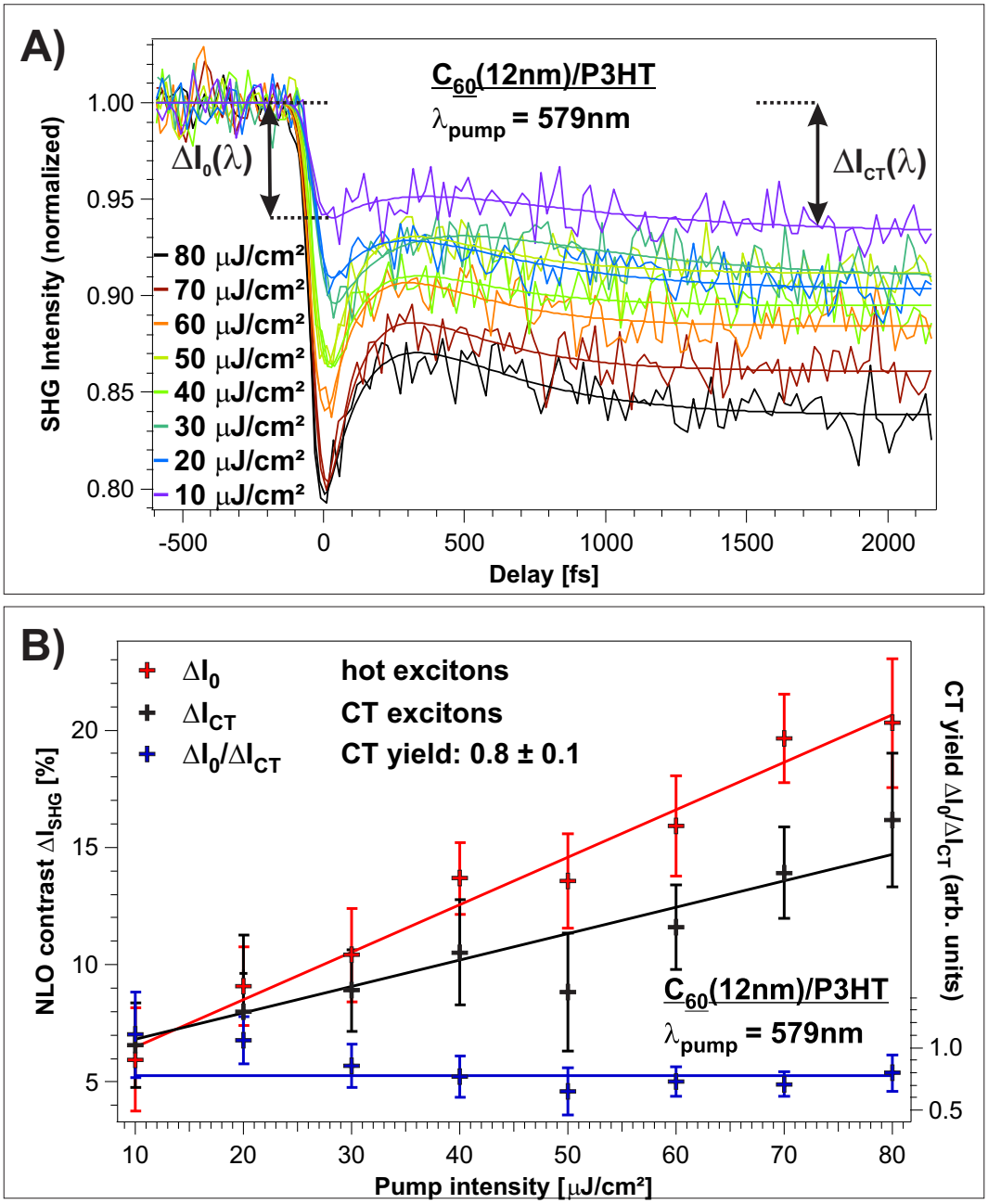

Figure 4.6. (A) TR-SHG data for the C_{60}/P3HT sample measured for varying excitation powers between 10 μJ/cm^2 and 80 μJ/cm^2. (B) The measured SHG signal contrasts at short and large delays ΔI_0 (red) and ΔI_{CT} (black), respectively, scale linearly with the excitation power and $\Delta I_{CT}/\Delta I_0$ (blue) therefore constitutes a measure for the relative amount of transferred charge. The minor observed offsets result from the direct excitation of the acceptor layer as discussed in appendix G.

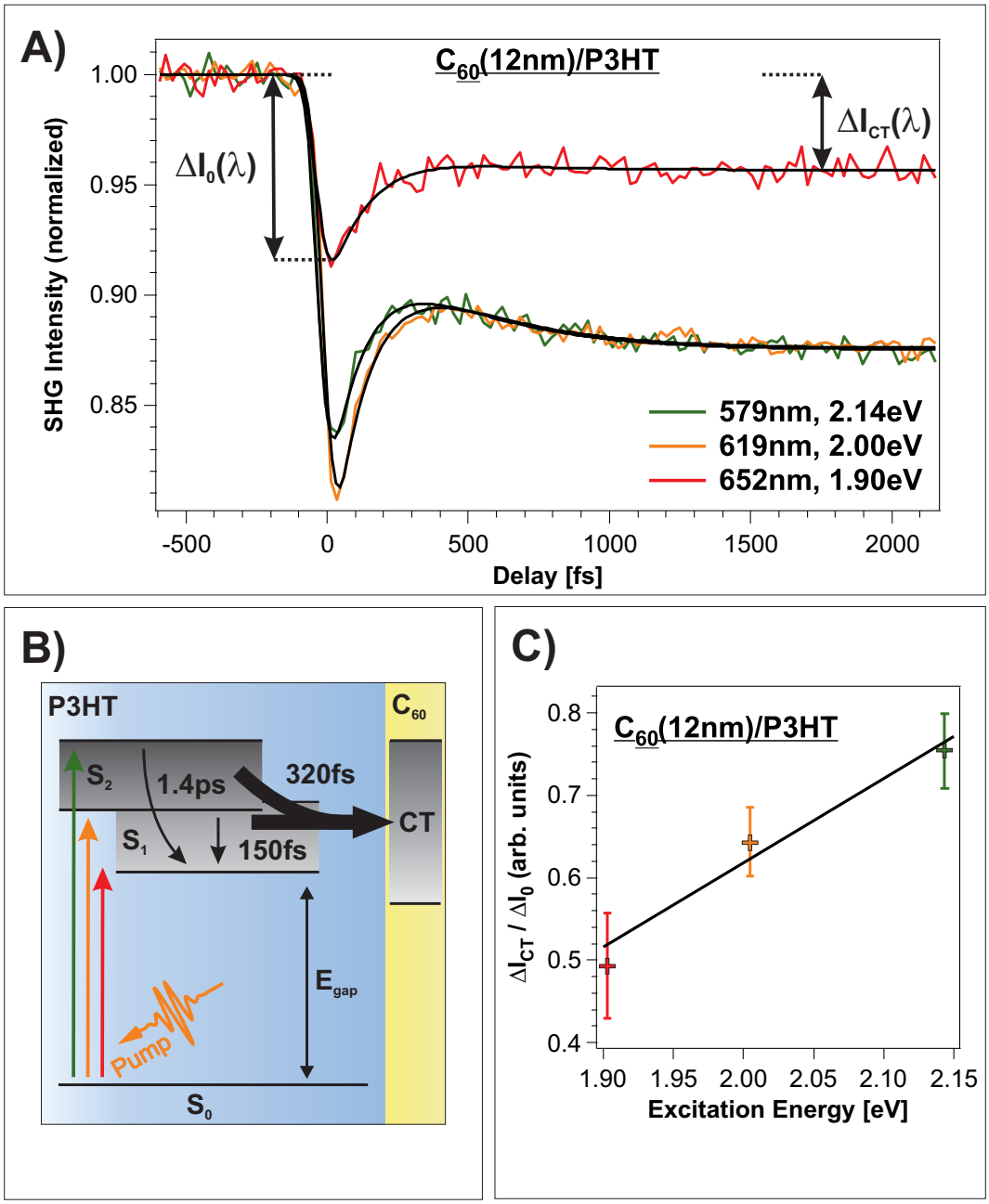

Figure 4.7. (A) The TR-SHG data on the C_{60}/P3HT sample measured for different excitation wavelengths allow for two conclusions. First, as depicted in (B), the CT state gets populated out of the S_1 band of the polymer and the process is enhanced if the excitation energy is sufficient to involve the S_2 band in addition. Second, the CT yield $\Delta I_{\mathrm{CT}}(\lambda)/\Delta I_0(\lambda)$ correlates with the excitation wavelength. It increases by approximately 50 % when the pump photon energy is increased from 1.90 eV to 2.14 eV as shown in (C).

$\tau_{CT} = 249 \pm 66$ fs). From these results two important observations can be derived. First, the charge transfer is also operative upon the 652 nm excitation although the S_2 band of the polymer is not populated. In conjunction with the above finding of the direct, ultrafast CT population out of the S_2 band for higher excitation energies, the according conclusion is depicted in figure 4.7B: the CT state gets populated out of the S_1 band of the polymer and the process is enhanced when the excess excitation energy is sufficient to populate the S_2 band in addition. Second, this results in an increased CT yield as a function of the excitation wavelength as shown in figure 4.7C. The charge transfer yield increases by approximately 50 % when the pump photon energy is altered from 1.90 eV to 2.14 eV. These numbers do not only confirm the qualitatively evident competition between energetic relaxation and localization of hot excitons and the charge transfer (cf. figure 4.5). They also show that the balance between these two channels progressively shifts in favor of the CT state population with increasing excess energy at the higher energetic excitations.

4.6. Summary: Exciton Dynamics

In summary, the intrinsic interface sensitivity of time-resolved SHG has been utilized to investigate the photoinduced charge transfer dynamics at the C_{60}/P3HT heterojunction. Induced dynamic changes in the interfacial electron density were indeed found to be traceable due to: (a) the influence of hot, delocalized excitons initially excited in the polymer on the susceptibility of the surrounding materials and (b) the electric field enhancement of the TR-SHG signal arising from the charge transfer across the D/A interface. In this regard, spectroscopic SHG measurements conducted by varying the pump photon energy enabled the identification of the donor- and interface-derived electronic states involved in the charge transfer process. In addition, polarization-resolved SHG provided the suitable means for investigating the quality of the interfaces of solution processed and vacuum evaporation deposited organic thin films and layered structures.

Two ultrafast decay channels of initially excited hot singlet excitons in pristine P3HT were observed and attributed to their energetic de-excitation and corresponding localization within the S_1 and S_2 bands of the polymer. In the presence of the acceptor, the ultrafast population of an interface-derived CT state is identified. Based on spectroscopic TR-SHG data, obtained by varying the pump beam wavelength, two important results on the charge transfer dynamics were derived. (1) The CT state gets populate out of the lower energetic S_1 band of the polymer and the process is enhanced if the excess excitation energy is sufficient to populate the S_2 band in addition. (2) Most remarkably, in a quantitative analysis of the amounts of generated singlet excitons and transferred charges to which the SHG amplitudes at different delays are

approximately proportional, respectively, a correlation between the CT yield and the excitation wavelength has been derived. It increases by approximately 50 % when the pump photon energy is altered from 1.90 eV to 2.14 eV.

It has to be kept in mind, however, that an increased charge transfer yield does not necessarily result in an increased charge generation yield, as for example proposed by Grancini *et al.* [118]. Recent studies revealed no correlation between the excitation energy and the quantum yield for charge separation in a variety of OPV model systems [121,122]. However, an increased performance of OPVs might be achievable by realizing both, a high CT yield out of a hot exciton population as demonstrated here and an efficient charge separation. While the former clearly indicates toward an advantage of low bandgap polymers [242,261,262] aside from considerations regarding the Shockley-Queisser-limit [14,116], the latter should be subject to further investigations.

As demonstrated here for the D/A interface, investigating the dynamics within the functional layers of an OPV first individually and subsequently at the pairwise interfaces leads to a stepwise understanding of each layer's contribution to the overall system functionality. Isolating the individual steps in the light-to-current conversion process hence provides a decisive advantage in comparison to the often practiced investigation of the properties of complete devices as for example the direct measurement of the voltage–current characteristics. The approach therefore holds the key to an understanding of the underlying processes in organic photovoltaics and accordingly for an improvement of device performance.

In a next step, aside from incorporating the above mentioned low bandgap polymers [242,261,262], the influence of transparent conducting oxide (TCO) top and metallic bottom electrodes like tin-doped indium oxide (ITO) [263] and gold, respectively, could be the subject to further investigations. Moreover, the need for additional interfacing layers could be studied which are considered to optimize the OPV performance [264]. For instance the transparent polymer blend poly(3,4-ethylenedioxythiophene):poly(styrene sulfonate) (PEDOT:PSS) [265] could be investigated, which is known to flatten out imperfections in the ITO surface and to prevent separated electrons from reaching the top electrode. Another example is 2,9-dimethyl-4,7-diphenyl-1,10-phenanthroline (BCP) which is analogously incorporated to screen the cathode against free holes [266].

Chapter 5

Conclusion

Second Harmonic Generation

In the framework of this thesis, an experimental SHG setup has been developed and realized. The inherent interface sensitivity of this experimental probe has been utilized to investigate functionalized surfaces and functional thin layers, *viz.* photochromic azobenzene and fulgimide self-assembled monolayers and the C_{60}/P3HT heterojunction. In each case, light has been applied as an external stimulus to trigger electronic excitations and charge rearrangements in the respective systems which are subsequently monitored *via* the change in the second order non-linear susceptibility tensor $\chi^{(2)}$ to which the SHG probe is sensitive. For the photochromic interfaces, these were static changes in the degree of the conjugation and the orientation of the π-electron system induced by visible and UV cw-light illumination. These resulted in pronounced changes of the NLO responses when switching between the respective photostationary states. In case of the donor/acceptor heterojunction, ultrafast exciton and charge transfer dynamics on a femtosecond timescale were induced and observed by means of time-resolved SHG experiments. Regarding the latter, additional information was obtainable by varying the pump beam wavelength, i.e., by conducting spectroscopic SHG measurements. In each case, polarization-resolved SHG has proven particularly useful to obtain geometric information, concretely on molecular alignment and accordingly the orientation of the non-linear susceptibility and on the interfacial smoothness, respectively. In summary, the SHG setup has proven to be a versatile experimental probe, capable of resolving induced changes in the interfacial electron density with both, a sub-monolayer molecular sensitivity and a temporal resolution below 50 fs.

Photochromic Interfaces

Despite the obvious differences between the two investigated chromophores azobenzene and the indolyl-fulgimide, the observed characteristic NLO responses of the respective photochromic interfaces are surprisingly comparable. The NLO contrasts of 19 ± 3 % for the *trans* $\leftrightarrow$ *cis* isomerization of

the former and 17 ± 5 % for the ring-opening/ring-closure reaction of the latter are equal within the given error bars and the respective cross-sections of $\sigma_{\mathrm{vis}} = 3.1 \pm 0.2 \cdot 10^{-18}$ cm^2 and $\sigma_{\mathrm{UV}} = 0.7 \pm 0.1 \cdot 10^{-18}$ cm^2 as well as $\sigma_{\mathrm{vis}} = 1.2 \pm 0.3 \cdot 10^{-18}$ cm^2 and $\sigma_{\mathrm{UV}} = 2.3 \pm 0.3 \cdot 10^{-18}$ cm^2 are on the same order of magnitude. Taken together, in particular accompanied by the complete reversibility observed in 19 switching steps in both cases, these findings imply an efficient decoupling between the chromophores and the respective substrates. In addition, when comparing these cross-sections to the four orders of magnitude smaller value for TBA/Au(111) on the one hand and to the equally efficient isomerization of azobenzene SAMs with significantly larger adamantane core or TATA linker systems on the other hand, it is tempting to conclude on an unhindered isomerization triggered by an intramolecular excitation in both cases. Albeit, additional investigations on a correlation between the azobenzene chromophore packing density, i.e., on the NLO contrast as a function of the ratio between azobenzene-functionalized alkyl chains and unmodified linkers, reveal a progressing quenching probably due to excitonic coupling or steric hindrance already at intermediate coverages.

As demonstrated for the fulgimide SAM, supporting theoretical investigations in the form of density functional theory as well as correlated wavefunction method calculations in the present case performed by Manuel Utecht in the group of Prof. Peter Saalfrank at the Institut für Chemie at the Universität Potsdam, provide a powerful tool in interpreting and confirming experimentally obtained information on NLO properties of the photochromic interfaces. In particular, the theoretical results allowed to conclude on the molecular alignment. (1) The interruption in the electronic conjugation of the four-ring π-system of the C-fulgimide in the ring-opening reaction due to the torsion between the indole and imide planes for the open isomers has been found to result in a significant difference in the hyperpolarizabilities which nicely explains the pronounced NLO contrast between the respective PSSs. (2) The alignment of the chromophores is predominantly parallel to the surface normal and the NLO contrast therefore applies perpendicular to the photochromic interface.

For the azobenzene SAMs, polarization-resolved SHG measurements provided evidence for the assumed origin of the NLO contrast. It arises from the 'geometric' rearrangement of the π-electron system and the according reduction in the degree of electronic conjugation perpendicular to the interface in the *trans* $\rightarrow$ *cis* isomerization. The second order non-linear susceptibility perpendicular to the surface is two orders of magnitude larger than parallel to the interface and it significantly decreases when the beforehand interface-averted 'upper' phenyl-ring is bent into plane, while the parallel component increases in this *trans* $\rightarrow$ *cis* isomerization. Additional detailed information on the chromophore alignment is obtainable, by comparing the polarization-resolved SHG data on the second order non-linear susceptibility as a system

property to the azobenzene molecular hyperpolarizabilities accessible in theoretical calculations as analogously done for the fulgimide SAMs. The latter is currently in progress.

The thermal stability at room temperature found for both systems, is partially astonishing. While the here investigated fulgimide is known to posses a sufficiently large thermal activation barrier to avoid thermal back-reactions, the *cis*-isomer of azobenzene is in general meta-stable with a thermal activation barrier which strongly depends on the environment, i.e., the solvent or the substrate. As it appears, the azobenzene SAM is thermally stable at room temperature solely if a sufficient amount of water is available *viz.* at high humidity. A complete back-reaction in a protective nitrogen atmosphere has been observed as well as a partial destabilization of the *cis*-PSS into a thermally stable intermediate state which contains an approximately equal ratio of *trans*- and *cis*-isomers, respectively, in air at low humidity. This apparent increase of the barrier for a thermal back-reaction and according stabilization of the *cis*-isomer *via* water co-adsorption demands for a further investigation for example by means of targeted water deposition in an UHV chamber. Furthermore, the aforementioned temperature-controlled SHG measurements *via* incorporation of a Peltier-element constitute an intriguing next step in this regard.

The major remaining challenge regarding the here investigated photochromic interfaces en route towards innovative photonic and optoelectronic data processing and transmitting microelectronic components and data storage devices, is a further improvement of the already substantial respective NLO contrasts. This might be achievable by adding an intermediate layer with low second order non-linear susceptibility between the linker-chains and the functional head-group, as for the azobenzene SAMs a significant background contribution from the alkyl chains has been observed. For the fulgimides, a further enhancement of the NLO contrast might be achievable by chemically modifying the electronic structure of the chromophore. The two possible improvements in this regard are: (a) an increased difference in the first hyperpolarizabilities between the E- and the C-fulgimide as a molecular parameter and (b) an increased difference in the interfacial second order non-linear susceptibility as a system parameter, by suppressing the undesired E $\rightarrow$ Z reaction which reduces the E $\rightarrow$ C yield.

Ultrafast Charge Transfer Processes

By investigating prototypal materials for organic solar cells, namely the organic semiconductor P3HT and the electron acceptor C_{60}, this work aimed to contribute to the fundamental understanding of the ultrafast charge transfer across the D/A interface. The combination of the intrinsic interface sensitivity with

the femtosecond temporal resolution inherent to the SHG setup developed and realized in the framework of this thesis, has proven particularly useful for the investigation of the photoinduced charge transfer dynamics at the C_{60}/P3HT heterojunction. Induced dynamic changes in the interfacial electron density were indeed found to be traceable due to: (1) the influence of hot, delocalized excitons initially excited in the polymer on the susceptibility of the surrounding molecules and (2) the electric field enhancement of the TR-SHG signal arising from the charge transfer across the D/A interface. In this regard, spectroscopic SHG measurements conducted by varying the pump photon energy enabled the identification of the donor- and interface-derived electronic states involved in the charge transfer process. In addition, polarization-resolved SHG provided the suitable means for investigating the quality of the interfaces of solution processed and vacuum evaporation deposited organic thin films and layered structures.

The choice for the C_{60}/P3HT heterojunction instead of the commonly used P3HT:PCBM blend, reduced the complexity of the system to a single, well-defined interface. The photoinduced dynamics at the D/A interface of this model system can be expected to be very similar to those in P3HT:PCBM blends in which phase-separation results in the formation of donor and acceptor domains. Regarding the charge transfer dynamics, the interface of the model heterojunction investigated in the framework of this thesis thus corresponds to the domain boundaries in the blended materials.

The first step in developing an understanding of the dynamics at the investigated D/A interface was to study the pristine P3HT and C_{60} samples. For the donor, a pronounced pump-induced change in the TR-SHG signal amplitude was observed to return to the initial level within $\tau_1 = 154 \pm 6$ fs and $\tau_2 = 1370 \pm 80$ fs. Considering experimental and theoretical reports on the influence of excess charges and unscreened dipoles on the non-linear susceptibility of surrounding molecules on the one hand and the high degree of delocalization of hot excitons on the other hand, the observed TR-SHG signal evolution is assigned to originate from the initial excitation and subsequent thermalization and corresponding localization of hot singlet excitons. Interestingly, the de-excitation was found to exhibit a bi-exponential behavior. By varying the pump beam wavelength, the involvement of two polymer-derived bands S_1 and the energetically higher S_2 was deduced. In contrast, the pump-induced TR-SHG signal amplitude change observed for pristine C_{60} was found to remain constant within the 20 ps time window of the measurement. It was assigned to originate from the excitation of 'charged polarons', i.e., long-living excitonic states, localized at adjacent fullerene molecules.

The TR-SHG data of the D/A sample resemble the dynamics observed for pristine P3HT for short delays up to 350 fs which indicates the initial population and the onset of localization of hot excitons in the donor layer. Thereafter,

the signal amplitude was found to decrease again instead of proceeding to return to the initial level. These dynamics indicate the delayed population of an interface derived state out of the initial hot exciton population. In accordance, the pronounced TR-SHG contrast at large delays is attributed to a field enhancement induced by charge transfer. Interestingly, solely the thermalization channel associated with the S_1 band is still operative for the D/A sample, while the ultrafast forming CT state appears to be directly populated out of the energetically higher S_2 band prior to de-excitation. Additional spectroscopic TR-SHG measurements conducted by varying the excitation wavelength revealed that a charge transfer out of the S_1 band is also operative. However, the process gets significantly enhanced if sufficient excess excitation energy is available, to additionally involve the S_2 band. Most remarkably, the CT yield was found to correlate with the excitation wavelength. It increases by approximately 50 % when the pump photon energy is altered from 1.90 eV to 2.14 eV.

It has to be kept in mind that an increased charge transfer yield does not necessarily result in an increased charge generation yield. Furthermore, recent studies revealed no correlation between the excitation energy and the quantum yield for charge separation in a variety of OPV model systems. Nevertheless, an increased performance of OPVs might be achievable by realizing both, a high CT yield out of a hot exciton population as has been demonstrated here and an efficient charge separation. While the former clearly indicates toward an advantage of low bandgap polymers aside from considerations regarding the Shockley-Queisser-limit, the latter should be subject to further investigations.

As has been shown in the framework of this thesis for the C_{60}/P3HT heterojunction, investigating the dynamics within the functional layers of an OPV first individually and subsequently at the pairwise interfaces leads to a stepwise understanding of each layer's contribution to the overall device functionality. Isolating the individual steps in the light-to-current conversion process hence provides a decisive advantage in comparison to the often practiced investigation of the properties of complete devices as for example the direct measurement of the voltage–current characteristics. The approach therefore holds the key to an understanding of the underlying processes in organic photovoltaics and accordingly for an improvement of device performances.

Regarding the corresponding continuation of the here presented experimental work, utilizing the inherent interface sensitivity and the femtosecond temporal resolution of the TR-SHG setup developed and realized in the framework of this thesis, two intriguing next steps are feasible. First, low bandgap polymers should be investigated with regard to the charge transfer yield as a function of the excitation wavelength. Second, more complicated layered structures could be investigated, for instance incorporating TCO top and metallic bottom electrodes like ITO and gold, respectively, or materials as PEDOT:PSS or

BCP, known to flatten out certain film imperfections and to prevent separated electrons and holes from reaching the top and bottom electrode, respectively.

Appendix A

Abbreviations

2PPE	two-photon photoelectron spectroscopy
AES	Auger electron spectroscopy
ATR	attenuated total reflection
BBO	β-Bariumborat
C	closed/colored-fulgimide
c.c.	complex conjugated
CS	charge separation
CT	charge transfer
D/A	donor/acceptor
DC	direct current
DFG	difference frequency generation
E	*trans*-fulgimide
EFISH	electric field enhanced second harmonic generation
EOR	electro-optical rectification
EQE	external quantum efficiency
FWHM	full width at half maximum
GaAs	gallium arsenide
HOMO	highest occupied molecular orbital
HPLC	high performance liquid chromatography
HREELS	high resolution electron energy loss spectroscopy
IPV	inorganic photovoltaic device
ITO	tin-doped indium oxide
KDP	potassium dihydrogen phosphate
Nd:YAG	neodymium-doped yttrium aluminium garnet
NEXAFS	near edge x-ray absorption fine structure spectroscopy
NIR	negative ion resonance
NIXSW	normal incidence x-ray standing wave
NLO	non-linear optical
OPV	organic photovoltaic device
P3HT	poly(3-hexylthiophene)
PCBM	phenyl-C_{61}-butyric acid methyl ester
PEDOT:PSS	poly(3,4-ethylenedioxythiophene):poly(styrenesulfonate)

PIR	positive ion resonance
PL	photoluminescence spectroscopy
PPV	polyphenylene vinylene
PSS	photostationary state
RR	regioregular
RRa	regiorandom
SAM	self-assembled monolayer
SF	singlet fission
SFG	sum frequency generation
SHG	second harmonic generation
STM	scanning tunneling microscopy
STS	scanning tunneling spectroscopy
TA	transient absorption spectroscopy
TATA	triazatriangulenium
TCO	transparent conducting oxide
TBA	3,3',5,5'-tetra-*tert*-butyl-azobenzene
TTL	transistor–transistor logic
UHV	ultra high vacuum
UV	ultraviolet
XPS	x-ray photoelectron spectroscopy
Z	*cis*-fulgimide

Appendix B

Technical Drawings

Figures B.1, B.2 and B.3 show the technical drawings of the chamber parts 'wall A' and 'wall B', 'wall C' and 'wall D' as well as 'top' and 'bottom', respectively.

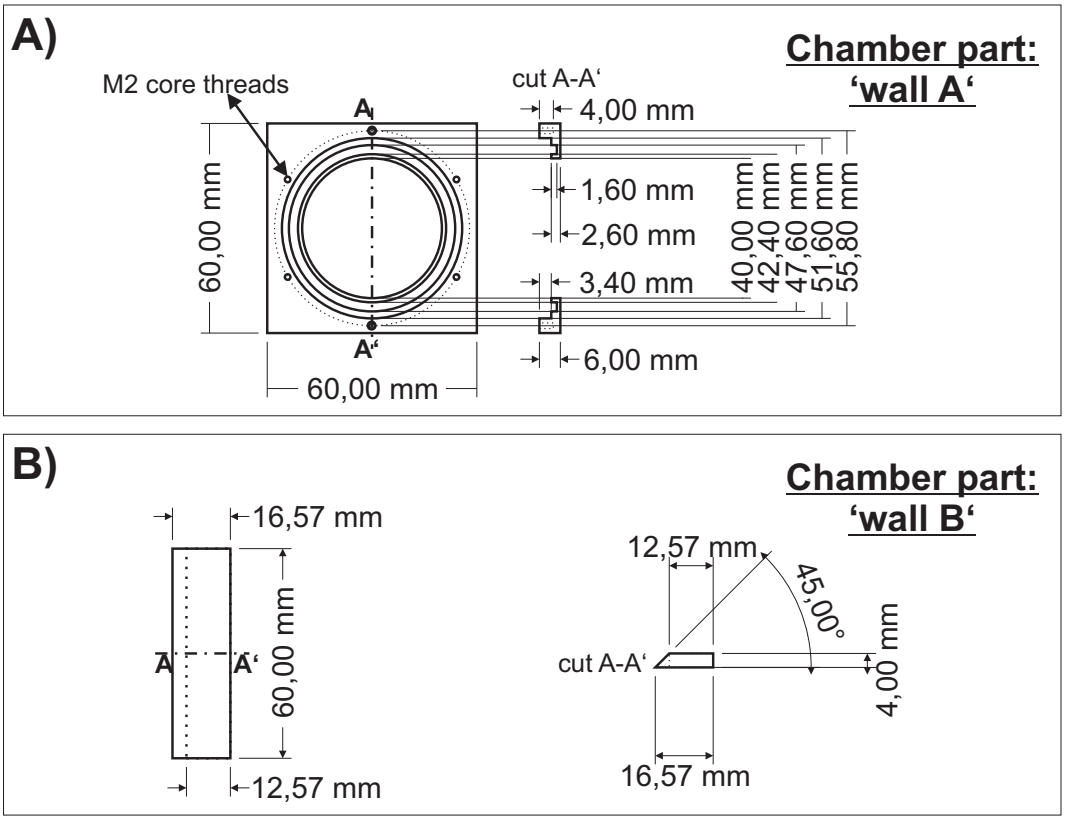

Figure B.1. Technical drawings of the experimental chamber parts 'wall A' (A) and 'wall B' (B).

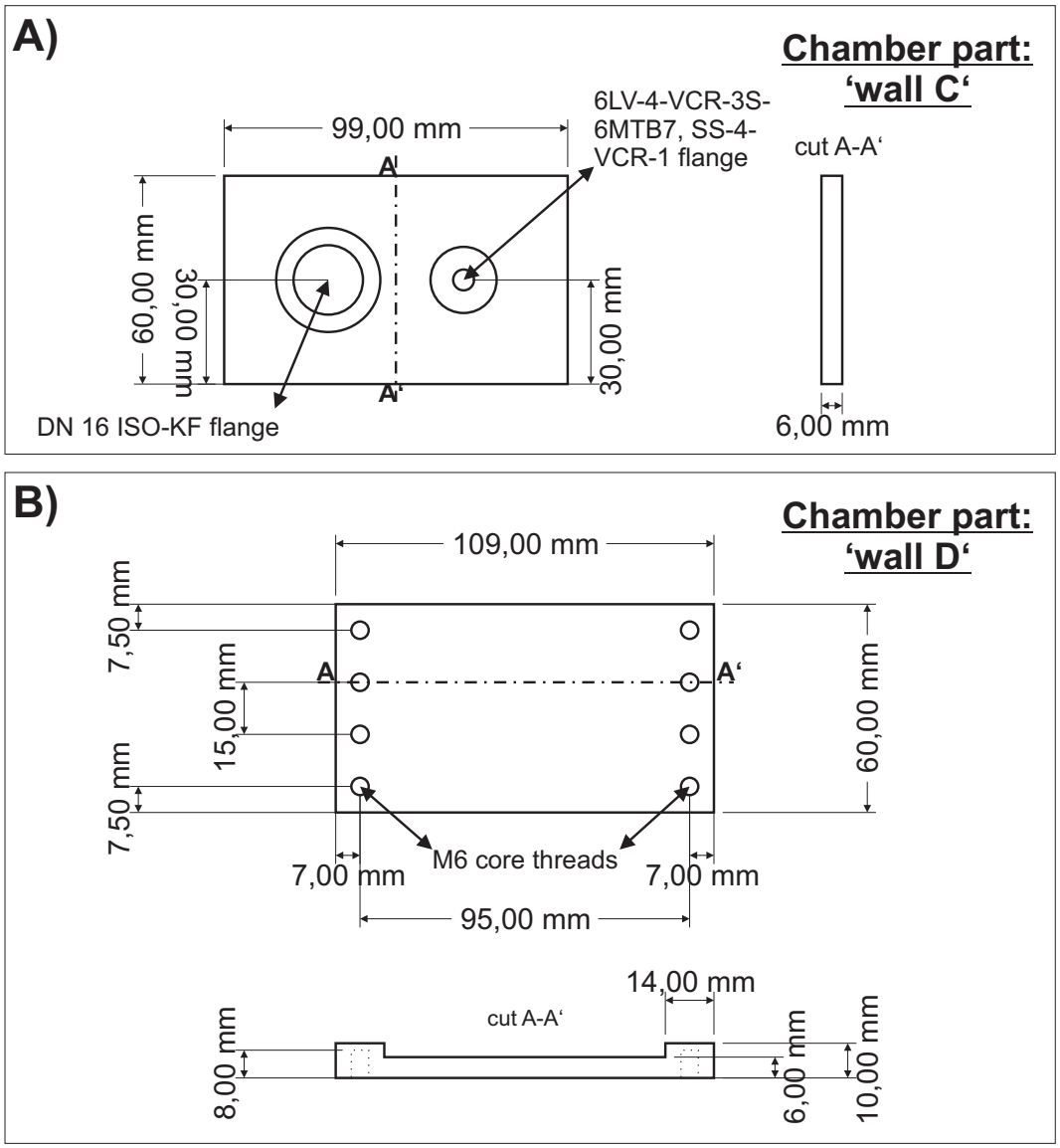

Figure B.2. Technical drawings of the experimental chamber parts 'wall C' (A) and 'wall D' (B).

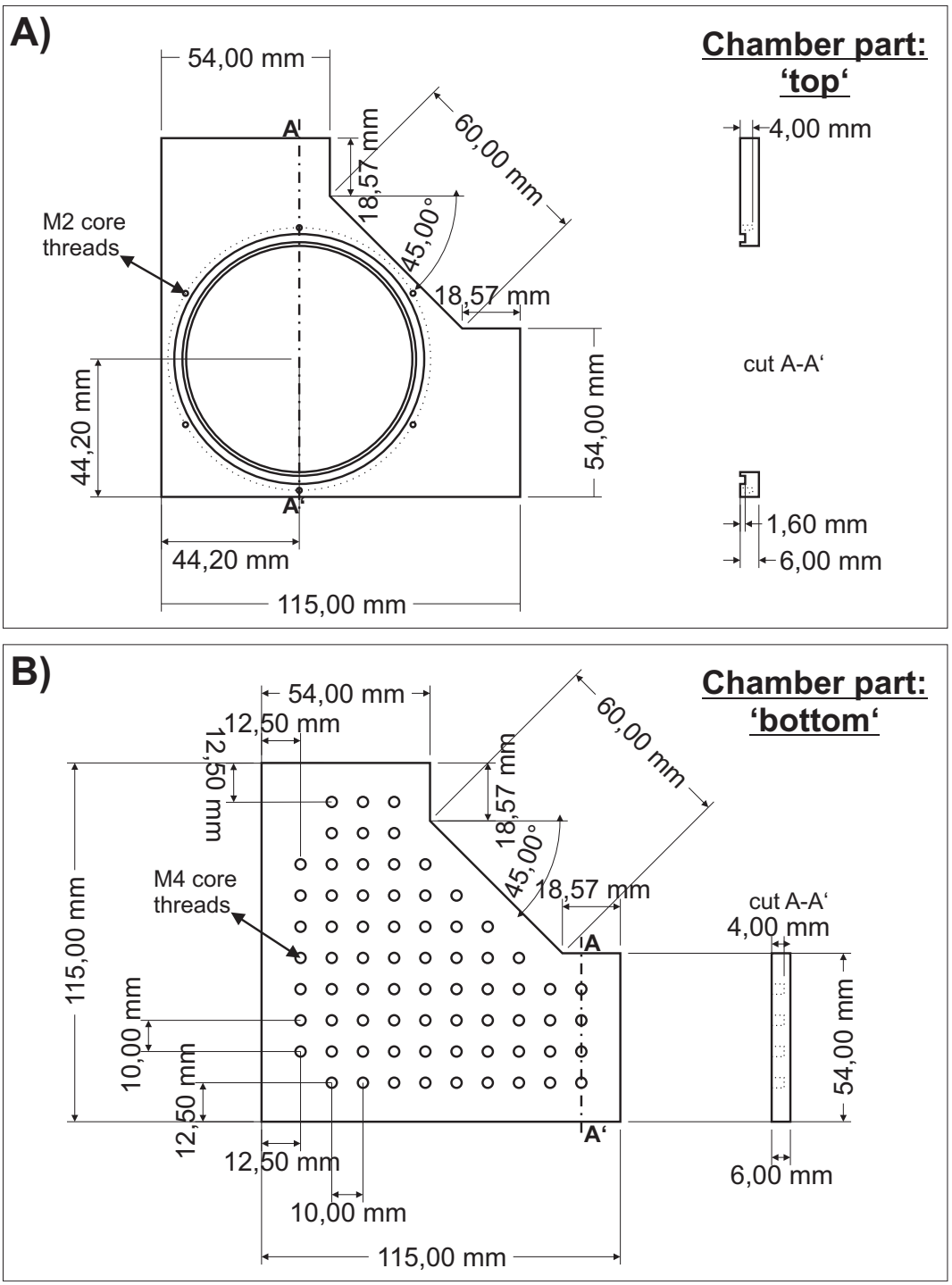

Figure B.3. Technical drawings of the experimental chamber parts 'top' and 'bottom'.

Appendix C

Fulgimide SAM: Background Correction

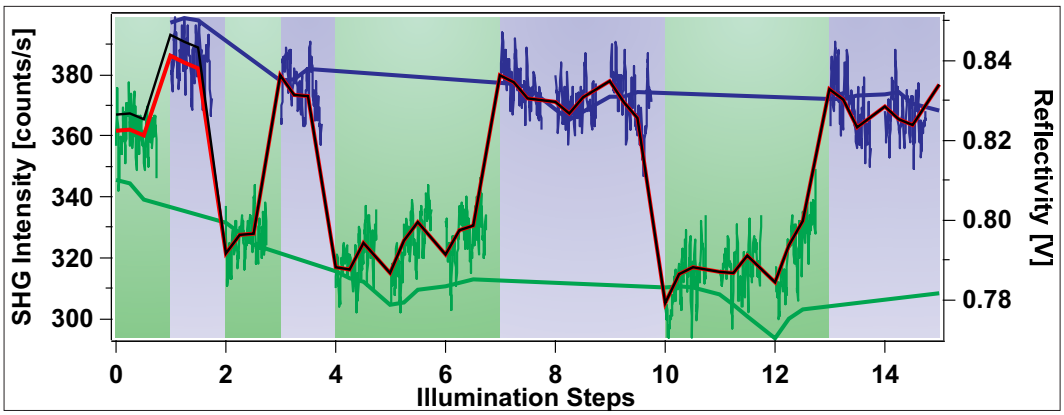

Figure C.1. The linear reflectivity of the sample is recorded during the measurement. The resulting blue and green solid lines yield a reduction in the laser stability of 1.5 %. As the linear reflectivity is considerably less sensitive to the interface in comparison to the second order non-linear SHG process, the decrease in reflectivity is attributed to a loss in laser power. The red solid line illustrates the correspondingly corrected data. The blue line is offset by 0.05 V for illustration purposes.

The linear reflectivity of the fulgimide SAM measured by means of the photodiode behind the dichroic mirror decreases during the measurement by 1.5 %. As mentioned in the experimental chapter, the linear reflectivity is considerably less sensitive to the interface in comparison to the second order non-linear SHG process. The observed signal intensity loss is accordingly attributed to a loss in laser stability which is usually on this order of magnitude during the period of a day. A background subtraction corresponding to the reduction in reflectivity is therefore performed, as depicted in figure C.1.

Appendix D

Azobenzene SAMs: Initial Ratio of *trans*-Azobenzene

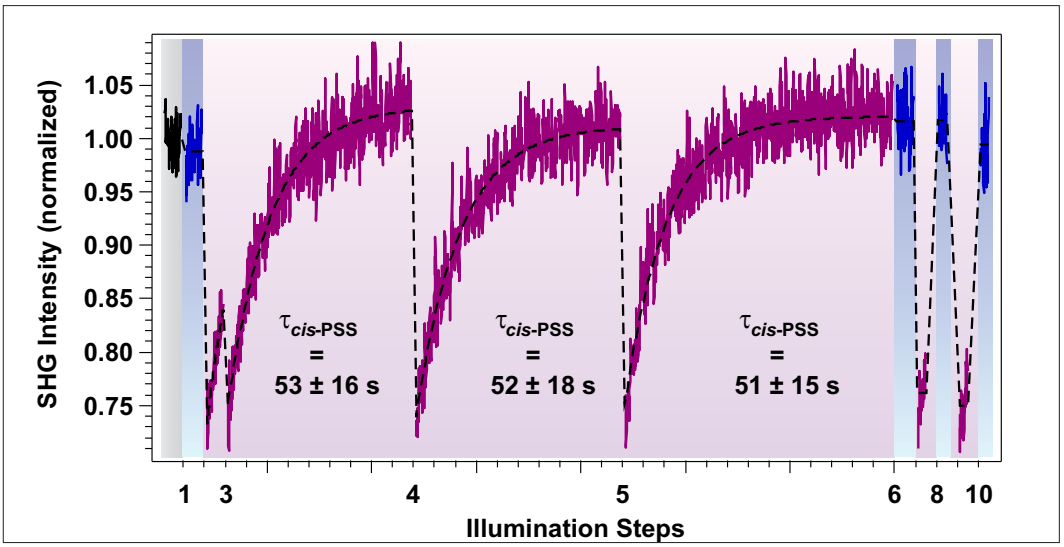

Figure D.1. SHG intensity measured for the 75 % azobenzene SAM as a function of illumination steps. Data labeled in purple and blue denote measurements conducted subsequent to UV (365 nm, photon dose $n_{\mathrm{UV}} = 1.3 \cdot 10^{20}$ cm^{-2}) and visible (445 nm, $n_{\mathrm{vis}} = 4.4 \cdot 10^{19}$ cm^{-2}) light illumination, respectively. The black curve is obtained for the initial SHG measurement prior to UV light exposure. Data are normalized to the amplitude of the latter for comparability. The initial SHG intensity is equal to the signal level associated with the *trans*-PSS within the given experimental accuracy. As these measurements are conducted under a protective gas (N_2, purity '5.0') atmosphere, the *cis*-PSS is thermally unstable at room temperature (cf. section 3.3.5).

The samples are prepared under exclusion of UV light and should therefore solely contain azobenzene chromophores immobilized in their thermally favorable *trans*-form [201, 204] prior to the illumination experiments. Accordingly, a

comparison of the initial SHG signal amplitude prior to any light exposure and the average *trans*-PSS signal level, allows to estimate the isomer ratio in the *trans*-PSS. The prerequisite is the validity of the approximate proportionality of the isomerization-induced SHG signal amplitude change and the number of switched chromophores (equation 2.8). As depicted in figure D.1, the respective signal levels are equal within the given experimental accuracy. The upper limit of the fraction of *cis*-isomers in the *trans*-PSS is thus estimated not to be higher than approximately 20 %. Note that these measurements are conducted under a protective gas (nitrogen, purity '5.0') atmosphere. The *cis*-PSS is therfore thermally not stable at room temperature, as discussed in detail in section 3.3.5.

Appendix E

C_{60}/P3HT: Well-Defined Interfaces

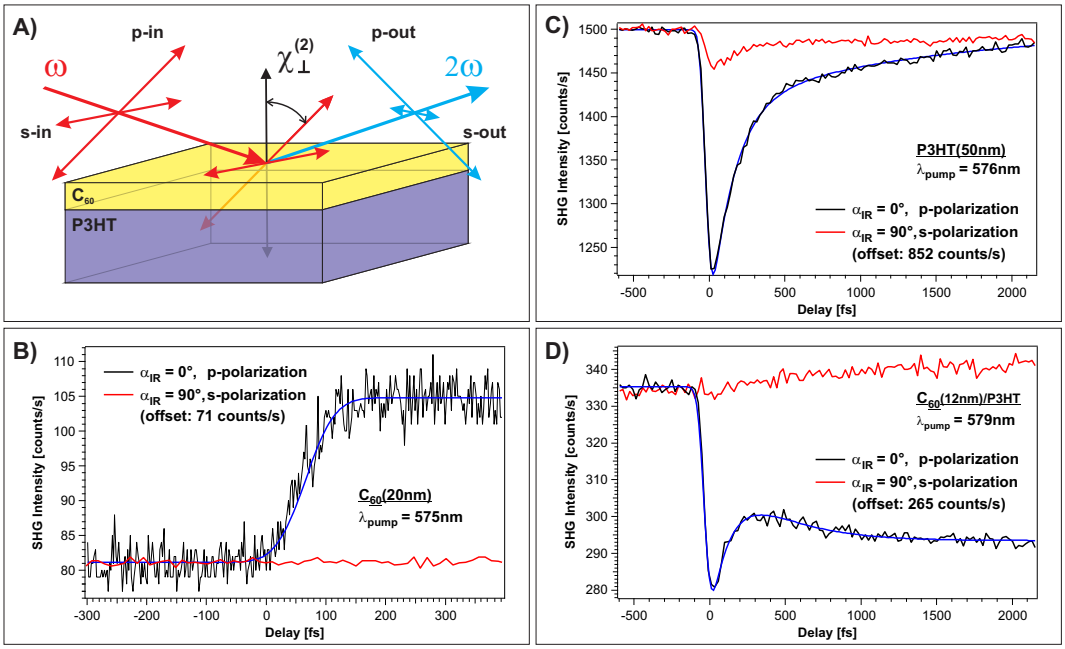

Figure E.1. (A) While the electric field of the p-polarized probe beam has a component perpendicular to the surface and therefore samples the components of the second order non-linear susceptibility tensor $\chi^{(2)}$ in that direction, an s-polarized probe beam is 'unaware' of the presence of an ideally flat surface (for simplicity only the response of one interface is illustrated). (B-D) For each sample the overall SHG signal amplitudes measured in s-polarization are small and the TR-SHG signal changes at time zero are neglectable compared to the data measured for the p-polarized probe beam, indicating homogeneous samples and well-defined interfaces. SHG data measured in s-polarization are offset by the stated respective count rates for comparability.

The success of the preparation strategy is justified *via* polarization-resolved

SHG measurements sensitive to interfacial roughness. Figure E.1A illustrates how the intrinsic interface sensitivity of SHG can be utilized for the evaluation of a sample's interface and surface smoothness in polarization-resolved SHG measurements. While the electric field vector of a p-polarized probe beam has a component perpendicular to the surface and is therefore able to sample the components of the second order non-linear susceptibility tensor $\chi^{(2)}$ pointing in that direction, the s-polarized probe beam is completely 'unaware' of the presence of an ideally flat interface. Hence, for the homogeneous C_{60} sample (figure E.1B) the SHG signal amplitude measured for an s-polarized probe beam is one order of magnitude smaller than for the p-polarized probe beam and shows no detectable change at time zero, indicating a well-defined, smooth surface. In the case of an asymmetric sample like the spin coated P3HT layer, the interface sensitivity of SHG is slightly reduced due to the inhomogeneity of the sample. In this case, the weak SHG signal amplitude measured for the s-polarized probe beam partially arises from a bulk and from an interfacial contribution. Although the respective quantitative contributions cannot be distinguished, the interfacial smoothness appears to be high, judging from difference in the signal level change at time zero measured for the two polarizations (figure E.1C). For the C_{60}/P3HT heterojunction (figure E.1D) the SHG signal amplitude measured for the s-polarized probe beam is by a factor of five smaller as measured for the p-polarized probe beam and the signal level change at time zero can be neglected in comparison. That the signal amplitude change is smaller in comparison to the the P3HT sample and that it does not show the initial decrease observed for pristine P3HT (cf. figure E.1C), indicates a very well-defined interface and therefore justifies the preparation strategy.

Appendix F

C_{60}/P3HT: Dynamics at Large Delays

Figures F.1 and F.2 show the long term temporal evolution of the TR-SHG data of pristine C_{60} and of the C_{60}/P3HT heterojunction, respectively. In both cases, no signal decrease is found on picosecond timescales which implies a constant population and degree of localization for the observed 'charged polarons' [138–140] and charge transfer excitons, respectively.

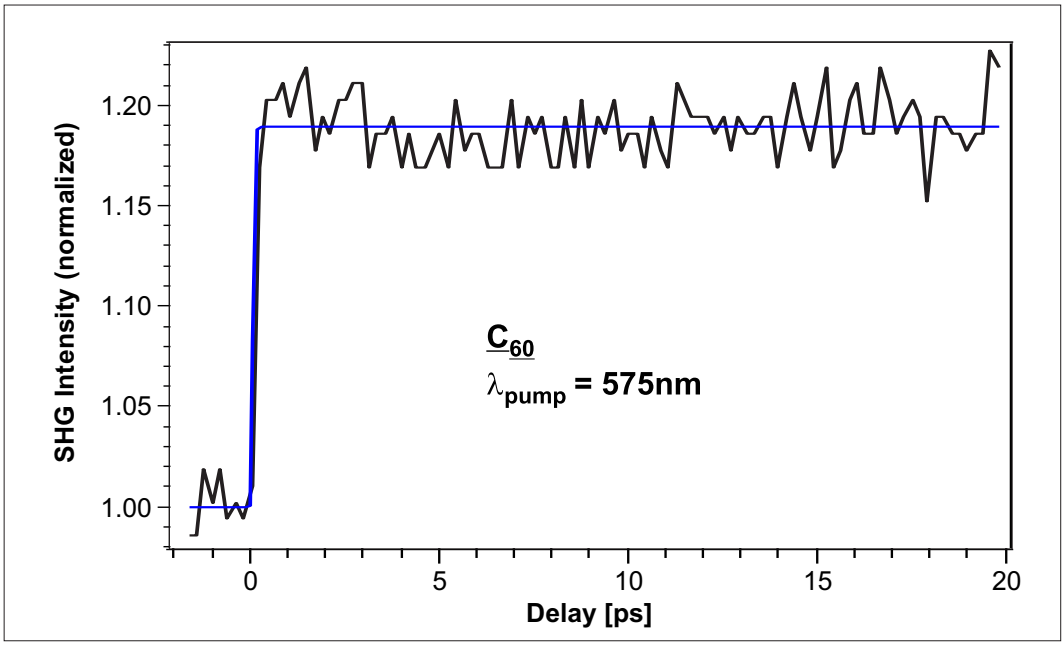

Figure F.1. The pump-induced SHG signal amplitude increase observed for the pristine C_{60} sample is attributed to the population of long-living 'charged polaron' states. The signal level remains constant within the 20 ps timeframe of the measurement, indicating no decay and a constant degree of localization of the excited species in contrast to the hot singlet excitons observed for pristine P3HT.

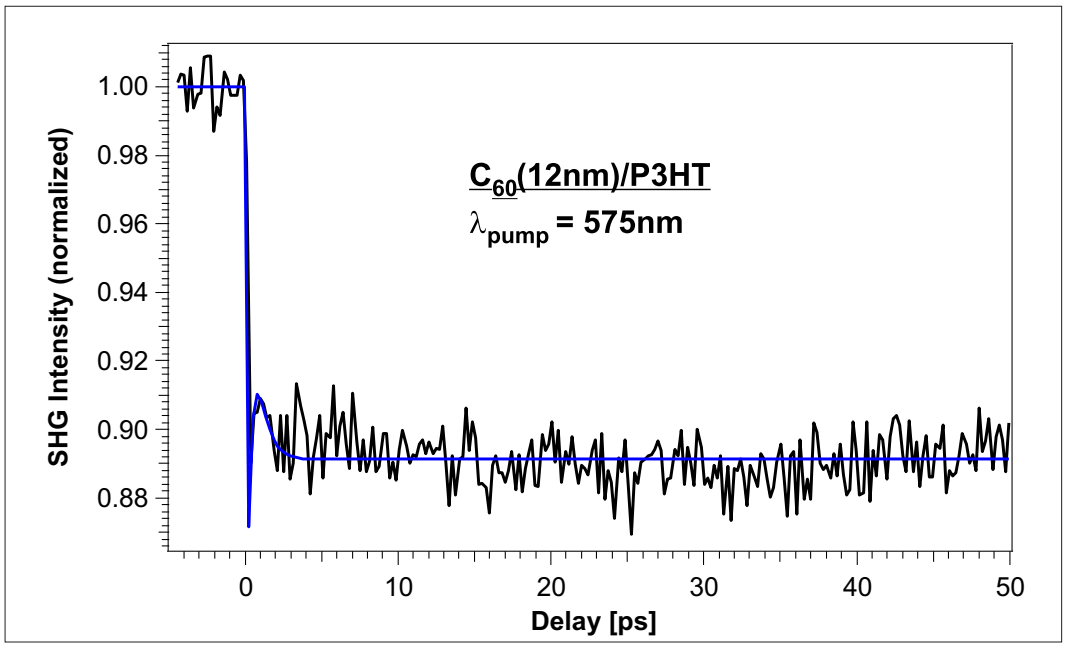

Figure F.2. The interface-derived charge transfer state responsible for the SHG signal amplitude change observed for the C_{60}/P3HT sample appears to be long-living as the corresponding field enhancement is found to be constant within the 50 ps timeframe of the measurement.

Appendix G

C_{60}/P3HT: Direct Acceptor Excitation

As outlined in chapter four, the SHG signal amplitude alteration as a function of the excitation intensity $\Delta I(P_{\mathrm{pump}})$ shown in figure G.1A exhibits a small offset when extrapolating the data to zero pump power. This is due to the direct excitation of the acceptor which needs to be subdivided into two contributions. First, the 12 nm thick top C_{60} layer also absorbs a fraction of the pump pulse according to figure 4.4. Second, although the absorbance of C_{60} at the 800 nm probe beam wavelength is more than two orders of magnitude smaller than for the applied pump beam wavelengths [12], the probe beam power is almost one order of magnitude higher and might thus also slightly excite the acceptor layer. Figure G.1B displays the results of the attempt to account for both effects and correct the data on the SHG signal amplitude changes as a function of the excitation intensity $\Delta I(P_{\mathrm{pump}})$ which is important as the evaluation of the charge transfer yield is based on these data sets. The effect of the pump beam is accounted for by reducing the SHG signal intensity at positive delays by 2.3 counts/s per mW. This corresponds to the signal amplitude change observed for the 20 nm thick pristine C_{60} sample. To account for a possible excitation of the acceptor by the probe beam, the SHG signal levels at all delays are increased by a constant value of 40 counts/s, corresponding to 10 % of the signal amplitude at positive delays, reasonable for the differences in pump and probe beam powers and the absorbances of C_{60} at the respective wavelengths. The orange and gray open circles shown in figure G.1B represent the corrected data. As indicated by the respective fits, the corrections reduce the offset as expected. Unfortunately, without conducting pump–probe experiments with two 800 nm beams and successively varying the probe beam powers, it is unknown which of the two effects contributes to which extend. However, as both the SHG signal amplitude change at short delays due to hot excitons and at large delays due to charge transfer excitons are affected to equal extends, the charge transfer yield is almost unaffected by the offset. It decreases from 0.82 ± 0.06 to 0.78 ± 0.06, which is within the error bars.

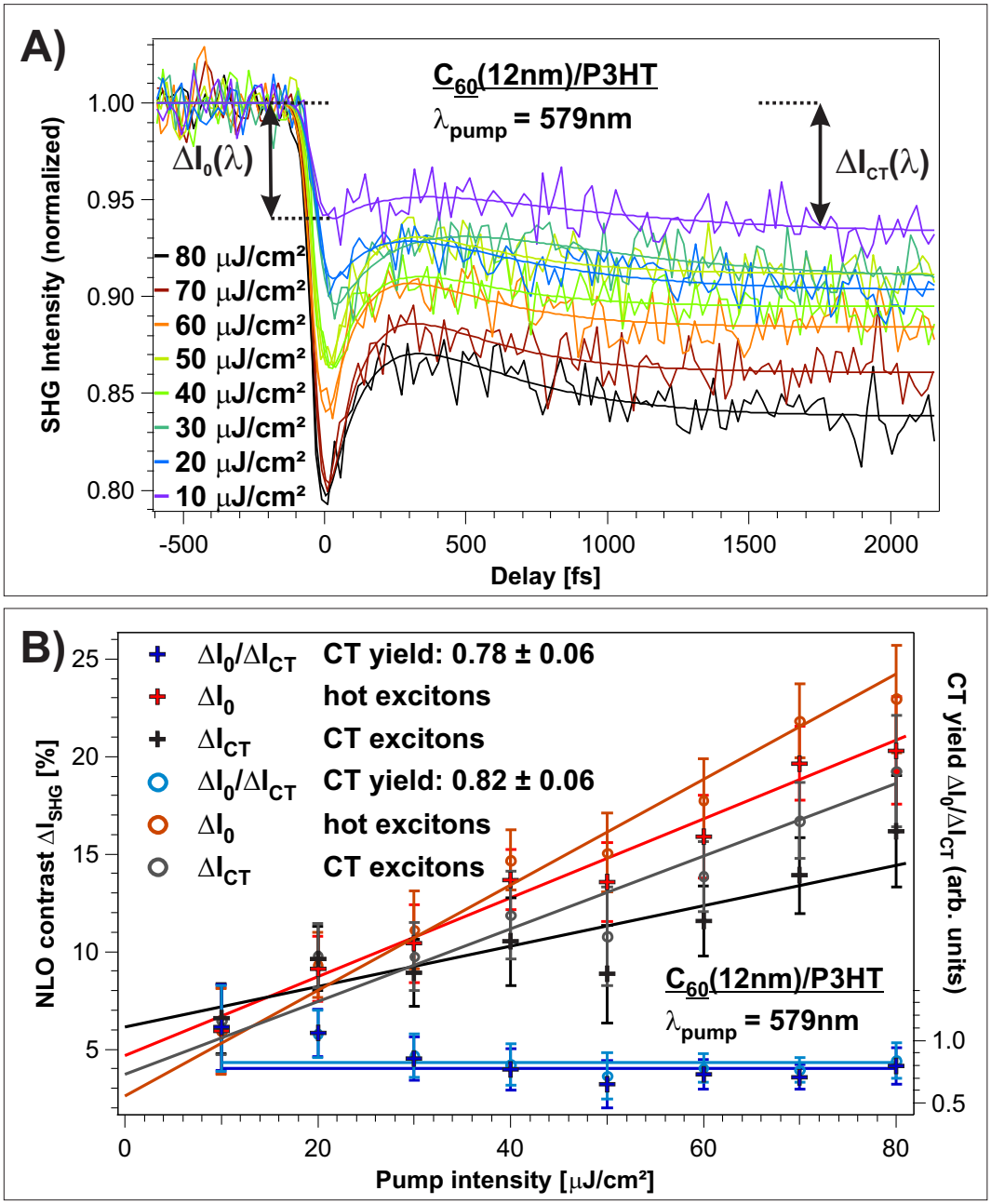

Figure G.1. (A) TR-SHG data for the C_{60}/P3HT sample measured for varying excitation powers between 10 μJ/cm^2 and 80 μJ/cm^2. (B) The measured SHG signal amplitude changes (markers) are corrected to account for the fraction of the signal originating from both a pump- and a probe-induced excitation of the acceptor (open circles). Fortunately, the CT yield $\Delta I_{\mathrm{CT}}/\Delta I_0$ is unaffected by the correction within the error bars (dark to light blue).

Bibliography

[1] P. A. Franken, A. E. Hill, C. W. Peters, and G. Weinreich. GENERATION OF OPTICAL HARMONICS. *Phys. Rev. Lett.*, 7(4):118–119, 1961.

[2] T. H. Maiman. Stimulated Optical Radiation in Ruby. *Nature*, 187:493–494, 1960.

[3] Y. R. Shen. Surfaces probed by second-harmonic and sum-frequency generation. *Nature*, 337:519–525, 1989.

[4] Y. R. Shen, R. B. Hall, and A. B. Ellis. *New laser and Optical Investigation of Chemistry and Sturcture at Interfaces*. Verlag-Chemie, Weinheim, 1986.

[5] Y. R. Shen. Surfaces probed by nonlinear optics. *Surf. Sci.*, 299/300:551–562, 1994.

[6] J. F. McGilp. A review of optical second-harmonic and sum-frequency generation at surfaces and interfaces. *J. Phys. D: Appl. Phys.*, 29:1812–1821, 1996.

[7] P. Guyot-Sionnest, W. Chen, and Y. R. Shen. General considerations on optical second-harmonic generation from surfaces and interfaces. *Phys. Rev. B*, 33(12):8254–8263, 1986.

[8] J. G. Mihaychuk, J. Bloch, Y. Liu, and H. M. van Driel. Time-dependent second-harmonic generation from the Si–SiO_2 interface induced by charge transfer. *Opt. Lett.*, 20(20):2063–2065, 1995.

[9] R. Loucif-Saïbi, K. Nakatani, J. A. Delaire, M. Dumont, and Z. Sekkat. Photoisomerization and Second Harmonic Generation in Disperse Red One-Doped and -Functionalized Poly(methyl methacrylate) Films. *Chem. Mater.*, 5:229–236, 1993.

[10] X. Zhuang, H. S. Lackritz, and Y .R. Shen. Photo-isomerization of polymer monolayers and multi-layers on water. *Chem. Phys. Lett.*, 246:279–284, 1995.

[11] C. Manzo, A. Savoia, D. Paparo, and L. Marrucci. Photoinduced Dynamics of Azobenzene Dyes in Langmuir Films Investigated by Optical Second Harmonic Generation. *Mol. Cryst. Liq. Cryst.*, 454:91–100, 2006.

[12] K. Kuhnke, R. Becker, and K. Kern. Dynamics of second harmonic generation at the C_{60}/quartz interface. *Chem. Phys. Lett.*, 257:569–575, 1996.

[13] W. A. Tisdale, K. J. Williams, B. A. Timp, D. J. Norris, E. S. Aydil, and X.-Y. Zhu. Hot-Electron Transfer from Semiconductor Nanocrystals. *Science*, 328:1543–1547, 2010.

[14] W.-L. Chan, M. Ligges, A. Jailaubekov, L. Kaake, L. Miaja-Avila, and X.-Y. Zhu. Observing the Multiexciton State in Singlet Fission and Ensuing Ultrafast Multielectron Transfer. *Science*, 334:1541–1545, 2011.

[15] A. E. Jailaubekov, A. P. Willard, J. R. Tritsch, W.-L. Chan, N. Sai, R. Gearba, L. G. Kaake, K. J. Williams, K. Leung, P. J. Rossky, and X.-Y. Zhu. Hot charge-transfer excitons set the time limit for charge separation at donor/acceptor interfaces in organic photovoltaics. *Nature Mater.*, 12:66–73, 2013.

[16] H. Petek and S. Ogawa. FEMTOSECOND TIME-RESOLVED TWO-PHOTON PHOTOEMISSION STUDIES OF ELECTRON DYNAMICS IN METALS. *Prog. Surf. Sci.*, 56(4):239–310, 1997.

[17] C. C. Chang. AUGER ELECTRON SPECTROSCOPY. *Surf. Sci.*, 25:53–79, 1971.

[18] F. M. Probst and T. C. Piper. Detection of the Vibrational States of Gases Adsorbed on Tungsten by Low-Energy Electron Scattering. *J. Vac. Sci. Technol.*, 4(2):53–56, 1967.

[19] J. Zegenhagen. Surface structure determination with X-ray standing waves. *Surf. Sci. Rep.*, 18:199–271, 1993.

[20] G. Binning, H. Rohrer, C. Gerber, and E. Weibel. Surface Studies by Scanning Tunneling Microscopy. *Phys. Rev. Lett.*, 49(1):57–61, 1982.

[21] R. M. Feenstra. Scanning tunneling spectroscopy. *Surf. Sci.*, 299/300:965–979, 1994.

[22] N. J. Harrick. SURFACE CHEMISTRY FROM SPECTRAL ANALYSIS OF TOTALLY INTERNALLY REFLECTED RADIATION. *J. Phys. Chem.*, 64:1110–1114, 1960.

[23] H. Borchert. *Solar Cells Based on Colloidal Nanocrystals*. Springer International Publishing, Cham, Heidelberg, New York, Dordrecht, London, 2014.

[24] G. Lüpke. Characterization of semiconductor interfaces by second-harmonic generation. *Surf. Sci. Rep.*, 35:75–161, 1999.

[25] T. F. Heinz, M. M. T. Loy, and W. A. Thompson. Study of Si(111) Surfaces by Optical Second-Harmonic Generation: Reconstruction and Surface Phase Transformation. *Phys. Rev. Lett.*, 54(1):63–66, 1985.

[26] X. Zhuang, P. B. Miranda, D. Kim, and Y. R. Shen. Mapping molecular orientation and conformation at interfaces by surface nonlinear optics. *Phys. Rev. B*, 59(19):12632–12640, 1999.

[27] C. K. Chen, T. F. Heinz, D. Ricard, and Y. R. Shen. Surface-enhanced second-harmonic generation and Raman scattering. *Phys. Rev. B*, 27(4):1965–1979, 1983.

[28] J. F. McGilp and Y. Yeh. PROBING THE BURIED METAL-SEMICONDUCTOR INTERFACE BY OPTICAL SECOND HARMONIC GENERATION: Au ON Si(111) AND Si(100). *Solid State Commun.*, 59(2):91–94, 1986.

[29] T. Rasing. Studies of buried interfaces by optical second-harmonic generation. *Appl. Phys. A*, 59:531–536, 1994.

[30] R.-P. Pan, H. D. Wei, and Y. R. Shen. Optical second-harmonic generation from magnetized surfaces. *Phys. Rev. B*, 39(2):1229–1234, 1989.

[31] H. A. Wierenga, M. W. J. Prins, D. L. Abraham, and T. Rasing. Magnetization-induced optical second-harmonic generation: A probe for interface magnetism. *Phys. Rev. B*, 50(2):1282–1285, 1994.

[32] H. A. Wierenga, W. de Jong, M. W. J. Prins, T. Rasing, R. Vollmer, A. Kirilyuk, H. Schwabe, and J. Kirschner. Interface Magnetism and Possible Quantum Well Oscillations in Ultrathin Co/Cu Films Observed by Magnetization Induced Second Harmonic Generation. *Phys. Rev. Lett.*, 74(8):1462–1465, 1995.

[33] C. H. Bjorkman, T. Yasuda, C. E. Shearon Jr., Y. Ma, G. Lucovsky, U. Emmerichs, C. Meyer, K. Leo, and H. Kurz. Influence of surface roughness on the electrical properties of Si–SiO_2 interfaces and on second-harmonic generation at these interfaces. *J. Vac. Sci. Technol. B*, 11(1521), 1993.

[34] J. I. Dadap, B. Doris, Q. Deng, M. C. Downer, J. K. Lowell, and A. C. Diebold. Randomly oriented Angstrom-scale microroughness at the Si(100)/SiO_2 interface probed by optical second harmonic generation. *Appl. Phys. Lett.*, 64(16):2139–2141, 1994.

[35] C. A. Paddock, G. F. Russell, and R. B. Miles. ANGLE RESOLVED SECOND HARMONIC GENERATION FROM SILVER AND COPPER SURFACES. *Surf. Sci.*, 172:578–597, 1986.

[36] T. F. Heinz, C. K. Chen, D. Ricard, and Y. R. Shen. Spectroscopy of Molecular Monolayers by Resonant Second-Harmonic Generation. *Phys. Rev. Lett.*, 48(7):478–481, 1982.

[37] W. Daum, H.-J. Krause, U. Reichel, and H. Ibach. Identification of Strained Silicon Layers at Si-SiO_2 Interfaces and Clean Si Surfaces by Nonlinear Optical Spectroscopy. *Phys. Rev. Lett.*, 71(8):1234–1237, 1993.

[38] J. F. McGilp, M. Cavanagh, J. R. Power, and J. D. O'Mahony. Spectroscopic optical second-harmonic generation from semiconductor interfaces. *Appl. Phys. A*, 59:401–405, 1994.

[39] A.-M. Janner, R. Eder, B. Koopmans, H. T. Jonkman, and G. A. Sawatzky. Excitons in C_{60} studied by temperature-dependent optical second-harmonic generation. *Phys. Rev. B*, 52(24):17158–17164, 1995.

[40] A.-M. Janner, H. T. Jonkman, and G. A. Sawatzky. Second-harmonic generation spectroscopy: A technique for selectively probing excitons. *Phys. Rev. B*, 63(085111), 2001.

[41] Y.-M. Chang, L. Xu, and H. W. K. Tom. Coherent phonon spectroscopy of GaAs surfaces using time-resolved second-harmonic generation. *Chem. Phys.*, 251:283–308, 2000.

[42] C. H. Lee, R. K. Chang, and N. Bloembergen. NONLINEAR ELECTROREFLECTANCE IN SILICON AND SILVER. *Phys. Rev. Lett.*, 18(5):167–170, 1967.

[43] O. A. Aktsipetrov, A. A. Fedyanin, A. V. Melnikov, E. D. Mishina, A. N. Rubtsov, M. H. Anderson, P. T. Wilson, M. ter Beek, X. F. Hu, J. I. Dadap, and M. C. Downer. dc-electric-field-induced and low-frequency electromodulation second-harmonic generation spectroscopy of Si(001)-SiO_2 interfaces. *Phys. Rev. B*, 60(12):8924–8938, 1999.

[44] A. Bouhelier, M. Beversluis, A. Hartschuh, and L. Novotny. Near-Field Second-Harmonic Generation Induced by Local Field Enhancement. *Phys. Rev. Lett.*, 90(1), 2003.

[45] J. S. Prauzner-Bechcicki, S. Godlewski, and M. Szymonski. Atomic- and molecular-scale devices and systems for single-molecule electronics. *Phys. Status Solidi A*, 209(4):603–612, 2012.

[46] S. E. Thompson and S. Parthasarathy. Moore's law: the future of Si microelectronics. *Mater. Today*, 9(6):20–25, 2006.

[47] J.-P. Wang. MAGNETIC DATA STORAGE Tilting for the top. *Nature Mater.*, 4:191–192, 2005.

[48] S. Kawata and Y. Kawata. Three-Dimensional Optical Data Storage Using Photochromic Materials. *Chem. Rev.*, 100:1777–1788, 2000.

[49] D. D. Awschalom and M. E. Flatté. Challenges for semiconductor spintronics. *Nature Phys.*, 3:153–159, 2007.

[50] J. E. Moore. The birth of topological insulators. *Nature*, 464:194–198, 2010.

[51] A. Candini, S. Klyatskaya, M. Ruben, W. Wernsdorfer, and M. Affronte. Graphene Spintronic Devices with Molecular Nanomagnets. *Nano Lett.*, 11:2634–2639, 2011.

[52] A. C. Whalley, M. L. Steigerwald, X. Guo, and C. Nuckolls. Reversible Switching in Molecular Electronic Devices. *J. Am. Chem. Soc.*, 129:12590–12591, 2007.

[53] L. Grill, M. Dyer, L. Laffarentz, M. Persson, M. V. Peters, and S. Hecht. Nano-architectures by covalent assembly of molecular building blocks. *Nat. Nanotechnol.*, 2:687–691, 2007.

[54] K. Nakada, M. Fujita, G. Dresselhaus, and M. S. Dresselhaus. Edge state in graphene ribbons: Nanometer size effect and edge shape dependence. *Phys. Rev. B*, 54(24):17954–17961, 1996.

[55] J. Cai, P. Ruffieux, R. Jaafar, M. Bieri, T. Braun, S. Blankenburg, M. Muoth, A. P. Seitsonen, M. Saleh, X. Feng, K. Müllen5, and R. Fasel. Atomically precise bottom-up fabrication of graphene nanoribbons. *Nature*, 466:470–473, 2010.

[56] C. Bronner, S. Stremlau, M. Gille, F. Brauße, A. Haase, S. Hecht, and P. Tegeder. Aligning the Band Gap of Graphene Nanoribbons by Monomer Doping. *Angew. Chem. Int. Ed.*, 52:4422–4425, 2013.

[57] R. H. Baughman, A. A. Zakhidov, and W. A. de Heer. Carbon Nanotubes–the Route Toward Applications. *Science*, 297:787–792, 2002.

[58] D. A. Parthenopoulos and P. M. Rentzepis. Three-Dimensional Optical Storage Memory. *Science*, 245:843–845, 1989.

[59] E. Walker and P. M. Rentzepis. TWO-PHOTON TECHNOLOGY A new dimension. *Nature Photon.*, 2:406–408, 2008.

[60] F. M. Raymo and S. Giordani. All-optical processing with molecular switches. *Proc. Natl. Acad. Sci. U.S.A.*, 99(8):4941–4944, 2002.

[61] S. D. Straight, P. A. Liddell, Y. Terazono, T. A. Moore, A. L. Moore, and D. Gust. All-Photonic Molecular XOR and NOR Logic Gates Based on Photochemical Control of Fluorescence in a Fulgimide–Porphyrin–Dithienylethene Triad. *Adv. Funct. Mater.*, 17:777–785, 2007.

[62] B. J. Coe. Molecular Materials Possessing Switchable Quadratic Nonlinear Optical Properties. *Chem. Eur. J.*, 5(9):2464–2471, 1999.

[63] C. Samyn, T. Verbiest, and A. Persoons. Second-order non-linear optical polymers. *Macromol. Rapid. Commun.*, 21:1–15, 2000.

[64] M. Sliwa, S. Létard, I. Malfant, M. Nierlich, P. G. Lacroix, T. Asahi, H. Masuhara, P. Yu, and K. Nakatani. Design, Synthesis, Structural and Nonlinear Optical Properties of Photochromic Crystals: Toward Reversible Molecular Switches. *CHem. Mater.*, 17:4727–4735, 2005.

[65] L. Boubekeur-Lecaque, B. J. Coe, K. Clays, S. Foerier, T. Verbiest, and I. Asselberghs. Redox-Switching of Nonlinear Optical Behavior in Langmuir–Blodgett Thin Films Containing a Ruthenium(II) Ammine Complex. *J. Am. Chem. Soc.*, 130:3286–3287, 2008.

[66] A. Plaquet, M. Guillaume, B. Champagne, F. Castet, L. Ducasse, J.-L. Pozzo, and V. Rodriguez. *In silico* optimization of merocyanine-spiropyran compounds as second-order nonlinear optical molecular switches. *Phys. Chem. Chem. Phys.*, 10:6223–6232, 2008.

[67] A. Priimagi, K. Ogawa, M. Virkki, J. i. Mamiya, M. Kauranen, and A. Shishido. High-Contrast Photoswitching of Nonlinear Optical Response in Crosslinked Ferroelectric Liquid-Crystalline Polymers. *Adv. Mater.*, 24:6410–6415, 2012.

[68] S. R. Marder, B. Kippelen, A. K.-Y. Jen, and N. Peyghambarian. Design and synthesis of chromophores and polymers for electro-optic and photorefractive applications. *Nature*, 388:845–851, 1997.

[69] L. R. Dalton, W. H. Steier, B. H. Robinson, C. Zhang, A. Ren, S. Garner, A. Chen, T. Londergan, L. Irwin, B. Carlson, L. Fifield, G. Phelan,

C. Kincaid, J. Amend, and A. Jen. From molecules to opto-chips: organic electro-optic materials. *J. Mater. Chem.*, 9:1905–1920, 1999.

[70] H. Ma, S. Liu, J. Luo, S. Suresh, L. Liu, S. H. Kang, M. Haller, T. Sassa, L. R. Dalton, and A. K.-Y. Jen. Highly Efficient and Thermally Stable Electro-Optic Dendrimers for Photonics. *Adv. Funct. Mater.*, 12(9):565–574, 2002.

[71] F. Castet, V. Rodriguez, J.-L. Pozzo, L. Ducasse, A. Plaquet, and B. Champagne. Design and Characterization of Molecular Nonlinear Optical Switches. *Acc. Chem. Res.*, 45(11):2656–2665, 2013.

[72] B. Champagne, A. Plaquet, J.-L. Pozzo, V. Rodriguez, and F. Castet. Nonlinear Optical Molecular Switches as Selective Cation Sensors. *J. Am. Chem. Soc.*, 134:8101–8103, 2012.

[73] T. J. Rockey, M. Yang, and H.-L. Dai. Adsorption Energies, Inter-adsorbate Interactions, and the Two Binding Sites within Monolayer Benzene on Ag(111). *J. Phys. Chem. B*, 110:19973–19978, 2006.

[74] M. J. Comstock, N. Levy, A. Kirakosian, J. Cho, F. Lauterwasser, J. H. Harvey, D. A. Strubbe, J. M. J. Fréchet, D. Trauner, S. G. Louie, and M. F. Crommie. Reversible Photomechanical Switching of Individual Engineered Molecules at a Metallic Surface. *Phys. Rev. Lett.*, 99(038301), 2007.

[75] S. K. Yesodha, C. K. S. Pillai, and N. Tsutsumi. Stable polymeric materials for nonlinear optics: a review based on azobenzene systems. *Prog. Polym. Sci.*, 29:45–74, 2004.

[76] G. S. Kumar and D. C. Neckers. Photochemistry of Azobenzene-Containing Polymers. *Chem. Rev.*, 89:1915–1925, 1989.

[77] G. G. Roberts. An applied science perspective of Langmuir–Blodgett films. *Adv. Phys.*, 34(4):475–512, 1985.

[78] T. Seki, M. Sakuragi, Y. Kawanishi, Y. Suzuki, T. Tamaki, R. i. Fukuda, and K. Ichimura. "Command Surfaces" of Langmuir–Blodgett Films. Photoregulations of Liquid Crystal Alignment by Molecularly Tailored Surface Azobenzene Layers. *Langmuir*, 9:211–218, 1993.

[79] P. Dietrich, F. Michalik, R. Schmidt, C. Gahl, G. Mao, M. Breusing, M. B. Raschke, B. Priewisch, T. Elsässer, R. Mendelsohn, M. Weinelt, and K. Rück-Braun. An anchoring strategy for photoswitchable biosensor technology: azobenzene-modified SAMs on Si(111). *Appl. Phys. A*, 93:285–292, 2008.

[80] K. Rück-Braun, M. Å. Petersen, F. Michalik, A. Hebert, D. Przyrembel, C. Weber, S. A. Ahmed, S. Kowarik, and M. Weinelt. Formation of Carboxy- and Amide-Terminated Alkyl Monolayers on Silicon(111) Investigated by ATR-FTIR, XPS, and X-ray Scattering: Construction of Photoswitchable Surfaces. *Langmuir*, 29:11758–11769, 2013.

[81] A. Natansohn and P. Rochon. Photoinduced Motions in Azo-Containing Polymers. *Chem. Rev.*, 102:4139–4175, 2002.

[82] T. Fukuda, H. Matsuda, T. Shiraga, T. Kimura, M. Kato, N. K. Viswanathan, J. Kumar, and S. K. Tripathy. Photofabrication of Surface Relief Grating on Films of Azobenzene Polymer with Different Dye Functionalization. *Macromolecules*, 33(11):4220–4225, 2000.

[83] C. L. Feng, Y. J. Zhang, J. Jin, Y. L. Song, L. Y. Xie, G. R. Qu, L. Jiang, and D. B. Zhu. Reversible Wettability of Photoresponsive Fluorine-Containing Azobenzene Polymer in Langmuir–Blodgett Films. *Langmuir*, 17:4593–4597, 2001.

[84] T. Yamamoto, Y. Umemura, O. Sato, and Y. Einaga. Photoswitchable Magnetic Films: Prussian Blue Intercalated in Langmuir–Blodgett Films Consisting of an Amphiphilic Azobenzene and a Clay Mineral. *Chem. Mater.*, 16:1195–1201, 2004.

[85] C. Bronner, G. Schulze, K. J. Franke, J. I. Pascual, and P. Tegeder. Switching ability of nitro-spiropyran on Au(111): electronic structure changes as a sensitive probe during a ring-opening reaction. *J. Phys.: Condens. Matter*, 23(484005), 2011.

[86] M. Bazarnik, J. Henzl, R. Czajka, and K. Morgenstern. Light driven reactions of single physisorbed azobenzenes. *Chem. Commun.*, 47:7764–7766, 2011.

[87] P. Tegeder. Optically and thermally induced molecular switching processes at metal surfaces. *J. Phys.: Condens. Matter*, 24(394001), 2012.

[88] E. R. McNellis, G. Mercurio, S. Hagen, F. Leyssner, J. Meyer, S. Soubatch, M. Wolf, K. Reuter, P. Tegeder, and F. S. Tautz. Bulky spacer groups – A valid strategy to control the coupling of functional molecules to surfaces? *Chem. Phys. Lett.*, 499:247–249, 2010.

[89] T. Ishikawa, T. Noro, and T. Shoda. Theoretical study on the photoisomerization of azobenzene. *J. Chem. Phys.*, 115(16):7503–7512, 2001.

[90] G. Füchsel, T. Klamroth, J. Dokić, and P. Saalfrank. On the Electronic Structure of Neutral and Ionic Azobenzenes and Their Possible Role as

Surface Mounted Molecular Switches. *J. Phys. Chem. B*, 110:16337–16345, 2006.

[91] E. R. McNellis, C. Bronner, J. Meyer, M. Weinelt, P. Tegeder, and K. Reuter. Azobenzene *versus* 3,3',5,5'-tetra-*tert*-butyl-azobenzene (TBA) at Au(111): characterizing the role of spacer groups. *Phys. Chem. Chem. Phys.*, 12:6404–6412, 2010.

[92] C. Bronner, M. Schulze, S. Hagen, and P. Tegeder. The influence of the electronic structure of adsorbate–substrate complexes on photoisomerization ability. *New J. Phys.*, 14(043023), 2012.

[93] S. Hagen, F. Leyssner, D. Nandi, M. Wolf, and P. Tegeder. Reversible switching of tetra-*tert*-butyl-azobenzene on a Au(111) surface induced by light and thermal activation. *Chem. Phys. Lett.*, 444:85–90, 2007.

[94] S. Hagen, P. Kate, F. Leyssner, D. Nandi, M. Wolf, and P. Tegeder. Excitation mechanism in the photoisomerization of a surface-bound azobenzene derivative: Role of the metallic substrate. *J. Chem. Phys.*, 129(164102), 2008.

[95] S. Wagner, F. Leyssner, C. Kördel, S. Zarwell, R. Schmidt, M. Weinelt, K. Rück-Braun, M. Wolf, and P. Tegeder. Reversible photoisomerization of an azobenzene-functionalized self-assembled monolayer probed by sum-frequency generation vibrational spectroscopy. *Phys. Chem. Chem. Phys.*, 11:6242–6248, 2009.

[96] U. Jung, C. Schütt, O. Filinova, J. Kubitschke, R. Herges, and O. Magnussen. Photoswitching of Azobenzene-Functionalized Molecular Platforms on Au Surfaces. *J. Phys. Chem. C*, 116:25943–25948, 2012.

[97] P. Song, A.-H. Gao, P.-W. Zhou, and T.-S. Chu. Theoretical Study on Photoisomerization Effect with a Reversible Nonlinear Optical Switch for Dithiazolylarylene. *J. Phys. Chem. A*, 116:5392–5397, 2012.

[98] H. Satzger, C. Root, and M. Braun. Excited-State Dynamics of *trans*- and *cis*-Azobenzene after UV Excitation in the $\pi\pi^*$ Band. *J. Phys. Chem. A*, 108:6265–6271, 2004.

[99] W. B. Caldwell, D. J. Campbell, K. Chen, B. R. Herr, C. A. Mirkin, A . Malik, M. K. Durbin, P. Dutta, and K. G. Huang. A Highly Ordered Self-Assembled Monolayer Film of an Azobenzenealkanethiol on Au(111): Electrochemical Properties and Structural Characterization by Synchrotron in-Plane X-ray Diffraction, Atomic Force Microscopy, and Surface-Enhanced Raman Spectroscopy. *J. Am. Chem. Soc.*, 117:6071–6082, 1995.

[100] A. S. Kumar, T. Ye, T. Takami, B.-C. Yu, A. K. Flatt, J. M. Tour, and P. S. Weiss. Reversible Photo-Switching of Single Azobenzene Molecules in Controlled Nanoscale Environments. *Nano Lett.*, 8(6):1644–1648, 2008.

[101] L. F. N. Ah Qune, H. Akiyama, T. Nagahiro, K. Tamada, and A. T. S. Wee. Reversible work function changes induced by photoisomerization of asymmetric azobenzene dithiol self-assembled monolayers on gold. *Appl. Phys. Lett.*, 93(083109), 2008.

[102] C. Gahl, R. Schmidt, D. Brete, E. R. McNellis, W. Freyer, R. Carley, K. Reuter, and M. Weinelt. Structure and Excitonic Coupling in Self-Assembled Monolayers of Azobenzene-Functionalized Alkanethiols. *J. Am. Chem. Soc.*, 132:1831–1838, 2010.

[103] M. Utecht, T. Klamroth, and P. Saalfrank. Optical absorption and excitonic coupling in azobenzenes forming self-assembled monolayers: a study based on density functional theory. *Phys. Chem. Chem. Phys.*, 13:21608–21614, 2011.

[104] D. T. Valley, M. Onstott, S. Malyk, and A. V. Benderskii. Steric Hindrance of Photoswitching in Self-Assembled Monolayers of Azobenzene and Alkane Thiols. *Langmuir*, 29:11623–11631, 2013.

[105] R. Schmidt, E. McNellis, W. Freyer, D. Brete, T. Gießel, C. Gahl, K. Reuter, and M. Weinelt. Azobenzene-functionalized alkanethiols in self-assembled monolayers on gold. *Appl. Phys. A*, 93:267–275, 2008.

[106] C. W. Tang. Two-layer organic photovoltaic cell. *Appl. Phys. Lett.*, 48(2):183–185, 1986.

[107] A. Pivrikas, N. S. Sariciftci, G. Juška, , and R. Österbacka. A Review of Charge Transport and Recombination in Polymer/Fullerene Organic Solar Cells. *Prog. Photovolt: Res. Appl.*, 15:677–696, 2007.

[108] B. Kippelen and J.-L. Brédas. Organic photovoltaics. *Energy Environ. Sci.*, 2(3):241–332, 2009.

[109] F. C. Krebs. Fabrication and processing of polymer solar cells: A review of printing and coating techniques. *Sol. Energ. Mat. Sol. Cells*, 93:394–412, 2009.

[110] M. T. Dang, L. Hirsch, and G. Wantz. P3HT:PCBM, Best Seller in Polymer Photovoltaic Research. *Adv. Mater.*, 23:3597–3602, 2011.

[111] W. Shockley and H. J. Queisser. Detailed Balance Limit of Efficiency of *p-n* Junction Solar Cells. *J. Appl. Phys.*, 32:510–519, 1961.

[112] M. Pope, N. E. Geacintov, and F. Vogel. Singlet Exciton Fission and Triplet-Triplet Exciton Fusion in Crystalline Tetracene. *Mol. Cryst. Liq. Cryst.*, 6:83–104, 1969.

[113] R. E. Merrifield, P. Avakian, and R. P. Groff. FISSION OF SINGLET EXCITONS INTO PAIRS OF TRIPLET EXCITONS IN TETRACENE CRYSTALS. *Chem. Phys. Lett.*, 3(3):155–157, 1969.

[114] M. B. Smith and J Michl. Singlet Fission. *Chem. Rev.*, 110:6891–6936, 2010.

[115] P. M. Zimmerman, F. Bell, D. Casanova, and M. Head-Gordon. Mechanism for Singlet Fission in Pentacene and Tetracene: From Single Exciton to Two Triplets. *J. Am. Chem. Soc.*, 133:19944–19952, 2011.

[116] C. A. Nelson, N. R. Monahan, and X.-Y. Zhu. Exceeding the Shockley–Queisser limit in solar energy conversion. *Energy Environ. Sci.*, 6:3508–3519, 2013.

[117] K. Chen, A. J. Barker, M. E. Reish, K. C. Gordon, and J. M. Hodgkiss. Broadband Ultrafast Photoluminescence Spectroscopy Resolves Charge Photogeneration via Delocalized Hot Excitons in Polymer:Fullerene Photovoltaic Blends. *J. Am. Chem. Soc.*, 135:18502–18512, 2013.

[118] G. Grancini, M. Maiuri, D. Fazzi, A. Petrozza, H.-J. Egelhaaf, D. Brida, G. Cerullo, and G. Lanzani. Hot exciton dissociation in polymer solar cells. *Nature Mater.*, 12:29–33, 2013.

[119] I. Borges, Jr., A. J. A. Aquino, A. Köhn, R. Nieman, W. L. Hase, L. X. Chen, and H. Lischka. *Ab Initio* Modeling of Excitonic and Charge-Transfer States in Organic Semiconductors: The PTB1/PCBM Low Band Gap System. *J. Am. Chem. Soc.*, 135:18252–18255, 2013.

[120] S. Gélinas, A. Rao, A. Kumar, S. L. Smith, A. W. Chin, J. Clark, T. S. van der Poll, G. C. Bazan, and R. H. Friend. Ultrafast Long-Range Charge Separation in Organic Semiconductor Photovoltaic Diodes. *Science*, 343:512–516, 2014.

[121] K. Vandewal, S. Albrecht, E. T. Hoke, K. R. Graham, J. Widmer, J. D. Douglas, M. Schubert, W. R. Mateker, J. T. Bloking, G. F. Burkhard, A. Sellinger, J. M. J. Fréchet, A. Amassian, M. K. Riede, M. D. McGehee, D. Neher, and A. Salleo. Efficient charge generation by relaxed charge-transfer states at organic interfaces. *Nature Mater.*, 13:63–68, 2014.

[122] S. Albrecht, K. Vandewal, J. R. Tumbleston, F. S. U. Fischer, J. D. Douglas, J. M. J. Fréchet, S. Ludwigs, H. Ade, A. Salleo, and D. Neher. On the Efficiency of Charge Transfer State Splitting in Polymer:Fullerene Solar Cells. *Adv. Mater.*, 26:2533–2539, 2014.

[123] J. C. Hummelen, B. W. Knight, F. LePeq, Fred Wudl, J. Yao, and C. L. Wilkins. Preparation and Characterization of Fulleroid and Methanofullerene Derivatives. *J. Org. Chem.*, 60:532–538, 1995.

[124] G. Dennler, M. C. Scharber, and C. J. Brabec. Polymer-Fullerene Bulk-Heterojunction Solar Cells. *Adv. Mater.*, 21:1323–1338, 2009.

[125] L.-M. Chen, Z. Hong, G. Li, and Y. Yang. Recent Progress in Polymer Solar Cells: Manipulation of Polymer:Fullerene Morphology and the Formation of Efficient Inverted Polymer Solar Cells. *Adv. Mater.*, 21:1434–1449, 2009.

[126] J. Campoy-Quiles, T. Ferenczi, T. Agostinelli, P. G. Etchegoin, Y. Kim, T. D. Anthopoulos, P. N. Stavrinou, D. D. C. Bradley, and J. Nelson. Morphology evolution via self-organization and lateral and vertical diffusion in polymer:fullerene solar cell blends. *Nature Mater.*, 7:158–164, 2008.

[127] Z. Xu, L.-M. Chen, M.-H. Chen, G. Li, and Y. Yang. Energy level alignment of pol(3-hexylthiophene): [6,6]-phenyl C_{61} butyric acid methyl ester bulk heterojunction. *Appl. Phys. Lett.*, 95(013301), 2009.

[128] O. J. Korovyanko, R. Österbacka, X. M. Jiang, and Z. V. Vardeny. Photoexcitation dynamics in regioregular and regiorandom polythiophene films. *Phys. Rev. B*, 64(235122), 2001.

[129] J. Piris, T. E. Dykstra, A. A. Bakulin, P. H. M. van Loosdrecht, W. Knulst, M. T. Trinh, J. M. Schins, and L. D. A. Siebbeles. Photogeneration and Ultrafast Dynamics of Excitons and Charges in P3HT/PCBM Blends. *J. Phys. Chem. C*, 113:14500–14506, 2009.

[130] J. Guo, H. Ohkita, H. Benten, and S. Ito. Near-IR Femtosecond Transient Absorption Spectroscopy of Ultrafast Polaron and Triplet Exciton Formation in Polythiophene Films with Different Regioregularities. *J. Am. Chem. Soc.*, 131:16869–16880, 2009.

[131] J. Guo, H. Ohkita, H. Benten, and S. Ito. Charge Generation and Recombination Dynamics in Poly(3-hexylthiophene)/Fullerene Blend Films with Different Regioregularities and Morphologies. *J. Am. Chem. Soc.*, 132:6154–6164, 2010.

[132] D. Herrmann, S. Niesar, C. Scharsich, A. Köhler, M. Stutzmann, and E. Riedle. Role of Structural Order and Excess Energy on Ultrafast Free Charge Generation in Hybrid Polythiophene/Si Photovoltaics Probed in Real Time by Near-Infrared Broadband Transient Absorption. *J. Am. Chem. Soc.*, 133(45):18220–18233, 2011.

[133] A. R. S. Kandada, G. Grancini, A. Petrozza, S. Perissinotto, D. Fazzi, S. S. K. Raavi, and G. Lanzani. Ultrafast Energy Transfer in Ultrathin Organic Donor/Acceptor Blend. *Sci. Rep.*, 3(2073), 2013.

[134] A. Ruseckas, P. Wood, I. D. W. Samuel, G. R. Webster, W. J. Mitchell, P. L. Burn, and V. Sundström. Ultrafast depolarization of the fluorescence in a conjugated polymer. *Phys. Rev. B*, 72(115214), 2005.

[135] I. Hwang and G. D. Scholes. Electronic Energy Transfer and Quantum-Coherence in π-Conjugated Polymers. *Chem. Mater.*, 23:610–620, 2011.

[136] F. Terenziani, S. Ghosh, A.-C. Robin, P. K. Das, and M. Blanchard-Desce. Environmental and Excitonic Effects on the First Hyperpolarizability of Polar Molecules and Related Dimers. *J. Phys. Chem. B*, 112:11498–11505, 2008.

[137] A. Datta and S. K. Pati. Effects of Dipole Orientations on Nonlinear Optical Properties of Oxo-Bridged Dinitroaniline Systems. *J. Phys. Chem. A*, 108:320–325, 2004.

[138] K. Harigaya. Lattice distortion and energy-level structures in doped C_{60} and C_{70} molecules studied with the extended Su-Schrieffer-Heeger model: Polaron excitations and optical absorption. *Phys. Rev. B*, 45(23):13676–13684, 1992.

[139] B. Friedman. Electronic absorption spectra in C_{60}^- and C_{60}^+. *Phys. Rev. B*, 48(4):2743–2747, 1993.

[140] D. Dick, X. Wei, S. Jeglinski, R. E. Benner, Z. V. Vardeny, D. Moses, V. I. Srdanov, and F. Wudl. Transient Spectroscopy of Excitons and Polarons in C_{60} Films from Femtoseconds to Milliseconds. *Phys. Rev. Lett.*, 73(20):2760–2763, 1994.

[141] R. L. Sutherland. *Handbook of Nonlinear Optics*. CRC press, New York, 2003.

[142] K. H. Yang, P. L. Richards, and Y. R. Shen. Generation of Far-Infrared Radiation by Picosecond Light Pulses in $LiNbO_3$. *Appl. Phys. Lett.*, 19(9):320–323, 1971.

[143] K. H. Yang, J. R. Morris, P. L. Richards, and Y. R. Shen. Phase-matched far-infrared generation by optical mixing of dye laser beams. *Appl. Phys. Lett.*, 23(12):669–671, 1973.

[144] B. Koopmans. *Interface and Bulk Contributions in Optical Second-Harmonic Generation.* Ph.D. Thesis, University of Groningen, the Netherlands, 1993.

[145] N. Bloembergen. Surface nonlinear optics: a historical overview. *Appl. Phys. B*, 68:289–293, 1999.

[146] M. Omote, H. Kitaoka, E. Kobayashi, O. Suzuki, K. Aratake, H. Sano, G. Mizutani, W. Wolf, and R. Podloucky. Spectral, tensor, and *ab initio* theoretical analysis of optical second harmonic generation from the rutile TiO_2(110) and (001) faces. *J. Phys.: Condens Matter*, 17:S175–S200, 2005.

[147] P. D. Maker, R. W. Terhune, M. Nisenoff, and C. M. Savage. EFFECTS OF DISPERSION AND FOCUSING ON THE PRODUCTION OF OPTICAL HARMONICS. *Phys. Rev. Lett.*, 8(1):21–22, 1962.

[148] C. Chen, Y. Wang, B. Wu, K. Wu, W. Zeng, and L. Yu. Design and synthesis of an ultraviolet-transparent nonlinear optical crystal $Sr_2Be_2B_2O_7$. *Nature*, 373:322–324, 1995.

[149] A. Seemann, H.-J. Egelhaaf, C. J. Brabec, and J. A. Hauch. Influence of oxygen on semi-transparent organic solar cells with gas permeable electrodes. *Organ. Electron.*, 10:1424–1428, 2009.

[150] K. Norrman, S. A. Gevorgyan, and F. C. Krebs. Water-Induced Degradation of Polymer Solar Cells Studied by $H_2{}^{18}O$ Labeling. *Appl. Mater. Interfaces*, 1(1):102–112, 2009.

[151] J. Schafferhans, A. Baumann, A. Wagenpfahl, C. Deibel, and V. Dyakonov. Oxygen doping of P3HT:PCBM blends: Influence on trap states, charge carrier mobility and solar cell performance. *Organ. Electron.*, 11:1693–1700, 2010.

[152] J. C. Lambropoulos, M. R. Jolly, C. A. Amsden, S. E. Gilman, M. J. Sinicropi, D. Diakomihalis, and S. D. Jacobs. Thermal conductivity of dielectric thin films. *J. Appl. Phys.*, 66(9):4230–4242, 1989.

[153] F. A. Haight. *Handbook of the Poisson Distribution.* John Wiley & Sons, New York, 1967.

[154] D. J. Kissick, R. D. Muir, and G. J. Simpson. Statistical treatment of photon/electron counting; extending the linear dynamic range from the dark count rate to saturation. *Anal. Chem.*, 82(24):10129–10134, 2010.

[155] Mark Fox. *Optical Properties of Solids*. Oxford University press, Oxford, New York, 2001.

[156] T.-Q. Nguyen, I. B. Martini, J. Liu, and B. J. Schwartz. Controlling Interchain Interactions in Conjugated Polymers: The Effects of Chain Morphology on Exciton–Exciton Annihilation and Aggregation in MEH–PPV Films. *J. Phys. Chem. B*, 104:237–255, 2000.

[157] P. E. Shaw, A. Ruseckas, and I. D. W. Samuel. Exciton Diffusion Measurements in Poly(3-hexylthiophene). *Adv. Mater.*, 20:3516–3520, 2008.

[158] A. J. Lewis, A. Ruseckas, O. P. M. Gaudin, G. R. Webster, P. L. Burn, and I. D. W. Samuel. Singlet exciton diffusion in MEH-PPV films studied by exciton–exciton annihilation. *Org. Electron.*, 7:452–456, 2006.

[159] S. Albert-Seifried and R. H. Friend. Measurement of thermal modulation of optical absorption in pump-probe spectroscopy of semiconducting polymers. *Appl. Phys. Lett.*, 98(223304), 2011.

[160] T. Nägele, R. Hoche, W. Zinth, and J. Wachtveitl. Femtosecond photoisomerization of *cis*-azobenzene. *Chem. Phys. Lett.*, 272:489–495, 1997.

[161] W. Freyer, D. Brete, R. Schmidt, C. Gahl, R. Carley, and M. Weinelt. Switching behavior and optical absorbance of azobenzene-functionalized alkanethiols in different environments. *J. Photochem. Photobiol. A*, 204:102–109, 2009.

[162] T. Moldt, D. Brete, D. Przyrembel, J. R. Goldman, R. Klajn, C. Gahl, and M. Weinelt. Tailoring the Optical Response of Self-Assembled Monolayers with Azobenzene Derivatives on Planar and Curved Surfaces. *in preparation*, 2014.

[163] S. Dietrich. *Synthese und photochrome Eigenschaften funktionalisierter Indolylfulgimide*. Ph.D. Thesis, Technischen Universität Berlin, 2006.

[164] C. H. de Villeneuve, F. Michalik, J. N. Chazalviel, K. Rück-Braun, and P. Allongue. Quantitative IR Readout of Fulgimide Monolayer Switching on Si(111) Surfaces. *Adv. Mater.*, 25:416–421, 2013.

[165] G. Pace, V. Ferri, C. Grave, M. Elbing, C. von Hänisch, M. Zharnikov, M. Mayor, M. A. Rampi, and P. Samorí. Cooperative light-induced molecular movements of highly ordered azobenzene self-assembled monolayers. *Proc. Natl. Acad. Sci. U.S.A.*, 104(24):9937–9942, 2007.

[166] Z. Yu and S. Hecht. Cooperative Switching Events in Azobenzene Foldamer Denaturation. *Chem. Eur. J.*, 18:10519–10524, 2012.

[167] B. Baisch, D. Raffa, U. Jung, O. M. Magnussen, C. Nicolas, J. Lacour, J. Kubitschke, and R. Herges. Mounting Freestanding Molecular Functions onto Surfaces: The Platform Approach. *J. Am. Chem. Soc.*, 131:442–443, 2009.

[168] W. R. Browne and B. L. Feringa. *Molecular Switches*. Wiley-VCH, Weinheim, 2011.

[169] S. Goldschmidt, R. Riedle, and A. Reichardt. ÜBER DIE BISDIPHENYLENFULGIDE UND DIE SPALTUNG DER BISDIPHENYLENFULGENSAÜRE IN OPTISCH AKTIVE KOMPONENTEN. *Liebigs Ann. Chem.*, 604(1):121–132, 1957.

[170] H. G. Heller, K. Koh, C. Elliot, and J. Whittall. FULGIDES AND FULGIMIDES FOR PRACTICAL APPLICATIONS. *Mol. Cryst. Liq. Cryst.*, 246:79–86, 1994.

[171] H. Stobbe. Die Farbe der "Fulgensäuren" und "Fulgide". *Ber. Dtsch. Chem. Ges.*, 38(3):3673–3682, 1905.

[172] T. Brust, S. Draxler, S. Malkmus, C. Schulz, M. Zastrow, K. Rück-Braun, W. Zinth, and M. Braun. Ultrafast dynamics and temperature effects on the quantum efficiency of the ring-opening reaction of a photochromic indolylfulgide. *J. Mol. Liq.*, 141:137–139, 2008.

[173] T. Cordes, T. T. Herzog, S. Malkmus, S. Draxler, T. Brust, J. A. DiGirolamo, Watson J. Lees, and M. Braun. Wavelength and solvent independent photochemistry: the electrocyclic ring-closure of indolylfulgides. *Photochem. Photobiol. Sci.*, 8:528–534, 2009.

[174] K. Uchida, Y. Yamanoi, T. Yonezawa, and H. Nishihara. Reversible On/Off Conductance Switching of Single Diarylethene Immobilized on a Silicon Surface. *J. Am. Chem. Soc.*, 133:9239–9241, 2011.

[175] M. Piantek, G. Schulze, M. Koch, K. J. Franke, F. Leyssner, A. Krüger, C. Navío, J. Miguel, M. Bernien, M. Wolf, W. Kuch, P. Tegeder, and J. I. Pascual. Reversing the Thermal Stability of a Molecular Switch on a Gold Surface: Ring-Opening Reaction of Nitrospiropyran. *J. Am. Chem. Soc.*, 131:12729–12735, 2009.

[176] G. S. Hartley. The *Cis*-form of Azobenzene. *Nature*, 140(3537):281, 1937.

[177] D. Brete, D. Przyrembel, C. Eickhoff, R. Carley, W. Freyer, K. Reuter, C. Gahl, and M. Weinelt. Mixed self-assembled monolayers of azobenzene photoswitches with trifluoromethyl and cyano end groups. *J. Phys.: Condens. Matter*, 24(394015), 2012.

[178] J. Auernheimer, C. Dahmen, U. Hersel, A. Bausch, and H. Kessler. Photoswitched Cell Adhesion on Surfaces with RGD Peptides. *J. Am. Chem. Soc.*, 127:16107–16110, 2005.

[179] D. Liu, Y. Xie, H. Shao, and X. Jiang. Using Azobenzene-Embedded Self-Assembled Monolayers To Photochemically Control Cell Adhesion Reversibly. *Angew. Chem. Int. Ed.*, 48:4406–4408, 2009.

[180] D. Gust, J. Andréasson, U. Pischel, T. A. Moore, and A. L. Moore. Data and signal processing using photochromic molecules. *Chem. Commun.*, 48:1947–1957, 2012.

[181] R. Hoffmann and R. B. Woodward. The Conservation of Orbital Symmetry. *Acc. Chem. Res.*, 1(1):17–22, 1968.

[182] R. Matsushima and H. Sakaguchi. Comparison of the photochromic properties of fulgides and fulgimides. *J. Photochem. Photobiol. A*, 108:239–245, 1997.

[183] R. Matsushima, M. Nishiyama, and M. Doi. Improvements in the fatigue resistances of photochromic compounds. *J. Photochem. Photobiol. A*, 139:63–69, 2001.

[184] S. Malkmus, F. O. Koller, B. Heinz, W. J. Schreier, T. E. Schrader, W. Zinth, C. Schulz, S. Dietrich, K. Rück-Braun, and M. Braun. Ultrafast ring opening reaction of a photochromic indolyl-fulgimide. *Chem. Phys. Lett.*, 417:266–271, 2006.

[185] F. O. Koller, W. J. Schreier, T. E. Schrader, S. Malkmus, C. Schulz, S. Dietrich, K. Rück-Braun, and M. Braun. Ultrafast Ring-Closure Reaction of Photochromic Indolylfulgimides Studied with UV-Pump–IR-Probe Spectroscopy. *J. Phys. Chem. A*, 112:210–214, 2008.

[186] A. Santiago and R. S. Becker. Photochromic Fulgides. Spectroscopy and Mechanism of Photoreactions. *J. Am. Chem. Soc.*, 90(14):3654–3658, 1968.

[187] H. G. Heller and R. M. Megit. Overcrowded Molecules. Part IX. Fatigue-free Photochromic Systems involving (*E*)-2-lsopropylidene-3-(mesitylmethylene)succinic Anhydride and *N*-Phenylimide. *J. Chem. Soc., Perkin Trans. 1*, pages 923–927, 1974.

[188] Y. Yokoyama. Fulgides for Memories and Switches. *Chem. Rev.*, 100:1717–1739, 2000.

[189] S. Uchida, S. Yamada, Y. Yokoyama, and Y. Kurita. Steric Effects of Substituents on the Photochromism of Indolylfulgides. *Bull. Chem. Soc. Jpn.*, 68(6):1677–1682, 1995.

[190] S. Uchida, Y. Yokoyama, J. Kiji, T. Okano, and H. Kitamura. Electronic Effects of Substituents on Indole Nitrogen on the Photochromic Properties of Indolylfulgides. *Bull. Chem. Soc. Jpn.*, 68(10):2961–2967, 1995.

[191] Y. Yokoyama, T. Tanaka, T. Yamane, and Y. Kurita. Synthesis and Photochromic Behavior of 5-Substituted Indolylfulgides. *Chem. Lett.*, 20(7):1125–1128, 1991.

[192] Y. Chen, C. Wang, M. Fan, B. Yao, and N. Menke. Photochromic fulgide for holographic recording. *Opt. Mater.*, 26:75–77, 2004.

[193] J. Walz, K. Ulrich, H. Port, H. C. Wolf, J. Wonner, and F. Effenberger. Fulgides as switches for intramolecular energy transfer. *Chem. Phys. Lett.*, 213(3,4):321–324, 1993.

[194] M. Seibold and H. Port. Mid-infrared recognition of the reversible photoswitching of fulgides. *Chem. Phys. Lett.*, 252:135–140, 1996.

[195] Y. C. Liang, A. S. Dvornikov, and P. M. Rentzepis. Nonvolatile read-out molecular memory. *Proc. Natl. Acad. Sci. U.S.A.*, 100(14):8109–8112, 2003.

[196] I. K. Lednev, T.-Q. Ye, P. Matousek, M. Towrie, P. Foggi, F. V. R. Neuwahl, S. Umapathy, R. E. Hester, and J. N. Moore. Femtosecond time-resolved UV-visible absorption spectroscopy of trans-azobenzene: dependence on excitation wavelength. *Chem. Phys. Lett.*, 290:68–74, 1998.

[197] C. J. Barrett, J. i. Mamiya, K. G. Yager, and T. Ikeda. Photo-mechanical effects in azobenzene-containing soft materials. *Soft Matter*, 3:1249–1261, 2007.

[198] G. S. Hartley. 113. *The* cis-*Form of Ambenzene and the Velocity of the Thermal* cis $\rightarrow$ trans-*Conversion of Azobenzene and Some Derivatives. J. Chem. Soc.*, pages 633–642, 1938.

[199] T. Cusati, G. Granucci, M. Persico, and G. Spighi. Oscillator strength and polarization of the forbidden $n \rightarrow \pi^*$ band of *trans*-azobenzene: A computational study. *J. Chem. Phys.*, 128(194312), 2008.

[200] E. W.-G. Diau. A New Trans-to-Cis Photoisomerization Mechanism of Azobenzene on the $S_1(n,\pi^*)$ Surface. *J. Phys. Chem. A*, 108:950–956, 2004.

[201] R. J. Maurer and K. Reuter. Bistability Loss as a Key Feature in Azobenzene (Non-)Switching on Metal Surfaces. *Angew. Chem. Int. Ed.*, 124:12175–12177, 2012.

[202] J. Shao, Y. Lei, Z. Wen, Y. Dou, and Z. Wang. Nonadiabatic simulation study of photoisomerization of azobenzene: Detailed mechanism and load-resisting capacity. *J. Chem. Phys.*, 129(164111), 2008.

[203] N. L. Doltsinis M. Böckmann and D. Marx. Nonadiabatic Hybrid Quantum and Molecular Mechanic Simulations of Azobenzene Photoswitching in Bulk Liquid Environment. *J. Phys. Chem. A*, 114:745–754, 2010.

[204] G. Mercurio, E. R. McNellis, I. Martin, S. Hagen, F. Leyssner, S. Soubatch, J. Meyer, M. Wolf, P. Tegeder, F. S. Tautz, and K. Reuter. Structure and Energetics of Azobenzene on Ag(111): Benchmarking Semiempirical Dispersion Correction Approaches. *Phys. Rev. Lett.*, 104(036102), 2010.

[205] A. Kirakosian, M. J. Comstock, J. Cho, and M. F. Crommie. Molecular commensurability with a surface reconstruction: STM study of azobenzene on Au(111). *Phys. Rev. B*, 71(113409), 2005.

[206] B.-Y. Choi, S. Kim S.-J. Kahng, H. Kim, H. W. Kim, Y. J. Song, J. Ihm, and Y. Kuk. Conformational Molecular Switch of the Azobenzene Molecule: A Scanning Tunneling Microscopy Study. *Phys. Rev. Lett.*, 96(156106), 2006.

[207] M. Alemani, S. Selvanathan, F. Ample, M. V. Peters, K.-H. Rieder, F. Moresco, C. Joachim, S. Hecht, and L. Grill. Adsorption and Switching Properties of Azobenzene Derivatives on Different Noble Metal Surfaces: Au(111), Cu(111), and Au(100). *J. Phys. Chem. C*, 112:10509–10514, 2008.

[208] A. Safiei, J. Henzl, and K. Morgenstern. Isomerization of an Azobenzene Derivative on a Thin Insulating Layer by Inelastically Tunneling Electrons. *Phys. Rev. Lett.*, 104(216102), 2010.

[209] J. Henzl, P. Puschnig, C. Ambrosch-Draxl, A. Schaate, B. Ufer, P. Behrens, and K. Morgenstern. Photoisomerization for a molecular switch in contact with a surface. *Phys. Rev. B*, 85(035410), 2012.

[210] C.-W. Jiang, R.-H. Xie, F.-L. Li, and R. E. Allen. Comparative Studies of the *trans–cis* Photoisomerizations of Azobenzene and a Bridged Azobenzene. *J. Phys. Chem. A*, 115:244–249, 2011.

[211] M. Alemani, M. V. Peters, S. Hecht, K.-H. Rieder, F. Moresco, and L. Grill. Electric Field-Induced Isomerization of Azobenzene by STM. *J. Am. Chem. Soc.*, 128:14446–14447, 2006.

[212] P. Tegeder, S. Hagen, F. Leyssner, M. V. Peters, S. Hecht, T. Klamroth, P. Saalfrank, and M. Wolf. Electronic structure of the molecular switch tetra-*tert*-butyl-azobenzene adsorbed on Ag(111). *Appl. Phys. A*, 88:465–472, 2007.

[213] M. Schulze, C. Bronner, and P. Tegeder. Adsorption energetics of azobenzenes on noble metal surfaces. *J. Phys.: Condens. Matter*, 26(355004), 2014.

[214] C. Bronner, B. Priewisch, K. Rück-Braun, and P. Tegeder. Photoisomerization of an Azobenzene on the Bi(111) Surface. *J. Phys. Chem. C*, 117:27031–27038, 2013.

[215] J. Repp, G. Meyer, S. M. Stojković, A. Gourdon, and C. Joachim. Molecules on Insulating Films: Scanning-Tunneling Microscopy Imaging of Individual Molecular Orbitals. *Phys. Rev. Lett.*, 94(026803), 2005.

[216] P. Liljeroth, J. Repp, and G. Meyer. Current-Induced Hydrogen Tautomerization and Conductance Switching of Naphthalocyanine Molecules. *Science*, 317:1203–1206, 2007.

[217] K. Morgenstern. Switching individual molecules by light and electrons: From isomerisation to chirality flip. *Prog. Surf. Sci.*, 86:115–161, 2011.

[218] A. Ulman. Formation and Structure of Self-Assembled Monolayers. *Chem. Rev.*, 96:1533–1554, 1996.

[219] H. A. Biebuyck and G. M. Whitesides. Interchange between Monolayers on Gold Formed from Unsymmetrical Disulfides and Solutions of Thiols: Evidence for Sulfur–Sulfur Bond Cleavage by Gold Metal. *Langmuir*, 9:1766–1770, 1993.

[220] J. B. Schlenoff, M. Li, and H. Ly. Stability and Self-Exchange in Alkanethiol Monolayers. *J. Am. Chem. Soc.*, 117:12528–12536, 1995.

[221] D. D. M. Wayner and R. A. Wolkow. Organic modification of hydrogen terminated silicon surfaces. *J. Chem. Soc., Perkin Trans. 2*, pages 23–34, 2002.

[222] S. S. S. Vegunta, J. N. Ngunjiri, and J. C. Flake. Electrochemical and Thermal Grafting of Alkyl Grignard Reagents onto (100) Silicon Surfaces. *Langmuir*, 25(21):12750–12756, 2009.

[223] J. A. Delaire and K. Nakatani. Linear and Nonlinear Optical Properties of Photochromic Molecules and Materials. *Chem. Rev.*, 100:1817–1845, 2000.

[224] M. A. Wolak, N. B. Gillespie, C. J. Thomas, R. R. Birge, and W. J. Lees. Optical properties of photochromic fluorinated indolylfulgides. *J. Photochem. Photobiol. A*, 144:83–91, 2001.

[225] N. I. Islamova, X. Chen, J. A. DiGirolamo, Y. Silva, and W. J. Lees. Thermal stability and photochromic properties of a fluorinated indolylfulgimide in a protic and aprotic solvent. *J. Photochem. Photobiol. A*, 199:85–91, 2008.

[226] A. Plaquet, B. Champagne, F. Castet, L. Ducasse E. Bogdan, V. Rodriguez, and J.-L. Pozzo. Theoretical investigation of the dynamic first hyperpolarizability of DHA–VHF molecular switches. *New J. Chem.*, 33:1349–1356, 2009.

[227] G. Zimmerman, L.-Y. Chow, and U.-J. Paik. The Photochemical Isomerization of Azobenzene. *J. Am. Chem. Soc.*, 80(14):3528–3531, 1958.

[228] V. Deblauwe and G. Smets. Quantum yields of the photochromic reactions of heterocyclic fulgides and fulgimides. *Makromol. Chem.*, 189:2503–2512, 1988.

[229] C.-W. Chang, Y.-C. Lu, T.-T. Wang, and E. W.-G. Diau. Photoisomerization Dynamics of Azobenzene in Solution with S_1 Excitation: A Femtosecond Fluorescence Anisotropy Study. *J. Am. Chem. Soc.*, 126:10109–10118, 2004.

[230] M. Xi, M. X. Yang, S. K. Jo, and B. E. Bent. Benzene adsorption on Cu(111): Formation of a stable bilayer. *J. Chem. Phys.*, 101(10):9122–9131, 1994.

[231] B. A. Gregg and M. C. Hanna. Comparing organic to inorganic photovoltaic cells: Theory, experiment, and simulation. *J. Appl. Phys.*, 93(6):3605–3614, 2003.

[232] C. J. Brabec, S. Gowrisanker, J. J. M. Halls, D. Laird, S. Jia, and S. P. Williams. Polymer–Fullerene Bulk-Heterojunction Solar Cells. *Adv. Mater.*, 22:3839–3856, 2010.

[233] N. S. Sariciftci, L. Smilowitz, A. J. Heeger, and F. Wudl. Photoinduced Electron Transfer from a Conducting Polymer to Buckminsterfullerene. *Science*, 258:1474–1476, 1992.

[234] M. M. Wienk, J. M. Kroon, W. J. H. Verhees, J. Knol, J. C. Hummelen, P. A. van Hal, and R. A. J. Janssen. Efficient Methano[70]fullerene/MDMO-PPV Bulk Heterojunction Photovoltaic Cells. *Angew. Chem. Int. Ed.*, 42:3371–3375, 2003.

[235] F. Zhang, Z. Zhuo, J. Zhang, X. Wang, X. Xu, Z. Wang, Y. Xin, J. Wang, J. Wang, W. Tang, Z. Xu, and Y. Wang. Influence of $PC_{60}BM$ or $PC_{70}BM$ as electron acceptor on the performance of polymer solar cells. *Sol. Energ. Mat. Sol. Cells*, 97:71–77, 2012.

[236] B. C. Thompson and J. M. J. Fréchet. Polymer–Fullerene Composite Solar Cells. *Angew. Chem. Int. Ed.*, 47:58–77, 2008.

[237] C.-Y. Liu, Z. C. Holman, and U. R. Kortshagen. Hybrid Solar Cells from P3HT and Silicon Nanocrystals. *Nano Lett.*, 9(1):449–452, 2009.

[238] R. B. Ross, C. M. Cardona, D. M. Guldi, S. G. Sankaranarayanan, M. O. Reese, N. Kopidakis, J. Peet, B. Walker, G. C. Bazan, E. Van Keuren, B. C. Holloway, and M. Drees. Endohedral fullerenes for organic photovoltaic devices. *Nature Mater.*, 8:208–212, 2009.

[239] Y. He and Y. Li. Fullerene derivative acceptors for high performance polymer solar cells. *Phys. Chem. Chem. Phys.*, 13:1970–1983, 2011.

[240] S. Günes, H. Neugebauer, and N. S. Sariciftci. Conjugated Polymer-Based Organic Solar Cells. *Chem. Rev.*, 107:1324–1338, 2007.

[241] A. A. Bakulin, A. Rao, V. G. Pavelye, P. H. M. van Loosdrecht, M. S. Pshenichnikov, D. Niedzialek, J. Cornil, D. Beljonne, and R. H. Friend. The Role of Driving Energy and Delocalized States for Charge Separation in Organic Semiconductors. *Science*, 335:1340–1344, 2012.

[242] J. Peet, J. Y. Kim, N. E. Coates, W. L. Ma, A. J. Heeger D. Moses, and G. C. Bazan. Efficiency enhancement in low-bandgap polymer solar cells by processing with alkane dithiols. *Nature Mater.*, 6:497–500, 2007.

[243] T. Ameri, G. Dennler, C. Lungenschmied, and C. J. Brabec. Organic tandem solar cells: A review. *Energy Environ. Sci.*, 2:347–363, 2009.

[244] G. Yu, J. Gao, J. C. Hummelen, F. Wudl, and A. J. Heeger. Polymer Photovoltaic Cells: Enhanced Efficiencies via a Network of Internal Donor-Acceptor Heterojunctions. *Science*, 270(5243):1789–1791, 1995.

[245] X. Yang and A. Uddin. Effect of thermal annealing on P3HT:PCBM bulk-heterojunction organic solar cells: A critical review. *Renew. Sust. Energ. Rev.*, 30:324–336, 2014.

[246] I. A. Howard, R. Mauer, M. Meister, and F. Laquai. Effect of Morphology on Ultrafast Free Carrier Generation in Polythiophene:Fullerene Organic Solar Cells. *J. Am. Chem. Soc.*, 132:14866–14876, 2010.

[247] R. Mauer, M. Kastler, and F. Laquai. The Impact of Polymer Regioregularity on Charge Transport and Efficiency of P3HT:PCBM Photovoltaic Devices. *Adv. Funct. Mater.*, 20:2082–2092, 2010.

[248] Y. Kim, S. Cook, S. M. Tuladhar, S. A. Choulis, J. Nelson, J. R. Durrant D. D. C. Bradley, M. Giles, I. McCulloch, C.-S. Ha, and M. Ree. A strong regioregularity effect in self-organizing conjugated polymer films and high-efficiency polythiophene:fullerene solar cells. *Nature Mater.*, 5:197–203, 2006.

[249] R. D. McCullough, S. Tristram-Nagle, S. P. Williams, R. D. Lowe, and M. Jayaraman. Self-orienting Head-to-Tail Poly(3-alkylthiophenes): New Insights on Structure–Property Relationships in Conducting Polymers. *J. Am. Chem. Soc.*, 115:4910–4911, 1993.

[250] J. Cornil, D. Beljonne, J.-P. Calbert, and J.-L. Brédas. Interchain Interactions in Organic π-Conjugated Materials: Impact on Electronic Structure, Optical Response, and Charge Transport. *Adv. Mater.*, 13(14):1053–1067, 2001.

[251] J. Clark, C. Silva, R. H. Friend, and F. C. Spano. Role of Intermolecular Coupling in the Photophysics of Disordered Organic Semiconductors: Aggregate Emission in Regioregular Polythiophene. *Phys. Rev. Lett.*, 98(206406), 2007.

[252] M. A. Green, K. Emery, Y. Hishikawa, W. Warta, and E. D. Dunlop. Solar cell efficiency tables (version 39). *Prog. Photovolt: Res. Appl.*, 20:12–20, 2012.

[253] L. Onsager. Initial Recombination of Ions. *Phys. Rev.*, 54:554–557, 1938.

[254] X. M. Jiang, R. Österbacka, C. P. An, and Z. V. Vardeny. Photoexcitations in Regio-regular and Regio-random Polythiophene Films. *Synt. Met.*, 137:1465–1468, 2003.

[255] A. Dogariu, D. Vacar, and A. J. Heeger. Picosecond time-resolved spectroscopy of the excited state in a soluble derivative of poly(phenylene

vinylene): Origin of the bimolecular decay. *Phys. Rev. B*, 58(16):10218–10224, 1998.

[256] P. J. Brown, D. S. Thomas, A. Köhler, J. S. Wilson, J.-S. Kim, C. M. Ramsdale, H. Sirringhaus, and R. H. Friend. Effect of interchain interactions on the absorption and emission of poly(3-hexylthiophene). *Phys. Rev. B*, 67(064203), 2003.

[257] X. Jiang, R. Österbacka, O. Korovyanko, C. P. An, B. Horovitz, and R. A. J. Janssen. Spectroscopic Studies of Photoexcitations in Regioregular and Regiorandom Polythiophene Films. *Adv. Funct. Mater.*, 12(9):587–597, 2002.

[258] F. C. Spano. Modeling disorder in polymer aggregates: The optical spectroscopy of regioregular poly(3-hexylthiophene) thin films. *J. Chem. Phys.*, 122(234701), 2005.

[259] T. F. Heinz, H.-E. Ponath, and G. I. Stegeman. *Nonlinear Surface Electromagnetic Phenomena - Second-Order Nonlinear Optical Effects at Surfaces and Interfaces*. Elsevier, Amsterdam, 1991.

[260] A. Nahata and T. F. Heinz. Detection of freely propagating terahertz radiation by use of optical second-harmonic generation. *Opt. Lett*, 23(1):67–69, 1998.

[261] G. Grancini, N. Martino, M. R. Antognazza, M. Celebrano, H.-J. Egelhaaf, and G. Lanzani. Influence of Blend Composition on Ultrafast Charge Generation and Recombination Dynamics in Low Band Gap Polymer-Based Organic Photovoltaics. *J. Phys. Chem. C*, 116:9838–9844, 2012.

[262] S. R. Cowan, N. Banerji, W. L. Leong, and A. J. Heeger. Charge Formation, Recombination, and Sweep-Out Dynamics in Organic Solar Cells. *Adv. Mater.*, 22:1116–1128, 2012.

[263] I. Hamberg, C. G. Granqvist, K.-F. Berggren, B. E. Sernelius, and L. Engström. Band-gap widening in heavily Sn-doped In_2O_3. *Phys. Rev. B*, 30(6):3240–3249, 1984.

[264] A. W. Hains, Z. Liang, M. A. Woodhouse, and B. A. Gregg. Molecular Semiconductors in Organic Photovoltaic Cells. *Chem. Rev.*, 110:6689–6735, 2010.

[265] G. Heywang and F. Jonas. Poly(alkylenedioxythiophene)s– New, Very Stable Conducting Polymers. *Adv. Mater.*, 4(2):116–118, 1992.

[266] P. Peumans, S. Uchida, and S. R. Forrest. Efficient bulk heterojunction photovoltaic cells using small-molecular-weight organic thin films. *Nature*, 425:158–162, 2003.

List of Publications

Publications Related to this Thesis

Reversible Photoswitching of the Interfacial Nonlinear Optical Response
Michael Schulze, Manuel Utecht, Andreas Hebert, Karola Rück-Braun, Peter Saalfrank and Petra Tegeder
J. Phys. Chem. Lett., 6:505–509, 2015

Hot Excitons Increase the Donor/Acceptor Charge Transfer Yield
Michael Schulze, Marc Hänsel and Petra Tegeder
J. Phys. Chem. C, 118:28527–28534 2014

Reversible photoswitching of the interfacial non-linear optical response of an azobenzene-functionalized self-assembled monolayer
Michael Schulze, Thomas Moldt, Daniel Przyrembel, Manuel Utecht, Peter Saalfrank, Martin Weinelt and Petra Tegeder
in preparation

Publications not Related to this Thesis

Adsorption energetics of azobenzenes on noble metal surfaces
Michael Schulze, Christopher Bronner and Petra Tegeder
J. Phys.: Condens. Matter, 26(355004), 2014.

The influence of the electronic structure of adsorbate–substrate complexes on photoisomerization ability
Christopher Bronner, Michael Schulze, Sebastian Hagen and Petra Tegeder
New J. Phys., 14(043023), 2012.

Academic Curriculum Vitae

Der Lebenslauf ist in der Online-Version aus Gründen des Datenschutzes nicht enthalten.

Acknowledgments

First of all I would like to thank Petra Tegeder for supervising this PhD thesis, for countless constructive discussions, for the chance to present our results on numerous conferences and meetings and especially for giving me the great opportunity to work at the Columbia University in New York City. I would also like to thank my second supervisor Martin Weinelt for advice and active support on many occasions.

I am especially grateful for experience and know-how on applied non-linear optics which has been shared with me by Alexey Melnikov and Alexandr Alekhin of the Fritz-Haber-Institut in Berlin which greatly helped setting up the experiment and by Xiaoyang Zhu, Cory Nelson and Xiaoxi Wu during my time in New York City which enabled the experiments on the exciton and charge transfer dynamics.

For introducing the laser setup to me, for sharing his experiences on various topics and especially for taking the time to review the manuscript to this thesis, I would like to thank Christopher Bronner. For the many working hours we spend together, I would like to thank my colleagues in Berlin and Heidelberg Alexander Broska, David Gerbert, Marc Hänsel, Felix Leyssner, Friedrich Maaß, Michael Meyer, Laurenz Rettig, Stephan Stremlau and Erwan Varene and I am particularly grateful to Philip Rackow for the things I have learned during supervising his master thesis. I would also like to thank Dietgard Mallwitz and Irmhild Wegener for their help in overcoming any administrative hurdles.

I am especially thankful for the constructive collaborations and the according opportunities to work on a variety of interesting projects. In particular, I would like to thank Thomas Moldt, Daniel Przyrembel and Martin Weinelt (Freie Universität Berlin) for the cooperative work on the azobenzene self-assembled monolayers and Andreas Hebert and Karola Rück-Braun (Technische Universität Berlin) for the mutual accomplishment of the project concerning the fugimide-functionalized photochromic interface. I also acknowledge Manuel Utecht and Peter Saalfrank (Universität Potsdam) for investigating both projects from a theoretical point of view. Regarding the charge transfer dynamics project, I would like to thank Marcel Schubert, Steffen Roland and Dieter Neher (Universität Potsdam) for sample preparation and for constructive discussions in his group seminar, at the ICEL-10 and beyond, respectively.

I gratefully acknowledge the funding of the presented work by the Freie Uni-

versität Berlin, the Ruprecht-Karls-Universität Heidelberg and the Deutsche Forschungsgemeinschaft through the collaborative research center SFB 658 and the priority program SPP 1355.

Finally, I would like to thank Thomas Kunze and Kristof Zielke for sharing their office and Meike Herkewitz for proofreading the manuscript to this thesis.

Eidesstattliche Erklärung

Hiermit versichere ich, dass ich alle verwendeten Hilfen und Hilfsmittel angegeben habe und die vorliegende Arbeit auf dieser Grundlage selbständig von mir verfasst wurde. Diese Arbeit wurde nicht bereits in einem früheren Promotionsverfahren eingereicht.

Berlin, 9. Oktober 2014
Michael Schulze